amt-2019-27 – Spanu et al.

Author's Responses to Referee Comments and Short Comment

We thank the two referees and Peter Spichtinger for their useful comments. These comments were all considered and also helped us to identify aspects in the manuscript that needed some additional revision.

We are in the process of getting a data DOI (see data availablility section) but we don‘t have it already. We will add it as soon as possible.

This document contains our responses to Referee #1 *(page 2-11, ignore page number written on page)*, Referee #2 *(page 12-21)*, and Peter Spichtinger *(page 22-24)* as available in the interactive discussion. These responses are followed by a list with the most significant changes in the manuscript *(page 25)* and a marked-up manuscript version (created using latexdiff) showing all changes in the text made during the revision *(page 26-77)*.

We wish to thank the reviewer for carefully reading our manuscript and for providing suggestions which helped us to improve the manuscript. In the following, the questions and comments raised by the reviewer are marked in blue and our answers are written in black.

This manuscript is a useful addition to the growing body of work investigating the influence of airborne particle instruments on the measurements that they are making. The most important aspect for me is the influence of Stokes number on particle velocity through the probe sample volume, this is nice. That said, I think that there are a couple of general and more specific issues that I would prefer to see addressed before publication.

The flow model includes the airframe, or possibly a section of wing and the canister plus pylon, and a hemispherical dome approximation of the probe. Some more details about how much of the aircraft is included in the model would be useful and if the flows at each of the four hard points are the same or different. No specifics are given for modelling the DC-8, it is unclear whether the flows at the probe location on the DC-8 shall be similar or the same as those on the Falcon. This is important as one of the conclusions relates to minimizing the difference between TAS and PAS by judicious positioning of the probe on an aircraft.

Related to this question, we give more detail below. Generally, the flow under the wing is slightly varying along the wing since the wing cross section varies between the aircraft fuselage and the wing tip. Because of this, small differences between the hard points are possible. We haven't modelled the DC-8 since our results show that the concentration depends only on the ratio between the local air flow and the free stream air flow.

The angle of attack (AOA) of the Falcon is briefly mentioned in section 2.1.2. It appears that the AOA is held constant for all flight conditions used in the simulations such that the orientation of the probe is always aligned with the local flow, or at least in so far as the error associated with the misalignment is negligible. Given that the simulations are done over a very large range of pressure and TAS and that an aircraft's AOA maybe expected to change by degrees over this range, it would be useful to see some justification for this statement.

We have performed numerical sensitivity studies related to the dependency of the results on AOA. Figure 1 (in the reply) shows the deviation between PAS and TAS as a function of ambient pressure color-coded with the angle of attack (AOA) for the arbitrarily chosen TAS range from 152.5 m/s to 157.5 m/s from measurements during the SALTRACE campaign. A TAS range had to be chosen for this figure because the deviation between PAS and TAS depends also on TAS. However, the picture is similar for other TAS ranges and shows that the AOA has only a minor impact on the measurements ((PAS-TAS)/TAS changes less than 2% when the AOA is changed). Therefore, we chose a median AOA value (4°) for our analysis.

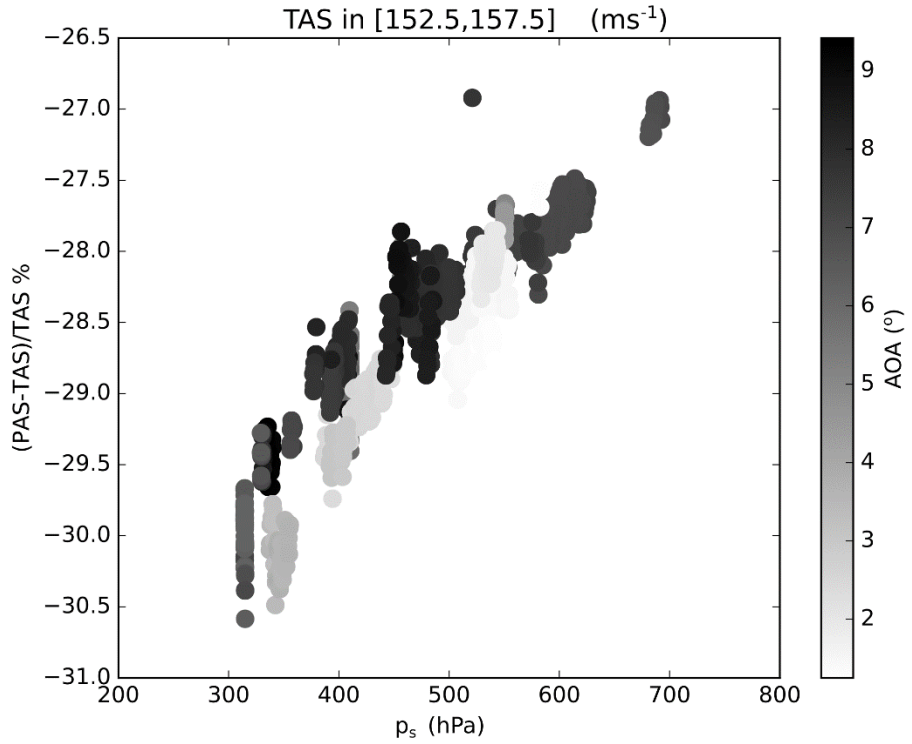

Figure 1. Deviation between PAS and TAS as a function of ambient pressure color-coded with the angle of attack (AOA). Markers represent measurements at 1Hz collected during the SALTRACE campaign.

No mention is made about these matters with regards to the DC-8 either.

On the DC-8, CAPS is mounted near the wing tip, i.e. it is less affected by the AOA, since the wing chord and the wing thickness is smaller at this part of the wing.

This work appears to approximate the probes with a semi-hemispherical dome. It would be a significant addition (and an unreasonable request) to include the actual probe geometries. However, a comment comparing this work to that of Weigel et al. (2016) and Korolev, Emery, and Creelman (2013), both already cited and which use accurate probe models, would be very interesting given the influence of the probe design on the local flow distortions and the apparent similarities in PAS/TAS ratios seen.

Figure 6b and 6c in the manuscript show the measured and simulated differences between p and PAS at the probe location and the corresponding values at free stream condition. The simulated values are well within the measured range. Therefore, we think that the simplified instrument geometry is a valid assumption.

Specific Comments

More specific comments are included here. I have included the page.line number/s to assist although some of these comments may apply to multiple places in the text.

3.31 The manuscript uses 'airspeed' extensively throughout. It would be useful in the context of airborne measurements to clarify that true air speed is used as opposed to any of the other definitions used with regards to aircraft. TAS and PAS are defined later at 5.20. 'Speed' is mentioned in section 2.1 but this clarification may be introduced earlier if more convenient/coherent. See comment 7.22 below for more.

We changed this in the manuscript as suggested.

4.3 Air speed uncertainties are more relevant here than those in static pressure, can these be related to air speed errors for the range of conditions relevant to this work?

Yes, if we assume the errors are only affecting the static pressure. In this case, a 1% overestimation of the static pressure will result in a 0.5% overestimation of the air speed according to the Bernoulli equation.

4.5 Are the uncertainties of the DC-8 MMS known? Are they comparable with those of the CMET?

Yes, the two uncertainties are similar and represent errors smaller than 2% on the total pressure. Figure 2 shows the deviation of the total pressure between CAS and the Falcon CMET system during SALTRACE and between CAS and the DC-8 MMS system during ATom-1.

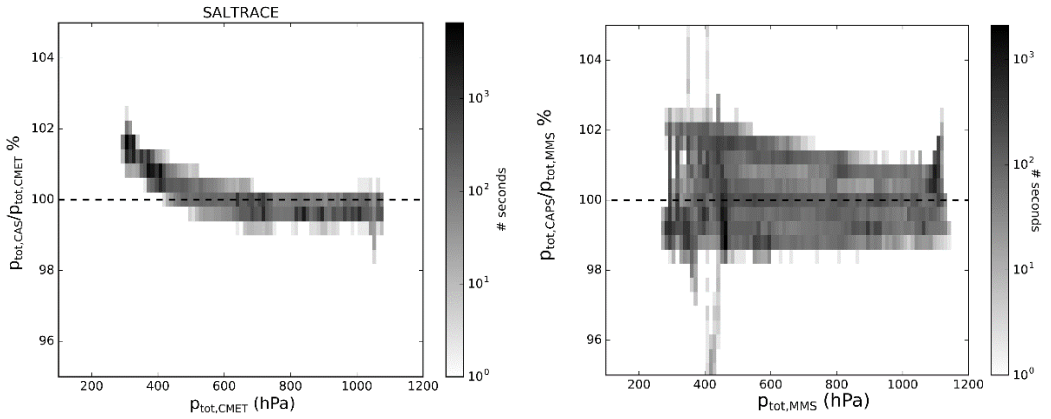

Figure 2. Deviations of total pressure measured by CAS and by the Falcon CMET system during SALTRACE (left), and the DC-8 MMS system during ATom-1 (right), respectively.

4.30 In my opinion it is inaccurate to say that most probes have pitot tubes close to the sample volume. The DMT PIP- or CIP-based instruments do, the AIMMS does (although is less relevant as it does not measure all that close to particle instrument sample volumes), but (most/all?) other instruments do not. So actually, the reverse of what is stated is the case. I'd suggest adding the importance of local PAS measurements to the conclusion of the manuscript with discussion about when it is most/least necessary based on what is being measured.

We changed the text in the paper as suggested. It reads now:

"As we described, OPC and OAP measurements depend on the flow, therefore wing-mounted instruments are sometimes equipped with flow sensors to constrain local conditions."

In addition, we added text to the conclusion of the manuscript explaining the importance of local PAS measurements.

5.26 Positional errors are discussed throughout the manuscript and I found the usage confusing. Positional error, when defined in section 2.1.2, relates (as I read it) to the difference between TAS and PAS where TAS is the free stream air speed and PAS is the airspeed in the sample volume in the probe. However, in 9.9 it seems that positional error possibly also refers to the difference between the airspeed measured at the pitot on the probe and that at the sample volume of the probe (due to the difference in PAS measured by the long and short pitot tubes). However, there is no specific mention/quantification of the difference in air speed between the pitot and sample volume. Please clarify the usage if possible.

With the term "position error", we refer to the difference between TAS and PAS. For this reason, a longer pitot tube will reduce the position error because the difference of the pressure at the probe and at free stream is exponentially decreasing as a function of the distance from the probe head. We assume the pitot tube measurements to be representative for the sampling area (see Fig. 5 and text of the revised manuscript). Thus, using a longer pitot tube, implies the sampling area also to be at a larger distance from the main instrument body. This is the case for CAPS.

6.16 Does "simplified three-dimensional model" mean a hemispherical dome as shown in Fig 4? If so this is quite the simplification for a CAPS for example. So mention of expected uncertainties due to this simplification would be useful.

As mentioned previously, Figure 6 in the manuscript shows the measured and simulated differences in pressure and air speed at the probe in comparison with free stream conditions. The simulated values are well within the measured range. Therefore, we think that the simplified instrument geometry is a valid assumption.

7.22 The use of 'airspeed' throughout is not as clear as it should be. In this sentence it is used to describe the velocity of a particle relative to the volume of air that contains it (slip velocity). Previously it has been used to describe the velocity of the aircraft and/or probe relative to the air. The difference is very important in this work so I suggest defining unique terms for consistent use throughout. TAS and PAS are traditionally used for the latter case so I'd suggest the use of slip velocity or some other term for the former.

We modified the text and the figures, according to your comment and now use "slip velocity".

8.23 Mention should be made to confirm if aircraft angle of attack changes with TAS in this model (here and elsewhere).

The simulations presented in the manuscript were made for a fixed AOA (4°). This AOA was selected to represent the median conditions as visible in Figure 3. Also, it can be seen from Figure 1 that changes of the AOA have only a minor impact on the relative deviation of PAS from TAS.

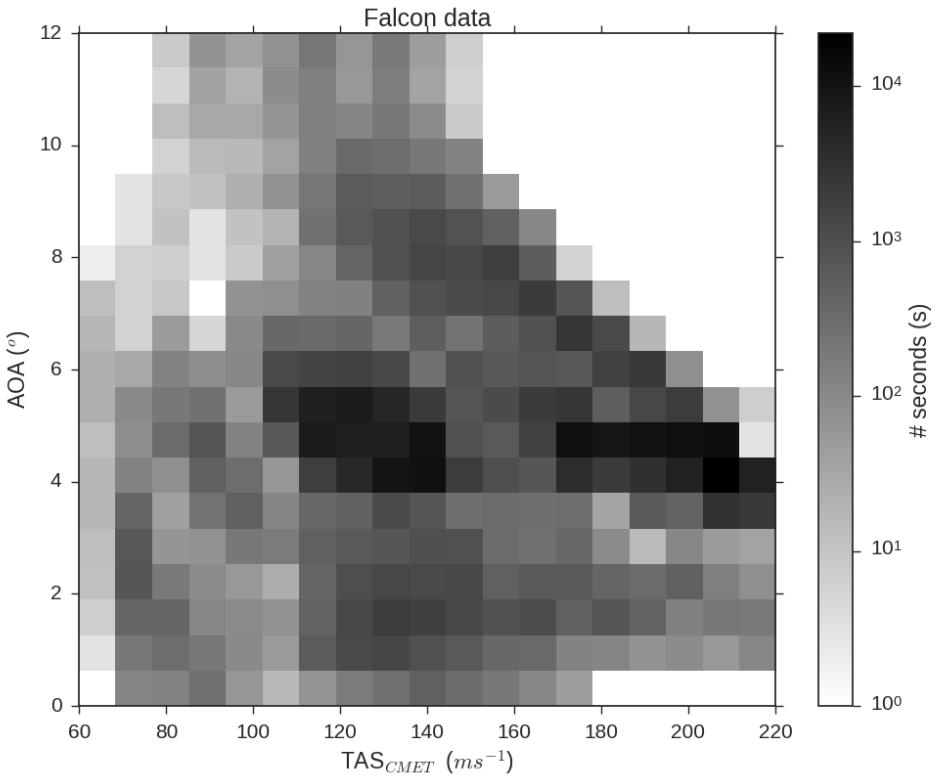

Figure 3. Frequency of AOA vs. true air speed (TAS) during the SALTRACE campaign in 2013.

13.11 There is something missing in the description of the Vargas experimental set up which made interpretation difficult. It turned out that this is the fact that the droplet is 'dropped' perpendicular to the plane of the rotating airfoil and therefore has a velocity in that plane of zero when far from the airfoil. An extra sentence to more fully describe the experiment that you are simulating would be useful. Also suggest using slip velocity instead of Urel as this is a commonly known term.

We extended the description of the Vargas experiment to clarify it. We also substituted Urel with Uslip in the entire manuscript.

How is 'breakup' that occurs around 60 ms−1 defined/identified given that the images in figure 14 contain only a single particle?

According to Vargas (2012), droplet breakup is occurring at the edge of the droplet by a stripping mechanism. In the volume of fluid (VOF) simulations the breakup is identified by considering the number of regions in the simulation which contain a liquid phase. If more than one such region is identified, the droplet is counted as "broken".

14.10 It is not obvious to me why the varying slip velocity case is different from the invariant one. An explanation would be appreciated.

According to Vargas (2012), the droplet in case of a varying slip velocity has more time to adjust to the flow. We extended the description and added a reference to Vargas (2012).

17.4 VOF has not been defined previously.

Corrected.

17.5 Has there been discussion about “wiggling” behavior previously? More specific language is required here.

According to the comment, we removed the term “wiggling” and reformulated the sentence.

17.6 Have Taylor instabilities been discussed previously?

Yes, they were mentioned on 14.22. We reformulated the sentence and removed this term from the conclusions.

3 Technical Corrections

There are quite a few basic notation inconsistencies, spelling mistakes, and technical errors that make following the text difficult and detract from the quality of the manuscript. Below are listed the technical corrections that I have caught, given as page. line numbers.

3.32 “per default” is quite an odd expression. “By default” would be more typical although in this instance I think the sentence makes sense without either, ie “The DLR Falcon is equipped with a...”

Done.

4.3 Does “pilot-induced manoeuvres” mean turns but not fluctuations due to auto-pilot corrections or turbulence? Clarification of this phrase would be helpful.

Yes, according to the cited article it refers only to pilot-induced maneuvers. Auto-pilot corrections or ‘normal’ turbulence probably result in even smaller errors.

4.19 Is “composed instrument” supposed to read “compound instrument”?

We modified the text and now leave out “composed”.

4.21 A OAP does not measure diameter directly, the user/software determines the size from the image recorded by the array. Different size metrics are defined in section 3.2.2 and so could be referred to here.

We modified the sentence including a reference to 3.2.2.

4.23 I’m not sure what is meant by “named shutter-speed of the camera”.

We modified the sentence and now leave out “named shutter-speed of the camera”.

4.24 The SID is a scattering instrument not an OAP so should be removed from this list.

SID has been removed from the list of OAP.

5.19 It seems as if “attack angle” here is used in reference to the alignment of the probe to the local air flow. This is confusing as “angle of attack” is traditionally used in reference to the alignment of the aircraft to the air flow (and indeed appears to be used in this way in 5.16). This should be clarified.

Your comment is correct. To avoid misunderstanding, we modified the sentence.

5.21 I’d prefer that “measured” is removed as the PAS is the airspeed at the probe location whether it is measured or not.

Done.

6.16 Change PMS and add canister to sentence to read “...Particle Measurement Systems canister...”

Canister in mentioned later in the same sentence so that we think it is not necessary to add it here.

6.21 Do you have a reference for snappyhexmesh?

We added a reference to snappyhexmesh:

Montorfano, A (2017) Mesh generation for HPC problems: the potential of SnappyHexMesh, doi:10.13140/RG.2.2.25007.53923

6.24 There is some confusing notation regarding *U*, ***U***, and U. The usage should be consistent, particularly between the italic and upright versions. One can reasonably assume that U0 is defined along the free stream direction given|U0|=TAS but an explicit definition of the axes along with consistent nomenclature would make this is clearer.

Done. For clarity, we included a new table in the revised manuscript giving an overview of the different velocities and speeds.

7.13 Change “as” to “an”.

“As” was correct, but “an” was missing. Now it reads: “Droplet breakup, as an effect of the instability … ”

7.16 Change “model including...” to “model to include...”.

Done.

7.17 Change “not fully agrees...” to “does not fully agree...”.

Done.

7.27 I'm not sure what is meant by "...both in the spatial and temporal discretization". Should "in" be replaced by "with"?

We think that "in" is correct, but modified the sentence slightly to make it more clear. It now reads as: "… both in the spatial and in the temporal discretization …"

8.26 This sentence uses upright U, should they be italic?

Corrected.

9.3 The sentence starting "The simulation results refer to..." is unclear. Is this "The figure refers to..." or "The simulation results are relative to..." or something else?

Improved. The sentence reads now "The simulation results in Fig. 6 are valid …"

9.9 See discussion on positional errors in the previous section but in this sentence it would be useful to know why and how the longer pitot tube effects to positional error. This shall assist in understanding the uncertainties when applying the methods discussed to instruments with different pitot tubes or even using pitot tubes mounted near a probe but not as part of the instrument.

See also our reply to comment 5.26 (p. 4). The text in the manuscript has be revised.

9.17 Typo in "However".

Although there is the term "howsoever", we now use "nevertheless".

10.9 The test case u100_p900 is not actually included in Figure 8.

The case u100_p900 has been added to Fig. 8.

11.16 Specify which air speed you are referring to here.

As recommended, we use "probe air speed" to make the message more clear.

12.18 It may be pedantic but Figure 12 shows circular images (which admittedly one assumes are of spherical drops).

We changed the text as follows: "Most of the droplet images are circular…"

12.23 The x and y dimensions should be defined in terms the array and with time (in terms of which the image is described in 12.16) so that the reader understands the aspect ratio values. This is clarified in 13.1 but should be brought forward to this point.

We modified the manuscript as suggested.

12.24 The markers in Figure 13 are not black.

We modified the Figure 13 which now uses three different colors.

14.3 The symbol for Weber number should be italics so that it is more obvious in text.

We modified the Weber symbol in the entire text.

15.1 Add what threshold value you have used in your greyscale images when finding image area.

We have used a threshold value of 0.8. The value is now specified in Sect. 3.2.

18.22 This is cited (incorrectly) in the body as Osborne and Cotton. The full author list is required here.

The SID reference has been removed according to your comment and consequently the reference too.

45.6 The data DOI needs updating.

We are in the process of updating the data DOI. Since we included new data, the update takes more time.

Comments on figures:

Fig 2 Many of the figures are shaded by number of seconds, for clarity it would be useful to add "...number of seconds of data at 1 Hz".

We added the "...number of seconds of data at 1 Hz" in the figure captions where necessary.

Fig 4 The free stream flow should be marked on this plot. There is some confusion regarding the orientation of the flows in the model between figures 4, 5, and 7. In figure 4, if the free stream is oriented with the figure then it appears as if the angle of attack (AOA) of the aircraft is not accounted for and the probe is not aligned with the flow. In figure 5, the free stream is aligned with the probe and so the AOA has been accounted for, however for the given flight conditions I assume that the AOA is changing, and this is not mentioned (see previous comments regarding AOA). In figure 7, the free stream seems to be coming up to the probe from below (which is opposite to the case shown in figure 4) or perhaps aligned with the probe, it is difficult to tell.

To make the message more clear, we changed the color-scale and added an arrow indicating the direction of the free stream flow. We also modified the scale label now using "(U-U0)/U0" to be consistent with Figure 5.

Fig 5 The pitot tube seems to be located diagonally off centre from the dome. Does the schematic represent where the pressure/velocity was measured or was it measured in front of the stagnation point of the dome (I assume that this is where the sample volume is)?

Correct, the pitot tube is located diagonally off center in the instrument and in the simulations. The schematic represents where the pressure/velocity was measured/simulated. The simulation results refer to the pitot tube static port location.

Fig 7 It would be useful to use the same colour scale parameters in this figure as in figure 4. When I converted from ratio to difference the values appear inconsistent between these two figures, is this an issue with my maths/understanding of what is being presented or an actual inconsistency between the two plots?

We modified the Figure. Now it is showing the density of the air $((\rho-\rho_0)/\rho_0)$. We modified the text accordingly.

Fig 13 The main text and caption refer to black markers, maybe it's my display/print but there doesn't appear to be any black markers.

The A-LIFE and ATom-2 data have similar shades of grey, completely different colours would be significantly clearer.

We modified the figure using now three different colors.

Is there a reason that the red trace, the mean for the ATom-1 data does not approach unity for small particles?

Yes, the bias is introduced by the wrong droplet speed (PAS instead of TAS) for the image reconstruction.

Fig 16 There appears to be multiple data points for the same TAS values (most evident for 125 ms−1), is this a plotting error or does it illustrate the different test cases? If the latter, it should be mentioned that P and T don't make a lot of difference.

For some velocities (TAS) there are more than one test case (see Table 2 in the manuscript for details). We added a clarifying comment in the manuscript.

We wish to thank the reviewer for carefully reading our manuscript and for providing suggestions which helped us to improve the manuscript. In the following, the questions and comments raised by the reviewer are marked in blue and our answers are written in black.

The paper takes simulations of the airflow around the wing and canister mount of the DLR Falcon aircraft (the canister mount being the location of the aircraft's cloud micro-physics instruments) and uses these to determine biases and corrections upon cloud microphysics measurements. It also examines how this airflow can induce droplet de-formation and breakup. A particular aspect of this work is its use of compressible flow in the simulations which allow application to airspeeds relevant to the faster speeds flown by the Falcon.

In general the work is entirely relevant to AMT and very worthwhile. Significant biases can exist in aircraft cloud microphysics measurements and this addresses one of those sources. In particular the work regarding biases in concentration due to airflow are incredibly useful for the community. There are two overarching limitations though, that I feel the authors should address, that I will mention here in the general comments. I will add more detail in the specific comments section.

The first of these limitations is that the simulations do not include the aircraft fuselage. There are three basic elements that could distort the flow along a particle trajectory before measurement. These are the instrument itself (represented in this work by a general instrument canister), the aircraft wing and the aircraft fuselage. The authors have chosen to include two of these three items in the simulations. They need to justify why the instrument and the wing are important, but the fuselage is not. I am not claiming that the fuselage is important, as I cannot say for certain that it is or it is not, but the authors must justify its exclusion. The second of the limitations is the discussion around image deformation and drop deformation and breakup. Figure 16, showing the breakup diameter for various airspeeds is a very useful plot as it shows the limits of our measurements. However, the discussion of droplet deformation seems to be less rigorous than the work regarding flow induced biases and given the other mechanisms which may induce IMAGE distortion, it is difficult to be certain that the distorted images are definitely, the result of distorted droplets in the manner described here. Some of the theory, observations and discussions do not seem consistent. I would suggest one of two options. Either this section needs rewriting, being much more careful about consistency and ensuring it is very clear what is discussion and what is conclusion, or alternatively this section could be significantly reduced in size or removed – the section discussing efficiencies is interesting enough to stand alone. As a final general recommendation, although the English in the paper is mostly very good (and much better than my foreign language skill would permit me to write in my non-native tongue), there are times when it is obvious that the paper is written by a non-native English speaker and the wording is difficult to under-stand. I would therefore recommend that the authors have the final version proof read by a native English speaker. Overall, the paper covers important aspects of the cloud microphysics measurement system and I absolutely recommend publication with the changes outlined in this review.

Specific Comments

P2L14 Explain why the temperature and pressure further affect the aerosol and cloud measurements – what mechanism are you referring to.

The flow around the aircraft modifies pressure and temperature of the air and as a consequence of the gas law also the air density at the instrument's sampling area. Consequently also the particle concentration, in particular of small particles, is affected. Furthermore, the flow distortion also modifies the sampled flow velocity. For example, higher pressure is related to a lower flow velocity (Bernoulli equation, energy conservation).

We have updated the manuscript.

P2L18. Are droplets appearing deformed because they are deformed due to aerodynamic forces or are they appearing deformed because of a bias with the instrument system (off axis flow, incorrectly measured particle speed).

They can appear deformed because of both mechanisms:

1.) Droplets may appear as deformed on the images, but they are not deformed on reality. This is the case if the camera does not use the correct velocity for taking the images.

2.) Large droplets are deformed due to aerodynamic forces. Both citations refer indeed to shape distortion mechanism at the droplet surface.

We rephrased the paragraph to make it more clear.

P2L32 compressible flow is not a hypothesis

We reworded the text and skipped the word 'hypothesis'.

P3L2 and throughout aircraft is probably a better word than plane or airplane in technical writing.

Done. We now only use the word aircraft.

P4L24 SID-2 is an open path OPC, not an OAP. Note also that SID-3, despite taking images, is not and OAP either as it uses a 2D CCD, not a line of photodiodes.

We removed the SID from the list of instruments.

P5L15 Insert the word measured before "dynamic pressure"

Done.

P5L23 Is the overestimation of airspeed an overestimation of PAS or TAS. Be specific.

This statement is generally valid, i.e. to any velocity derived from pitot tube measurements using the Bernoulli equation under the assumption of an incompressible fluid. For example, using the Bernoulli formula for incompressible gas together with the nose boom pressure values will lead to an overestimation of TAS. In contrast, the same formula applied to the pitot tube of the wing-probe instrument will lead to an overestimation of the PAS.

We adapted the text.

P6L4 Have you checked the conservation of total pressure at the two pitot tubes? This would give a good check that their calibrations are not introducing bias.

Figure 1 below shows comparisons of the total pressure measured by the pitot tube of the CAPS with measurements of the CMET pitot tube on the DLR Falcon and the MMS pitot tube on the NASA DC-8, respectively. The deviation between the different pressure sensors is less than 2%.

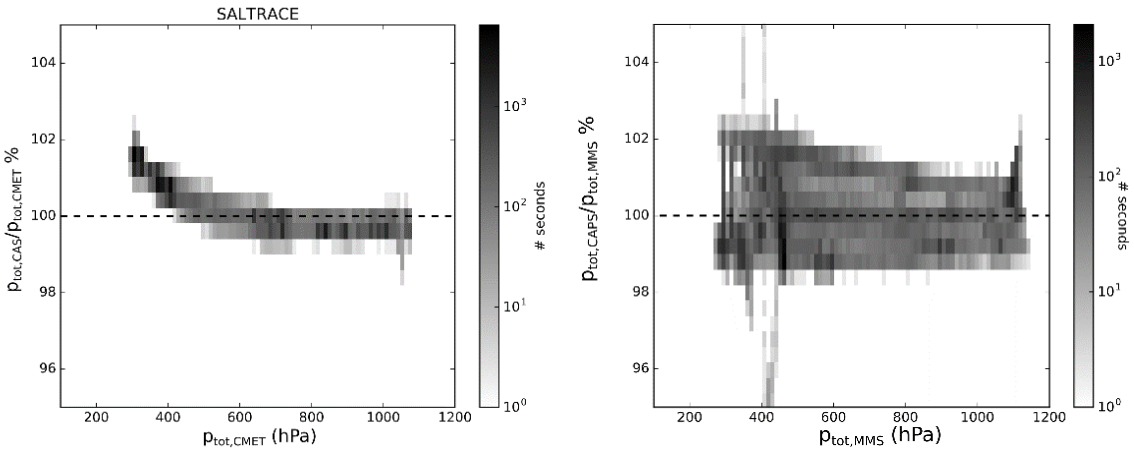

Figure 1. *Comparison between different total pressure measurements as a function of ambient pressure. Left: Ratio between CAPS pressure measurement and the DLR Falcon CMET pressure measurement. Right: Ratio between the CAPS pressure measurement and the NASA DC-8 MMS pressure measurement.*

P6L19 The authors have felt it necessary to make the edge length 10 times the canister length to avoid biases from the boundary. Although I appreciate that this was no-doubt chosen because it was a round number, that was at least as large (but probably larger) than necessary, I would guess that within this domain one may find either the aircraft fuselage itself or air which had been modified by flow around the fuselage. It may well be that this is not the case, or that the flow distortion caused by the fuselage does not impact the particle paths, but the authors should show that this is the case or they should provide some limits on the potential effects of the fuselage.

It was computationally too expensive and therefore not feasible to include the entire aircraft fuselage in the simulations. However, the pylon where the probe is mounted is about 1.5 m away from the fuselage therefore the wing and the pylon/canister/instrument are the main contributors to flow distortions at the measurement location. Furthermore, the measured and simulated differences in pressure and air speed at the probe in comparison to free stream conditions show that the simulated values are well within the measured range (see also Figure 6 in the manuscript). Therefore, we think the exclusion of the fuselage does not introduce a significant bias.

They should also describe the effect of the wing itself, so that it is clear to the reader that both the wing and the instrument canister have an impact upon the flow. This will certainly feed in to decisions made by future studies into flow effects on microphysics measurements.

We performed new numerical simulations only considering the effect of the wing. The result is shown in Figure 2. The wing will contribute only up to 9% whereas the total effect is up to 24%.

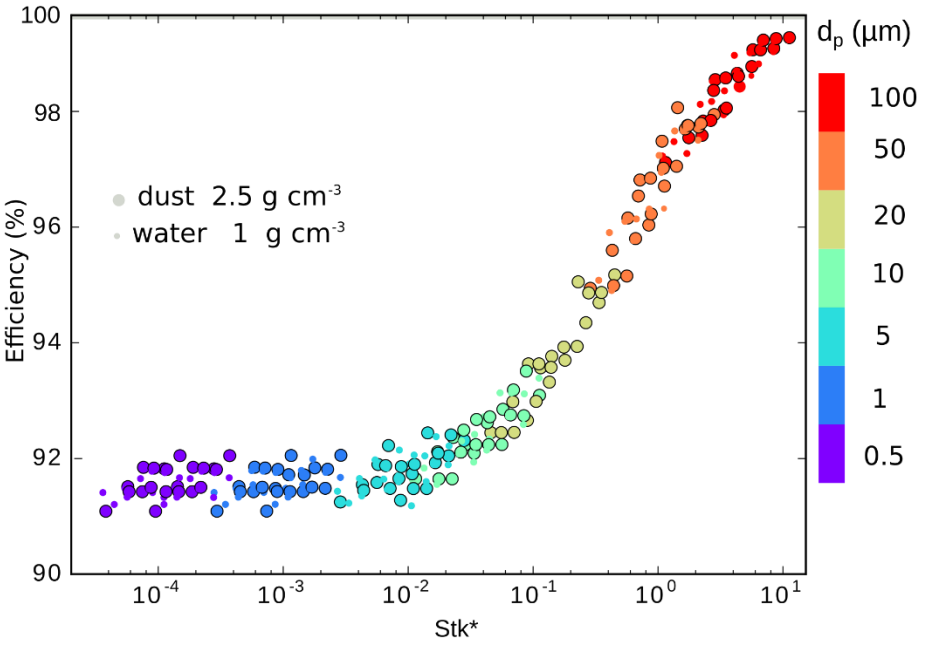

Figure 2. *Same as Figure 8 in the manuscript, but only simulating the effect of the wing. The sampling efficiency is calculated as a function of modified Stokes number (see Eq. 4) for the selected numerical test cases of Tab. 3 in the manuscript. Each marker represents a run where we released 2 x 10^5 particles of a specific diameter (colors) and density (small marker size: water; large marker size: dust) calculated at the upstream of the probe in the computed flow field. Sampling efficiency is defined as the ratio between particles released and particles passing through the sampling area, renormalized by the corresponding areas.*

P8L14 It would be nice to highlight the test case on all plots, either by circling the data point or putting the line in bold or some other method.

The test case (u100_p900) is always plotted with blue color.

P8L21 replace probe and free stream with local and free stream

Done.

P8L28 it would be good to see the incompressible solution on the charts for comparison.

The incompressible solution will look like the u75_p1000 simulation where the effect of is still small. We added a statement in the text.

P9L1 At first reading I thought the 1% error in ps was causing a 23% error in U. It maybe worth rewriting this sentence to ensure other readers don't make the same mistake.

Done.

P9L2 How much do we really care about temperature? Later in the paper the authors refer to the fact that there is a compression of air and a bias proportional to density which is in turn proportional to temperature. However, the temperature increase is a maximum of 3%. The authors also mention that the temperature is measured "round the back" of the probe so may not be that relevant to the

sample volume anyway. The authors should simply consider if the bias caused by temperature increase is worth considering, given the other uncertainties, and if it is they should explain at this point why it is of interest.

The temperature bias has only a minor effect. We kept mentioning the temperature bias in the text but also made clear that for our case it only has a minor effect.

P9L11 "Well represent" is an ambiguous term. The points from the simulations on figure 6c do not show the upside-down U shape that the measurements show. The authors should state some measure of the actual discrepancy and why they feel that this is sufficient.

For small TAS (below ~90 m/s), the configuration of the aircraft may be different (typically these speeds are observed during take-off and landing where the flaps are used). Also, the effect from the ground might be not negligible at low TAS. This is why we are not surprised by the small deviation between simulations and observations at these TAS values.

P9L14 What does "installed at the back" mean? Give some better description of the location of the temperature sensor and if it is not close to the sample volume then describe the expected error due to the position and whether this is sufficient – see above comment re temperature in general.

Figure 3 (see below) shows the position of the CAPS temperature sensor. The sensor is located at the same position in case of the CAS instrument.

Figure 6 (left panel) in the manuscript shows a statistical analysis of differences in the ratios between temperature values measured with the Falcon CMET system and with the CAS instrument during SALTRACE.

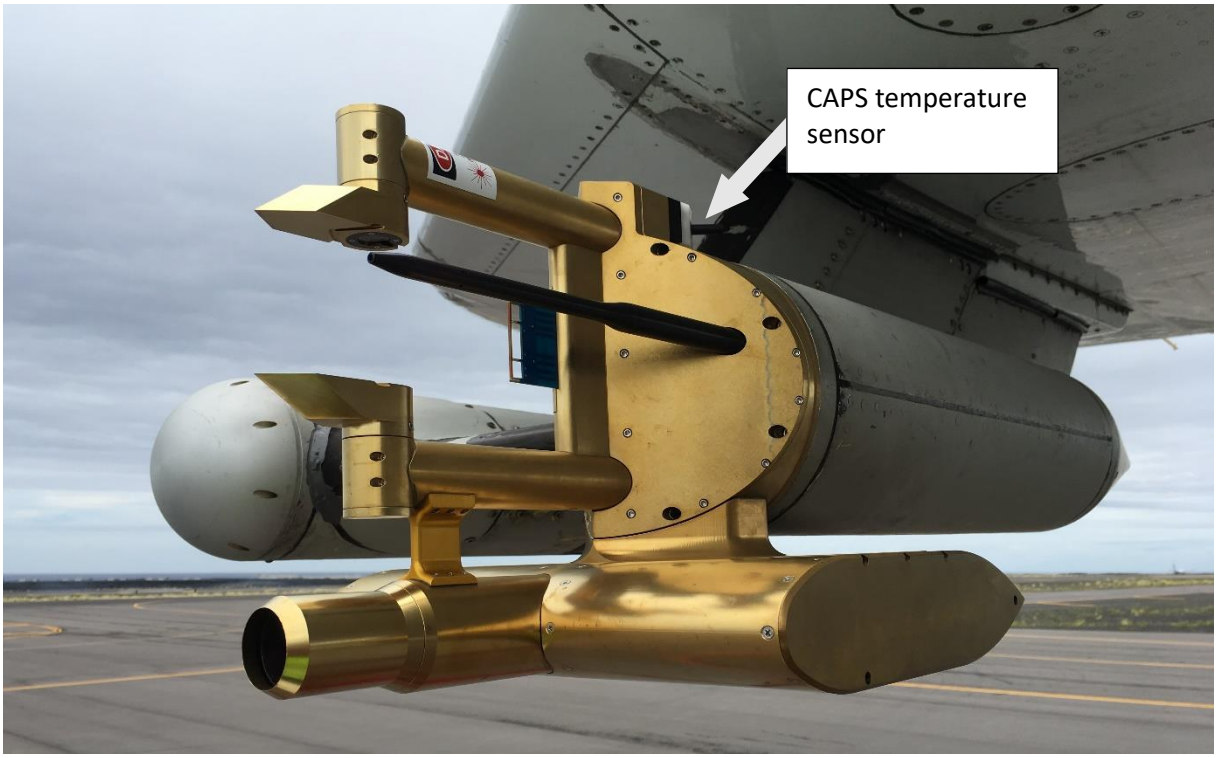

Figure 3. *Photograph of the CAPS mounted at the wing of the NASA research aircraft DC-8 during ATom-4. The position of the temperature sensor is marked by the white arrow. (Photograph: B. Weinzierl).*

P9L31 In what way is the stokes number modified and why?

According to Israel and Rosner (1982) the Stokes number is modified by introducing the correction factor psi which is a function of the Reynolds number distinguishing between the laminar and the fully turbulent case.

The text was modified accordingly.

P9l33 Equation (4) which velocity is used here for U? See later comments regarding stokes number.

To calculate equation 4 we use TAS. We added a new sentence to clarify the procedure.

P10 It is very impressive how well the data fit on the sigmoid curves on fig 8. This clearly forms an excellent correction factor. However, a few items may aid the reader in understanding the analysis that is occurring here.

Firstly, it would be good to indicate that the fit lines used are from equation (6).

The fit lines were obtained using a generic sigmoid function of the Stokes number using x0, k0 and k1 as free parameters. In the second step, we correlate these numbers (x0, k0, and k1) with flight conditions expressed as the alpha parameter.

We would also like to point out that there was typo in equation (6) where a plus was missing. We replaced it with the corrected equation.

Secondly, it should be noted that α is of the order 1 and contributes negligibly to the parameters x0 and k0, so should probably be removed.

The formulas given for x0, k0 and k1 were not correct. With the correct equations, the effect of alpha is stronger. Alpha is close to 1 in our case, but can have a larger effect in other cases. Therefore, we decided to keep the more general formula.

Thirdly, the authors should note that eˆ(-k0(log(stk)-x0) can be rearranged to b*stkˆa which is a much simpler form. Also if they remove the dependence of k0 and x0 upon α, then a and b simply become fitting constants. In fact b=10ˆ(x0*log(eˆk0)) and a=-log(eˆk0). Which makes b approximately -1.

We rearranged the formula.

Fourthly, it may be useful for the authors to rearrange the form slightly as this may help the points all converge onto 1 line.

We are not sure whether we understood this comment correctly. If the comment refers to Figure 8, we would like to clarify that the points in Figure 8 are not sitting on a line.

They should note the classic inlet efficiency equation from Belyaev & Levin doi:10.1016/0021-8502(74)90130-X, equation (5) Efficiency= 1+(u0/u-1) *sigmoid_function_of_stk_only Where u0 is

the far field velocity and u is the velocity at the inlet. This basically states that the deviation from unity efficiency is proportional to u0/u. This form may be useful to the authors, perhaps with u0/u replaced by α.

We considered the recommended explanation and the references in the text.

Fifthly, as described previously, the authors should consider whether it is really worth including temperature in this analysis as it is a relatively small effect and temperature may not be well measured by the probe.

See above.

P11L14 Do the authors actually mean mobility in the sense that it is used in aerosol science, e.g. for a scanning mobility particle sizer instrument? If not then change this word.

Yes, the term mobility is used in the same sense that it is typically used in aerosol science.

P11L26 The word positional error seems like an odd choice. Perhaps the authors mean distortion errors or something similar.

We improved the subsection title.

P11L27 did the authors mean 100 um? 10 um particles seem significantly affected by the flow.

We corrected the sentence now referring to particles with 30 µm diameter.

P11L31 rephrase. I think you want to say something like we adjust the calibration constants in the data logging software so that the pitot tube reports an air speed close to TAS rather than PAS. When this is reported to the instrument it causes the (insert info about lines imaged at the correct rate), but the PAS may still be recovered later by using the recorded pressures and the correct calibration constants.

We rephrased the sentence as recommended.

P12L14 The images shown in figure 12 are clearly distorted. However, it is not at all clear to me that this is a distortion of the droplets or just the images. In particular the images show a skew. This skew could be due to misalignment of the particle trajectory with the instrument axis, or perhaps it could be due to shear flow distorting the particles. This skew causes an apparent lengthening of the particles in the x direction – you will note that the farthest shadowed pixels on a droplet do not fall on the same line. It is not clear if any corrections for this have been made. Until a model can account for the skew distortion and the flattening, I think it is difficult to claim which mechanism is responsible. I think it is appropriate here to discuss how flattened the droplets are expected to be and to suggest it is a possible mechanism in the context of other possible mechanisms. But I don't feel it has been proven here that droplet flattening is the definite cause. Indeed the authors have the flow data to answer the question – are the particles travelling parallel to the probe axis?

The observation is correct. The particle trajectories especially for droplets with d>50µm can be considered parallel to the AOA. The difference between the AOA and the probe axis is in the

considered case small enough to be negligible. Indeed even considering a 1 degree angle between the AOA and the instrument axis this will result in a orthogonal component of TAS*sin(1°) which is less than 2% of TAS.

We would like to point out that only the larger droplets in Figure 12 are distorted, the smaller droplets (300nm and smaller) are not. This lead us to the conclusion that it is not the image what is distorted, but the distortion is caused by an aerodynamic force which preferentially acts on the larger droplets.

To make this point more clear, we included additional measurements from ATom-4 in Figure 12.

P13L5 It appears that airspeed errors of 10-20% would be perfectly sufficient to center the distribution of dy/dx over 1.0 for Atom-1. The a-life and Atom-2 data appear to show the opposite effect to that which would be expected from the droplet distortions described here. Please explain.

We included additional data from ATom-4 also in Figure 13.

We would like to point out that for ATom-1 the CAPS pitot tube was calibrated to measure the PAS, which for large particles leads to errors in the particle's/droplet's velocities of about 15% (depending on particle/droplet size). See Figure 11a in the manuscript for ATom-1. For A-LIFE, ATom-2 and ATom-4, we modified the calibration of the CAPS pitot tube to measure the TAS. The reason was to force the instrument to take the CIP images with the correct camera speed (large particle move with a velocity close to TAS).

If droplets start to deform by elongating in the y-dimension, they have a higher chance not to be fully recorded (see red contours in the new Figure 12 in the manuscript) and consequently they are removed from the analysis (Figure 13). This means that the deforming effect becomes less visible on larger particles.

P13L21 Be specific about what a small deviation is. Give the amount.

The results of our simulations are within two times the error bar of the experiments by Vargas (2012). We extended the text.

P14L23 There is no evidence for Taylor instabilities in Fig 13. Visually the scatter in the data looks to be entirely consistent with the error bars that the authors have put on the data. The authors would need to do some further analysis of the data scatter and if they find that the scatter is too large to be explained by the uncertainties, then and only then, should they invoke a mechanism to explain the extra scatter.

In the range between 200-500 µm, the dx/dy=1 line is outside the range of the error bar for most droplets. We think the data is sufficient to say that there is some scatter. We believe that the mentioned instabilities can be a possible reason for this scatter.

P14L28 Something here is not really matching up. The authors state that for a 200 um droplet they have We of 2.5 and it cannot be considered spherical, however close to that diameter on figure 13 the particles seem to generally have dy/dx within one error bar of unity. The author appears to be suggesting that observed broken up particles are caused by the mechanism here, or at least that some aircraft can go fast enough that droplets will be broken up so cannot be observed by the probes above a certain diameter.

Figure 12 shows deformed and broken particles/droplets (see red contours). According to Vargas (2012) this effect can be explained by aerodynamic forces.

But the points in Figure 15 show droplets going up to aspect ratios of 1.5 to 8. The only times I have seen such distorted particles has been when the refresh rate of the diode array has been clearly wrong. It may be that the authors have extrapolated the data for figure 15 past the break up point or perhaps there is something I am not able to piece together. But I can only suggest that section 3.2 needs a really thorough rewrite in order to ensure the arguments being made are consistent with the data and the model and to be clear what is a discussion and what is a conclusion.

We would like to point out that Figure 15 shows the results of simulations and not the analysis of droplets measured with the CIP instrument. In the grey-shaded area of Figure 15 there are also broken particles.

P14L29 I feel that the items discussed in section 3.2.2 are probably an over analysis of the data. Again the authors should be clear about what is a conclusion and what is a discussion and before they begin suggesting corrections for an effect they first need to be clear that they have shown the effect is real.

We would like to refer to Vargas (2012), who has shown the effect in a laboratory setting. Therefore, the shown effect is probably real. Furthermore, the simulations reproduce the same effect. Therefore, we think that a model-based testing of different formulas for the droplet volume calculation is useful for the reduction of errors of the droplet volume calculated from droplet images detected by OAP.

P15L25 should be clear that size is diameter rather than radius

Done. Everywhere, diameters are used.

P15L30 see comment above re corrections

See comment above.

P16L5 This set of steps would be much simplified to the point of being obvious if the advice above is taken regarding making the equations a bit clearer and specifying which air speed is being used for Stk.

We modified the manuscript and would like to point out that the velocity used for calculating Stk number in our case is the TAS.

P17L3 Again it is not clear to me that droplet deformation as a cause of the image distortion has been proven.

The images in Figure 12 show that smaller droplets appear circular while larger particles appear deformed. We extended Figure 12 to include droplet images from another campaign. They confirm the same finding. We extended the sentence.

P17L13 Stating this as a potential limit for the drop size that can be seen as a function of aircraft speed is I think very interesting, but my gut feeling is that observed droplet breakups are caused by impacts or near impacts with the probe.

In Vargas (2012), the effect has been observed in lab experiments. This lab experiment has been verified in our simulations.

P26Fig2 It would be nice to highlight the test case.

In all figures, the test case u100_p900 is marked in blue.

P27Fig3 The lines of best fit are linear – the word polynomial should be saved for higher order equations. Replace with Linear. All plots should at least have x and y axes that start at the same value. I would ideally like to see the same max value on the x and y axes too, but I appreciate that for Fig2d, this may not be appropriate.

Probably this comment refers to Figure 2? We updated Figure 2. Axes ranges for x and y axes start and end at the same values and "polynomial" was replaced with "linear".

P27Fig4 ensure that 0 is marked on the colour bar.

0 is now marked in the colour bar.

P28Fig5 It would be nice to see the test case highlighted

P29Fig6 It would be nice to see the test case highlighted

In all figures, the test case u100_p900 is marked in blue.

P36Fig13 The lines have no proper description of what they mean – are they averages over some size range? I think they are not useful anyway and should probably be removed unless the authors can argue a good reason for them. Also 2 different shades of grey should not be used. It is hard to tell them apart.

We modified the caption adding a description of the lines. The different campaigns are now plotted with 3 different colors and markers.

We thank Peter Spichtinger for his comments on our manuscript. It was not our intention to write pejoratively about Weigel et al. (2016). We modified our manuscript based on his suggestions. In the following, the comments raised by Peter Spichtinger are marked in blue and our answers are written in black.

On behalf of all authors of Weigel et al. (2016) I would like to address some issues in the manuscript concerning the statements about our work.

1. Statement in your manuscript (page 2, lines 27-30)

> "Recently Weigel et al. (2016) proposed a more general correction method for compressible flow mainly based on thermo-dynamical calculations. However, this empirical approach is only partially considering the size-dependent effect of particle inertia on the detected concentration. Furthermore, flow disturbances induced by the aircraft wings are not considered by Weigel et al. (2016)."

The definition of ξ is not empirical but exclusively based on thermodynamic considerations and is indeed essential to account for the compressed sample air volume under measurement conditions compared to ambient (undisturbed) conditions. The inclusion of μ in the overall correction provided in Weigel et al. (2016) factually considers (not 'only partly') the size dependent effect of particle inertia. Flow disturbances by the aircraft wings are not explicitly resolved as they were not observable as such and may be implied in the compressed condition under which the measurement occurs. So, one could understand your chosen formulation as misleadingly pejorative.
Please change the phrasing in the manuscript to account for this issue.

As recommended, we modified the paragraph to make it more clear. The paragraph now reads as follows:

> Recently Weigel et al. (2016) proposed a more general correction method for particle concentrations measured by an under-wing instrument. Its first component is a compression correction factor that is based on thermo-dynamical calculations using simultaneous measurements of the instrument's pitot tube. Its second component is a size-dependent correction factor that corrects the effect of the inertia of particles larger than 70 μm, but not for smaller particles.

2. Statement in your manuscript (page 11, lines 20-22)

> "Weigel et al.(2016) provides a rougher estimation based on the concept that the air compressibility effect will cause particle accumulation near the instrument. However, the concentration at the wing instrument is apparently larger only because particles are slowed down and stay longer in the corresponding region (see Fig. 9) "

The content of the referred paper might not be fully understood by readers of your paper, since the concept is not that particles accumulate. In Weigel et al. 2016, it is explicitly stated: "Under the preliminary assumptions that the particle number per mass M of the air sample is not affected by compression (i.e. remains constant and thus n_amb/M= n_meas/M)"

This is the case if particles and air volume get compressed equivalently. Your added statement, however: "the concentration at the wing instrument is apparently larger only because particles are slowed down and stay longer in the corresponding region" is one of the messages provided by Weigel et al. (2016) from the contrary perspective: small particles are capable to move out of their initial (undisturbed) state, induced by the compression region upstream of the underwing probe, due to the approaching aircraft. Larger particles are less capable to get moved out of this undisturbed state due to their inertia. Please make the relation to Weigel et al. (2016) better visible.

The description of the different perspectives of this effect is helpful. However, a discrepancy between the results of Weigel et al. (2016) and our results remains: The inertia correction factor µ of Weigel et al. (2016) is equal to 1.00 for diameters $d_p < 70$µm, implying that these particles follow the air flow. In contrast, our simulations (see e.g. Fig. 9) show a notable impact of the particle inertia already for a diameter of 10 µm (the µ factor would be around 0.90 for density 1g/cm^3) and a strong impact for 50 µm particles (µ around 0.75) with a notable effect on concentration too (see Fig. 10).

We double-checked our results using a simplified numerical approach for the particle movement using our CFD-simulated airflow velocity fields ahead of the instrument as input and accounting for the acceleration due to the drag force on the particles. The drag force was estimated based on Eq. 3.5 of the book "Aerosol Technology: Properties, Behavior, and Measurement of Airborne Particles" by W. C. Hinds. We assumed case *u200_p250* with a particle density of 1 g cm^{-3}, a TAS of 200 m s^{-1} and an ambient pressure of 250 hPa. The results of this simplified calculation (see attached Fig. 1) confirm the results presented in our paper and thus imply that inertia needs to be taken into account also for particles with diameters smaller than 70µm. For instance, according to Fig. 1, a 30µm particle still has a velocity of about 179 m/s at the measurement location while the air velocity (PAS) is slowed down to about 142 m/s. Therefore the velocity of a 30µm particle is closer to TAS than to PAS. Even a 5µm particle shows some inertia effects, nonetheless PAS and therefore constant particle number per mass M of the air may be considered a good approximation for small particles. For a 10µm particle, however, the deviation may already be considered significant, because 10 µm particles are about 10% faster than PAS.

The revised paragraph reads as follows:

> Weigel et al. (2016) provide a method that is primarily based on the concept that the air compression near the instrument causes a corresponding densification of the number concentration of airborne particles. Subsequently, they take into account a size-dependent correction factor that corrects the effect of the inertia of large particles. Their inertia correction is mainly assessed on the basis of the circularity of images taken by an OAP at a resolution of 15 µm. Weigel et al. (2016) conclude that particles with diameters $d_p < 70$ µm follow the airflow and thus require no inertia correction. On the contrary, our simulations (see e.g. Fig. 9) show a notable impact of the particle inertia already for particle diameters of 10 µm (their speed is about 10% faster than the air; particle density 1 g/cm^3) and a strong impact for 50 µm particles (about 25% faster than air). These particle simulations are consistent with results (not shown) from a simplified numerical particle motion model using the simulated flow fields (Sect. 3.1.1) as input and Eq. 3.5 of Hinds (1999) (which is based on Clift et al. (1978)) to calculate the drag force on the particles. Therefore, we conclude that inertia needs to be taken into consideration for particles larger than about 5-10 µm.

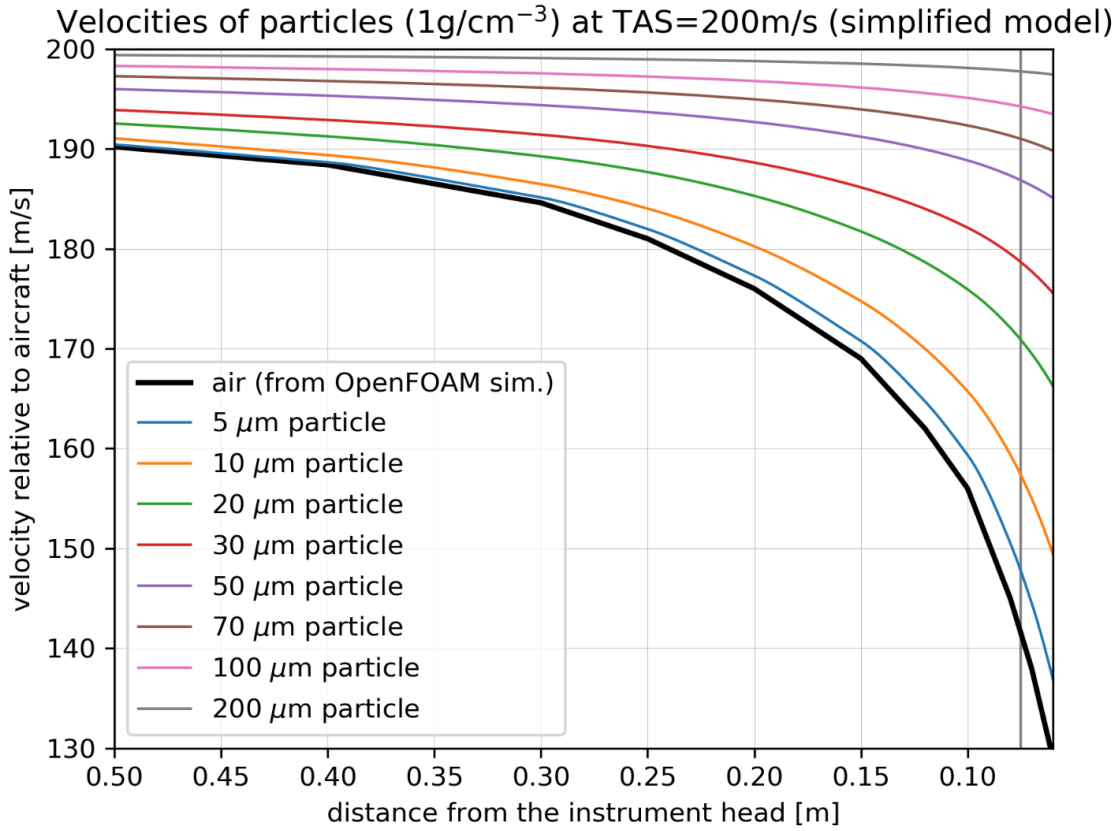

Figure 1: Velocities of air and particles of various diameters, relative to the aircraft for TAS=200m/s. The air velocity (thick black line) from the OpenFOAM simulation case u200_p250 of the discussion paper is used as input to calculate the motion of the particles caused by the drag force on the particles. The drag force is calculated based on the slip velocity particle, the corresponding Reynolds number, and Eq. 3.5 of Hinds (1999) which is based on a correlation given by Clift et al. (1978). The horizontal axis is the distance from the approaching instrument head. The grey vertical line marks the approximate location of the particle measurements.

References:

Clift, Grace, Weber: Bubbles, Drops, and Particles; Academic Press, 1978.

Hinds: Aerosol technology: properties, behavior, and measurement of airborne particles; John Wiley & Sons, 1999.

Weigel, R., Spichtinger, P., Mahnke, C., Klingebiel, M., Afchine, A., Petzold, A., Krämer, M., Costa, A., Molleker, S., Reutter, P., Szakáll, M., Port, M., Grulich, L., Jurkat, T., Minikin, A., and Borrmann, S.: Thermodynamic correction of particle concentrations measured by underwing probes on fast-flying aircraft, Atmospheric Measurement Techniques, 9, 5135–5162, https://doi.org/10.5194/amt-9-5135-2016, 2016.

amt-2019-27 – Spanu et al.

The most significant changes in the manuscript were:

- Changes directly requested by the reviewers (as indicated in our corresponding responses, see above)
- Generally, improvements with respect to language and explanation clarity
- Improved description of OAP measurement principle
- Addition of Table A1 with the different velocities used in our study
- Relation to Weigel et al. (2016) explained better
- Corrected coeffients x0, k0, k1 which are required for Eq. 6
- Addition of Eq. 7 describing directly the final step for the calculation of the ambient number concentration with our proposed method
- Addition of a new Figure 13b with unfiltered dy/dx ratios illustrating the aerodynamic squeezing of droplets larger than about 0.5 mm

All changes of the manuscript text are marked in the subsequent pages.

Flow-induced errors in airborne in-situ measurements of aerosols and clouds

Antonio Spanu[1], Maximilian Dollner[1], Josef Gasteiger[1], T. Paul Bui[2], and Bernadett Weinzierl[1]

[1]University of Vienna (UNIVIE), Aerosol Physics and Environmental Physics, Wien, Austria
[2]NASA Ames Research Center, Mountain View, CA, USA

Correspondence: Antonio Spanu (antonio.spanu@univie.ac.at)

Abstract. Aerosols and clouds affect atmospheric radiative processes and climate in many complex ways and still pose the largest uncertainty in current estimates of the Earth's changing energy budget.

Airborne in-situ sensors such as the Cloud, Aerosol, and Precipitation Spectrometer (CAPS) or other optical spectrometers and optical array probes provide detailed information about the horizontal and vertical distribution of aerosol and cloud properties. However, flow distortions occurring at the location where these instruments are mounted on the outside of an aircraft may directly produce artifacts in detected particle number concentration and also cause droplet deformation and/or ~~break-up~~ breakup during the measurement process.

Several studies have investigated flow-induced errors assuming that air is incompressible. However, for fast-flying aircraft, the impact of air compressibility is no longer negligible. In this study, we combine airborne data with numerical simulations to investigate the flow around wing-mounted instruments and the induced errors for different realistic flight conditions. A correction scheme for deriving particle number concentrations from in-situ aerosol and cloud probes is proposed, and a new formula is provided for deriving the droplet volume from images taken by optical array probes, reducing errors by up to one order of magnitude. Shape distortions of liquid droplets can either be caused by errors in the speed with which the images are recorded or by aerodynamic forces acting at the droplet surface caused by changes ~~in the airflow around~~ of the air flow when it approaches the instrument. These forces can lead to the dynamic breakup of droplets causing artifacts in particle number concentration and size. ~~Furthermore, an~~ An estimation of the critical breakup diameter ~~,~~ as a function of flight conditions is provided.

Experimental data show that flow speed at the instrument location is smaller than the ambient flow speed. Our simulations confirm the observed difference and reveal a size-dependent impact on particle speed and concentration. This leads, on average, to a 25 % overestimation of the number concentration of particles ~~larger than~~ with diameters larger than 10 µm diameter and causes distorted images of droplets and ice crystals if the flow values recorded at the instrument are used. With the proposed correction scheme~~both errors~~ , the effects on particle number concentration and image distortion, are significantly reduced by a factor of 10.

Although the presented correction scheme is derived for the DLR Falcon research aircraft (SALTRACE campaign) and validated for the DLR Falcon (A-LIFE campaign) and the NASA DC-8 (ATom campaign), the general conclusions hold for any fast-flying research ~~airplane~~aircraft.

1 Introduction

Aerosol-cloud-radiation interactions are one of the largest uncertainties in current climate predictions (Stocker et al., 2014). The size distribution of cloud and aerosol particles is a crucial parameter for aerosol-radiation and aerosol-cloud interaction (Albrecht, 1989; Rosenfeld and Lensky, 1998; Pruppacher and Klett, 2010). For example, an increase of the fraction of coarse particles can modify the direct radiative forcing of desert dust from cooling to warming (Kok et al., 2017) and also increase the reservoir of ice nucleating particles (e.g., DeMott et al., 2010).

Airborne in-situ measurements are fundamental to extend our knowledge of cloud and aerosol distributions, especially in the coarse mode. Instruments typically used by the aerosol and cloud community, for measuring coarse particles, are open path or passive-inlet[1] optical particle counters (OPCs) and optical array probes (OAPs). OPCs and OAPs measure particle flux as they record, within a time interval, the number of particles passing through a specific region named sampling area. The flux is later converted into a concentration using the air flow speed. Therefore, errors in the flow speed are directly affecting the calculated particle and cloud hydrometeor concentrations. For example, a ~~flow speed recorded too low~~ too low flow speed leads to a higher calculated particle concentration. Since the aircraft itself can influence the surrounding air and the flow measurements (Kalogiros and Wang, 2002), airborne measurements are challenging. Flow distortion caused by the fuselage and wings not only impacts the flow velocity but also modifies ~~temperature and pressurefrom~~ air temperature, pressure, and density as compared to free stream conditions thereby further affecting the aerosol and cloud measurements. ~~Furthermore, droplets can~~ For example, a higher air density leads to a higher number concentration of aerosol particles if the particle are sufficiently small to be able to follow the air flow. Furthermore, large droplets may be deformed or may even break up during high-speed sampling ~~resulting in an enhanced concentration of small droplets~~ due to aerodynamic forces acting on the droplet surface, as studied by Szakall et al. (2009); Vargas and Feo (2010). Whereas droplet deformation does not change the detected number concentrations, breakup results in enhanced droplet number concentrations (Weber et al., 1998). These shattering artifacts may originate ~~from aerodynamic or~~ not only from aerodynamic forces, but also from impaction breakup of cloud droplets and ice particles in and around the aerosol inlet (Korolev and Isaac, 2005; Craig et al., 2013). ~~Large~~ In contrast to these effects, droplets may appear ~~deformed as the result of aerodynamic forces acting on the droplet surface, as studied by Szakall et al. (2009); Vargas and Feo (2010)~~as deformed on the OAP images, but they are not deformed in reality. This is the case if the camera does not use the correct particle velocity for taking the images.

Generally, the degree of the artifact depends on the mounting position of the instrument at the aircraft and also on the flight conditions. Effects of a disturbed flow field on observed particle concentrations have been studied ~~, under the incompressible hypothesis~~ for an incompressible flow (e.g., King, 1984; King et al., 1984; Drummond and MacPherson, 1985; Norment, 1988). However, the assumption that air is incompressible does not hold for measurements on fast-flying aircraft (>100 ms^{-1}). Computational Fluid Dynamics (CFD) models are a powerful tool to study aircraft inlets (e.g., Korolev et al., 2013; Moharreri et al., 2013, 2014; Craig et al., 2013, 2014)) and sensors (Laucks and Twohy, 1998; Cruette et al., 2000), but are computationally

[1] Instruments with passive inlets are not actively sampling the air with a pump, instead they rely on the air flow resulting from the wind or the ~~airplane~~ aircraft motion.

expensive. That is why many studies considered only the instrument itself, but not the combined effect of the aircraft and the instrument.

Recently Weigel et al. (2016) proposed a more general correction method for ~~compressible flow mainly based on thermodynamical calculations . However, this empirical approach is only partially considering the~~ particle concentrations measured by an underwing instrument. Its first component is a compression correction factor that is based on thermo-dynamical calculations using simultaneous measurements of the instrument's pitot tube. Its second component is a size-dependent ~~effect of particle inertia on the detected concentration. Furthermore, flow disturbances induced by the aircraft wings are not considered by Weigel et al. (2016)~~correction factor that corrects the effect of the inertia of particles with diameters larger than 70 µm, but not for smaller particles.

In ~~this~~ the present study, the influence of ~~airflow~~ air flow distortion caused by the ~~instrument and aircraft wing~~ aircraft wing and the instrument is characterized for airborne aerosol and cloud measurements ~~. Under the hypothesis of a compressible flow, this study investigates~~ using CFD simulations with a compressible air flow. Furthermore, we investigate how different flight conditions affect particle concentrations depending on size. We propose a correction strategy valid for different ~~plane~~ aircraft configurations and passive inlet instruments. Moreover, we investigate how water droplets deform when approaching a wing-mounted instrument on a fast-flying aircraft. Errors affecting the estimation of the droplet volume from OAP images are studied using different approximating formulas. Numerical results are compared with in-situ measurements collected with a Cloud and Aerosol Spectrometer with Depolarization Detection (CAS-DPOL, Droplet Measurement Techniques (DMT) Inc., Longmont, CO, USA; Baumgardner et al. (2001)), and a second-generation Cloud, Aerosol and Precipitation Spectrometer (CAPS). The analysis is valid for a variety of wing-mounted OPC and OAP instruments used by the aerosol and cloud community. Other potential error sources affecting OPC and OAP measurements like calibration method (Walser et al., 2017), optical misalignment (Lance et al., 2010), or size-dependent sampling area (Hayman et al., 2016) are not considered in this paper.

The paper is organized as follows: section 2 introduces the methodology. For clarity, we divided the presentation of the results into two parts~~. The~~ : the first part (~~See~~Sect. 3.1) analyzes flow changes around wing-mounted instruments and their effects on derived particle concentrations. Also, a correction strategy is described. The second part (~~See~~Sect. 3.2) describes a method that ~~allows one to use for OAP measurements a corrected speed of very large particles~~provides a corrected particle speed for OAP measurements. It includes an evaluation of a parameterization of the droplet breakup process, as well as the verification of numerical results with experimental data. Different formulas for calculating the droplet volume and the undisturbed droplet diameter from OAP images are evaluated. The manuscript closes with recommendations (~~See~~Sect. 4) helping to reduce errors in airborne aerosol and cloud measurements and ~~concluding remarks~~a summary of findings (Sect. 5).

2 Methodology

The correction strategy presented in this manuscript is based on numerical simulations of ~~airflow~~ air flow and particle motion and field data collected in 2013 during the Saharan Aerosol Long-range Transport and Aerosol-Cloud-Interaction Experiment (SALTRACE, Weinzierl et al. (2017)). The primary purpose is to quantify flow-induced measurement errors and to present

a particle concentration correction scheme. The proposed correction scheme is later tested with independent datasets collected during two field campaigns, the Absorbing aerosol layers in a changing climate: aging, lifetime and dynamics mission conducted in 2017 (A-LIFE, Weinzierl and ALIFE_Team (2018)), and the Atmospheric Tomography Mission over the years 2016-2018 (ATom-1 ~~to~~ through ATom-4, Wofsy et al. (2018)).

2.1 Airborne meteorological and aerosol measurements on-board the DLR Falcon and the NASA DC-8 research aircraft

~~Our~~ The primary analysis focuses on the DLR research aircraft Dassault Falcon 20E (registration D-CMET) and is later applied to the NASA DC-8 ~~.~~ (registration N817NA).

Figure 1 shows a sketch of the DLR Falcon with a ~~wing mounted~~ wing-mounted instrument, such as the CAPS. Table 1 gives an overview of the specifications of Falcon and DC-8 including the range of typical aircraft cruise speeds and instruments used for this study. The typical altitude range covered by the DLR Falcon is below 12800 m, and ~~aircraft speed~~ the true air speed (TAS), which is the speed of the aircraft relative to the airmass flown through, ranges from 80 ms^{-1}, at low altitude, to 220 ms^{-1} at higher altitude (see Tab. 1). The DLR Falcon is equipped ~~per default~~ with a Rosemount 5-hole pressure probe model ~~R858A~~ 858 on the tip of the nose-boom (see Fig. 1), referred to as the CMET system in our study. The CMET system measures ~~inflow velocity~~ air speed and direction and has been calibrated using a cone trail (Bogel and Baumann, 1991). Bogel and Baumann (1991) estimate static pressure errors during pilot-induced maneuvers being smaller than 1 %, which converts to a 0.5 % error in derived air speed.

The NASA DC-8 can fly at altitudes up to 13800 m with ~~aircraft speeds~~ TAS between 90 and 250 ms^{-1}. During the ATom mission, the NASA DC-8 was equipped with the Meteorological Measurement System (MMS, Scott et al. (1990)). The MMS hardware consists of three major systems: an air-motion sensing system to measure air ~~velocity~~ speed and direction with respect to the aircraft, an aircraft-motion sensing system to measure the aircraft velocity with respect to the earth, and a data acquisition system to sample, process, and record the measured quantities (Chan et al., 1998; Scott et al., 1990). The uncertainty of the MMS pressure sensors is estimated to be less than 2 %.

2.1.1 Aerosol and cloud instruments

In this section, we describe the instruments used for aerosol and ~~droplet~~ cloud measurements during the different campaigns. For SALTRACE, the DLR Falcon was equipped with a CAS-DPOL mounted under the aircraft wing, hereafter named CAS. CAS is a passive inlet OPC (Baumgardner et al., 2001). Other similar open path and passive inlet instruments are the Forward Scattering Spectrometer Probe (FSSP type 100 and 300), the Cloud Droplet Probe (CDP), and the Cloud Particle Spectrometer with Polarization Detection (CPSPD) (Knollenberg, 1976; Lance et al., 2010; Baumgardner et al., 2014). The general measurement mechanism of an OPC is the following: when a particle passes through the laser beam, it scatters light, which is collected by an optical system and detected by a photo-detector. The resulting signal is then recorded and converted to the instrument-specific scattering cross section. Using scattering theory the particle size can be inverted from this cross section (e.g., Walser et al., 2017).

During A-LIFE and the ATom missions, ~~the~~ CAPS was used as the aerosol and cloud instrument. CAPS is ~~a composed~~ an instrument consisting of a second generation CAS and a Cloud Imaging Probe (CIP). CIP is an OAP~~, which was~~. OAP were introduced by Knollenberg (1970) and extensively used for droplet and ice-crystal measurements. OAPs measure particle ~~diameters~~ size indirectly with a linear array of photodiodes (64 in the case of CIP) by detecting the shadow formed by the particle passing through a collimated laser beam (λ = 658 nm in case of CIP). The CIP ~~'s unit acquires a full particle image by assembling a sequence~~ acquires 2-D images of the particles and hydrometeors by assembling sequences of image slices. In order to reconstruct the correct length of a particle along flow direction it is critical that the particle speed assumed for image creation, hereafter named OAP reference speed, represents the real particle speed. The image acquisition frequency, ~~named shutter speed of the camera, should be proportional to the particle speed~~ i.e. the speed with which the CIP records image slices, is usually set according to the OAP reference speed such that each image pixel represents in both dimensions the same lengths. CIP's working mechanism is similar to those other OAPs like 2D-S ~~, HVPS , and SID-2 (Knollenberg, 1981; Lawson et al., 2006; **?**)~~ or HVPS (Knollenberg, 1981; Lawson et al., 2006).

2.1.2 Measurement of ~~airflow~~ air flow and flow distortion effects caused by the aircraft~~fuselage~~

The DLR Falcon is equipped with four hard points under the aircraft wings to carry up to four instruments inside standard canisters (developed by Particle Measuring Systems). Canisters have an outer diameter of ~ 0.177 m with a 1.25 m length and are mounted with 3.5-degree angle with respect to the wing (see the green arrow in Fig. 1).

~~Most~~ As we described, OPC and OAP measurements depend on the flow, therefore wing-mounted instruments are sometimes equipped with flow sensors to constrain local flow conditions. Commonly used sensors are pitot-static tubes, hereafter referred to as pitot tubes (Letko, 1947; Garcy, 1980). ~~Pitot-tubes~~ Pitot tubes are usually located to measure flow conditions ~~at~~ representative for the sampling area. A pitot tube measures total pressure p_{tot} and the static pressure p_s. p_{tot} is the sum of the static and the dynamic pressure q_c and is a measure of the total energy per unit volume. Consequently, p_{tot} should not change around the ~~airplane~~ aircraft if dissipative processes ~~,~~such as a shock wave ~~,~~do not occur. Table A1 summarizes the different velocities referred to in this study. At small Mach numbers ($M = U/U_{sound}$<0.3, approximately corresponding to 100 ms^{-1} at sea level), ~~airspeed~~ air speed U can be derived using the incompressible form of Bernoulli's ~~Equation~~equation. When the ~~airspeed~~ air speed increases (M>0.3), air density cannot be considered independent of velocity. For this reason, a generalized Bernoulli's equation is needed~~:~~, which is given by

$$\int_{p_1}^{p_s} \frac{dp}{\rho} \frac{dp}{\rho_{air}} + \frac{U^2}{2} = \text{const.} \tag{1}$$

p_1 is a static reference pressure and the air density ~~ρ~~ ρ_{air} is a function of pressure. Using the heat capacity ratio γ and ~~$U_{sound} = \sqrt{\gamma p_s/\rho}$~~ the sound speed $U_{sound} = \sqrt{\gamma p_s/\rho_{air}}$ for an adiabatically expanding gas, the following expression can be derived ~~:~~ as

$$\frac{p_{tot}}{p_s} = \left(1 + \frac{\gamma - 1}{2} M^2\right)^{\frac{\gamma}{\gamma - 1}}. \tag{2}$$

It is assumed that the pitot tube is oriented parallel to the air flow. Eq. 2 can be converted to obtain the ~~flow speed~~ air flow speed

$$U = \sqrt{\frac{2\gamma}{\gamma-1}\frac{p_s}{\rho}\left(\left(\frac{p_{tot}}{p_s}\right)^{\frac{\gamma-1}{\gamma}}-1\right)}\sqrt{\frac{2\gamma}{\gamma-1}\frac{p_s}{\rho_{air}}\left(\left(\frac{p_{tot}}{p_s}\right)^{\frac{\gamma-1}{\gamma}}-1\right)}. \quad (3)$$

~~Therefore,~~ Equation 3 shows that errors of pressure-based ~~airspeed instruments~~ air speed measurements are related to the static pressure as well as to the dynamic pressure (Nacass, 1992). Static pressure errors are typically introduced by disturbances in the flow field around the aircraft and ~~mostly~~ mainly depend on the location and design of the pitot tube (Garcy, 1980). The amount by which the local static pressure at a given point in the flow field differs from the free stream static pressure is ~~called the positional~~ the so-called position error.

Errors in the measured dynamic pressure may occur due to air flow disturbances caused by the aircraft or by excessive flow angularity, for example when flying with a large angle of attack (>~~5~~10^o). ~~In this last case, which~~ , i.e. a large angle between the flow and the probe axis. A large angle of attack may occur during fast ascent or descents or steep turns of the aircraft. In that case, the fluid stream is ~~not anymore~~ no more parallel to the instrument head and errors occur in both, total and static pressure readings (Sun et al., 2007; Masud, 2010). ~~For~~ When the DLR Falcon ~~, when flying in normal condition, i.e. avoiding steep turns, the attack angle~~ flies under typical operating conditions during research flights the angle of attack is small enough to have only a negligible contribution to the error of the dynamic pressure.

The True Air Speed (TAS), i.e. the speed of the air in the free stream, can deviate from the Probe Air Speed (PAS), i.e. the ~~airspeed measured at the probe location~~ air speed at the location of the probe which may have a flow sensor as described above. King (1984) estimated the difference between TAS and PAS being smaller than 10 % and varying as the inverse square of the scaled distance from the aircraft nose. However, the estimation of King (1984) relies on an incompressible fluid. ~~Using the incompressible~~ , but using the Bernoulli's equation ~~will lead~~ for incompressible flow leads to a 10 % overestimation of ~~airspeed~~ air speed (as compared with a compressible flow) with an 8 % error in pressure as the aircraft approaches transonic speeds ($M \sim 0.8$). Therefore, because of the air compressibility, differences between TAS and PAS can be larger than 10 % in reality.

The CAS is equipped with a 17 cm pitot tube, whereas the CAPS has a 24 cm long one to represent the conditions in the CIP sampling area. Pressure sensors have been statically calibrated by the manufacturer. Therefore, the ~~positional errors~~ position error can be estimated using the ~~deviances~~ deviations between the CMET measurements, representing the free stream conditions, and the ~~wing mounted~~ wing-mounted instrument reading. Figure 2 shows a statistical comparison between temperature (a), dynamic pressure (b) and static pressure (c) values recorded by the CMET system at the nose boom (free stream) and by the CAS instrument. In Fig. 2d TAS_{CMET} is compared with the PAS calculated using the pitot tube data according to Eq. 3. Pixels are color coded with the statistical frequency of the binned data. Red lines in Fig. 2a-c are ~~polynomial~~ linear fits of the data with calculated R-squares values.

As indicated by the deviation from the 1:1 line (dashed), wing-mounted instruments experience an overpressure on their static sensors (Fig. 2b). Since the total pressure is constant along the ~~plane~~aircraft (within the pressure sensors errors), a higher static pressure p_s results in a lower dynamic pressure q_c (Fig. 2c). Consequently, the calculated PAS is on average 30 % lower

than TAS, with a 35 % maximum relative deviation at higher speed (Fig. 2d). To ~~investigate the discrepancy~~ understand the differences between PAS and TAS, we use a numerical model.

2.2 Numerical models

2.2.1 Flow model

As ~~discussed before, the incompressible hypothesis~~ mentioned earlier, the assumption of incompressibility of air is not valid for fast-flying aircraft ($M > 0.3$) such as the DLR Falcon and the NASA DC-8~~and a~~. A more general model including air compressibility is needed. Here, we use a numerical model based on the time-averaged Navier-Stokes ~~equations~~ equation for compressible flows (Johnson, 1992). The numerical solution is obtained using a modified version of the rhoSimpleFoam solver from the finite volume code OpenFOAM v4.0.x (Weller et al., 1998). The solver calculates a steady state solution with a segregated approach using a SIMPLE loop, with the latter solution solved using the Reynolds Averaged Navier-Stokes equations (RANS) with a LaunderSharmaKE (Launder and Spalding, 1974) turbulence model. Nakao et al. (2014) successfully used OpenFOAM for simulating the ~~airflow~~ air flow on a two-dimensional NACA (National Advisory Committee for Aeronautics) wing profile under different attack angles.

In our case, we use a simplified three-dimensional model of the Falcon wing equipped with a ~~Probe Measurement System~~probe measurement system, which consists of a pylon and a cylindrical canister mounted under the wing (see Fig. 1). The tube of the CAS with the passive inlet was not modelled since preliminary simulations showed that the effect of the CAS tube on the concentrations measured by CAS is smaller than 5 %. For simplicity, we reduced the complexity of the parameter space using a constant angle of attack of 4^o which is the median value derived from the flight conditions. We adopt a comparatively large model domain with edge lengths of 10 times the instrument length to minimize the effects of the domain boundaries. The model mesh comprises $8 \cdot 10^6$ elements. The dependency of the results on the number of mesh elements was tested, using different meshes (created with snappyhexmesh (Montorfano, 2017)), until we found convergence of the results. To separate CFD results from the statistical analyses conducted over the measured dataset we refer to the simulated velocity as ~~$\boldsymbol{U}$~~ U being the absolute value of the three-dimensional velocity vector. U_0 is the velocity in the free stream of the simulations. With this notation ~~$|\boldsymbol{U}_0|$=TAS.~~ U_0 is equal to TAS.

2.2.2 Particle motion

To describe particle motion, we adopt an Eulerian-Lagrangian approach: the Eulerian continuum equations are solved for the fluid phase (see ~~Sec~~Sect. 2.2.1) ~~, while~~ whereas Newton's equations ~~described~~ describe the particle motion determining their trajectories. We assume spherical particles with a density ρ_p = 2.5 gcm^{-3} for mineral dust and ρ_p = 1 gcm^{-3} for water droplets. We use a one way-coupling, i.e. we ~~only consider the flow action on~~ consider flow-induced drag forces on the particles. According to Elgobashi (1991), ignoring the effect of particle motion on the flow itself (two-way coupling) and inter-particle collisions (four-way coupling) is a reasonable assumption for volumetric particle fractions smaller than 10^{-6}. For dust particles, this corresponds to atmospheric concentrations lower than 2.5 gm^{-3}. This value is ~~about~~ at least two orders

of magnitude larger than concentrations measured in dense desert dust aerosol layers (e.g., Kandler et al., 2009; Weinzierl et al., 2009, 2011; Solomos et al., 2017) or volcanic ash layers (e.g., Barsotti et al., 2011; Poret et al., 2018). Single particle motion is resolved using a Lagrangian model where motion equations are integrated in time. The considered forces acting on a particle are the pressure gradient, the drag force, and the gravity.

2.2.3 Droplet distortion model

Fast As described in the introduction, fast changes in the airflow air flow can modify the shape of water droplets causing droplet break-up breakup and consequently strongly affecting the measured number concentration. To Here, we use a droplet deformation model to describe how the flow affects the shape of water droplets measured by OAP instruments mounted underwingwe use a droplet deformation model. A large body of research exists on droplet deformation and breakup (Rumscheidt and Mason., 1961; Rallison, 1984; Marks, 1998). The droplet dynamics is crucial for estimating the icing hazard of supercooled droplets on an aircraft wing (e.g., Tan and Papadakis, 2003). Flow changes experienced around the wing can have important consequences especially when sampling supercooled droplets, for example in case of mixed-phase clouds. Jung et al. (2012) observed how shear could cause almost instantaneous freezing in supercooled droplets. Vargas and Feo (2010); Vargas (2012) used laboratory observations to investigate the deformation and breakup of water droplets near the leading edge of an airfoil. Droplet breakup, as effect of an effect of the instability caused by shear on the droplet surface, was early studied by Pilch and Erdman (1987) and Hsiang and Faeth (1992). Different analytical models exist for describing a droplet in a uniform flow such as the Taylor Analogy Breakup (TAB) model (O'Rourke and Amsden, 1987), Clark's model (Clark, 1988) and the Droplet Deformation and Breakup (DDB) model by Ibrahim et al. (1993). Vargas (2012) modifies the DDB model including to include the effect of a changing airflowair flow. However, this model not fully agrees does not fully agree with the experimental data especially for particles with diameters larger than 1000 µm. Here we use a volume-of-fluid volume of fluid (VOF) method (Noh and Woodward, 1976) to determine droplet deformations as a function of droplet size and flight conditions (p_s, T, TAS). Droplets are initially assumed to be spherical with diameter d_0. Similar to the TAB model a simplified problem is considered assuming that droplets are radially symmetric along the flow.

Sampled droplets experience a change of relative airspeed slip velocity U_{slip} (speed of particle relative to the air around it) when approaching the instrument. For this reason, we simulate a transitional state where the airspeed air speed varies from zero (still air) to its final value TAS-PAS TAS minus PAS (when the droplet is passing through the sampling area). The applied velocity values are calculated along the simulated trajectory of the droplet (of given d_0) and imposed as boundary conditions. Similar to Vargas (2012) we assume that the droplet does not exchange heat with its surroundings and the only forces involved in the deformation of the droplet are viscous, pressure and surface tension forces.

The numerical method relies on the solver InterFoam included in OpenFOAM. Numerical schemes for solving the flow are second-order implicit schemes both in the spatial and in the temporal discretization (Rhie and Chow, 1982). The Courant number, i.e. the flow speed multiplied by time resolution and divided by space resolution, is limited to 0.8 globally and to 0.2 at the interface, and the domain size is ten times larger than the droplet, as suggested by Yang et al. (2017). The simulations have been performed with a water to air density ratio of 1000:1. Surface tension decreases with temperature from σ=0.75 Nm^{-1}

at T=278 K to σ = 0.7 Nm^{-1} at T=305 K (Vargaftik et al., 1983). The effect of a change in droplet surface tension due to the presence of impurities is not considered which seems to be a reasonable assumption given that salts increase the surface tension of seawater only by less than 1 % (Nayar et al., 2014).

3 Results and discussion

3.1 Airflow ~~distorsion~~ distortion and particle concentration

Aerosol concentrations are usually expressed as particle number (or mass) per unit volume. Since the aerosol particles are embedded in the air, and the air density depends on pressure and temperature, the aerosol concentration depends as well on these parameters. Therefore, sampling conditions, e.g. the flight level pressure or the flow-induced pressure distortion at the measurement location, influence the concentration measurement directly.

3.1.1 Measured and simulated ~~airflow~~air flow

To understand the effect of different flight conditions on the measurements, we selected 11 test cases (see Tab. 2) with initial data (p_s, T, TAS) chosen from flight conditions recorded during SALTRACE. Figure 3 shows a frequency histogram of the static pressure p_s and the TAS recorded by the CMET system during the SALTRACE campaign. The colored dots represent the 11 selected cases. Only certain combinations of p_s and TAS represent typical flight conditions for the DLR Falcon. For example, low pressure (high altitude) is associated with higher aircraft speed (when air density is lower, the aircraft needs to fly with a higher speed to have the same lift). As an example for all test cases, we first analyze the result for the specific test case u100_p900 (TAS=100 ms^{-1} and ~~p~~p_s=900 hPa, see Tab. 2). Figure 4 shows the simulated ~~airflow~~ air flow in a vertical plane around the Falcon wing ~~mounted with~~ where the simplified probe ~~(light gray~~ is mounted (white region). The local pressure (a) and the ~~airspeed~~ local air speed (b) are expressed as ~~the deviation in percentage~~ relative deviations (in percent) from free stream conditions. ~~In a~~ During flight, the pressure above the aircraft wing is lower than in the free stream, while the pressure below the wing is higher, resulting in a lower ~~airspeed~~ air speed at the wing-mounted probe compared to free stream conditions (Fig. 4b). Pressure and velocity changes in front of an obstacle are a function of the distance from the obstacle. In case of an incompressible flow, Stokes provided an analytical expression for the velocity field in front of a sphere. However, in the case of a compressible flow, a necessary assumption for a ~~fast airplane~~ fast-flying aircraft (TAS>150 ms^{-1}), analytical solutions have not been found yet. Figure 5 shows the ratio between the local conditions near the probe and free stream conditions for pressure (a) and air speed (b) as a function of the distance from the instrument head. The different colors represent a selection of test cases with different TAS (increasing from light-blue to brown). The gray round shape symbolizes the simplified instrument mounted in a canister below the aircraft wing. The pitot tube is sketched in dark gray. The location of the static ~~ports~~ port is marked with a vertical red line~~. The sampling area , which~~ , whereas the location of the tip of the pitot tube is marked with a light gray line. Note, that the sampling area of the instrument is located at the same horizontal distance from the instrument head as the tip of the pitot tube, ~~is marked with a~~ thus conditions at the light gray line should be representative for the location

of the aerosol measurement. Contrary to the incompressible case, where the ratio ~~U/U$_0$~~ U/U_0 is independent of the ~~airspeed~~air speed U_0 (TAS), here due to compressibility the ratio is changing with ~~U$_0$. As visible~~ U_0. An incompressible case in Fig. 5b ~~, airspeed differences~~ would be similar to the u75_p1000 simulation where the compression effect is still small. As visible in this figure, the relative air speed difference between the free stream and the instrument ~~increase at higher TAS, and is larger than the incompressible case~~location increases with TAS.

Errors in the pressure ~~are generally~~ measurement can arise due to the position of the static port ~~. As explained by Barlow et al. (1999) , for~~ relative to the tip of the pitot tube. For a pitot tube in a laminar flow ~~,~~ errors are a function of the pitot tube length and the static port distance from the tip (Barlow et al., 1999). For CAS, ~~static ports are~~ the static port is located 44 ~~mm downstream from~~ mm downstream of the tip. According to Fig. 5a this difference will lead to a deviation in the pressure since the pressure is ~~exponentially decreasing~~ decreasing exponentially as a function of the distance from the probe head. ~~For the considered~~ However, these differences are still small compared to the position error. For example, considering the numerical test case u100_p900 (see Fig. ~~4) the numerical simulation shows a 1 % error in the~~ 5) a CAS pitot tube reading will overestimate p_s ~~with an estimated deviation of U from~~ by 2.5 % and underestimate air speed by 26 % as compared to the free stream ~~airspeed of 23 %~~values.

~~Figure 6 compares the ratio of~~ To understand the differences between the free stream conditions and the conditions at the wing-mounted instrument we analyzed the data collected during SALTRACE and compared them with the results from the numerical simulations. Figure 6 shows a statistical analysis of ratios between values read by the CAS pitot tube and the CMET system during SALTRACE for temperature (a), static pressure (b) and ~~airspeed~~ air speed (c). ~~Different~~ The histogram color map refers to the number of seconds of available 1 Hz data of these ratios as function of specific T_{CMET}, $p_{s,CMET}$, TAS_{CMET}. The different marker colors indicate the selected simulation test cases described in Tab. 2. The simulation results ~~refer to~~ in Fig. 6 are valid for the pitot tube static port location. The temperature difference between free stream conditions and the probe is decreasing from 3.5 % to 0.5 % with increasing temperature. This effect is a response to a lower ~~airplane~~ aircraft speed at low altitude (see Fig. 3). Also, the trend of the pressure difference in Fig. 6b shows a similar behavior decreasing from 20 % at high to 1-2 % at low altitude. Local conditions differ from free stream also for ~~airspeed~~ air speed as shown in Fig. 6c with ~~airspeed~~ air speed being 25 % to 35 % lower at the probe location compared ~~with~~ to the free stream. In this context, it is worth mentioning that a longer pitot tube, as in the case of CAPS (as compared to the CAS used during SALTRACE), will reduce ~~positional errors~~the position error because the deviation of the pressure in front of the probe from the free stream pressure is exponentially decreasing with increasing distance from the probe head. Indeed, the differences between TAS_{CMET} and PAS_{CAPS} are only 15 % to 20 % (see Appendix, Fig. A2). The simulated conditions at the pitot tube location well represent the measured data from the SALTRACE campaign with small deviations (see Fig. 6). The systematic differences in temperature need a separate explanation. Like pressure also the temperature is ~~changing with distance from airplane body~~ increasing near the probe head. For this reason, temperature measurements are sensitive to the measurement location. In the CAS and CAPS instruments, the temperature sensor is installed in the back, and the temperature measurement is corrected using the Bernoulli equation to obtain the temperature at the pitot tube. Consequently, errors in pressure will lead to an error in the temperature. This provides a possible explanation for the 1 % difference between the ~~measurements~~ temperature values obtained from the instrument and the

simulations (Fig. 6a). The temperature bias is probably due to a combination of static pressure bias, instrumental uncertainty, and model ~~parametrization. Howsoever~~parameterization. Nevertheless, an error of 1 % in T will lead, according to Eq. 3, to a PAS error smaller than 0.5 %~~and thus can be considered~~. Thus, the uncertainty of the temperature has only a very small contribution to the uncertainty of the PAS and is therefore negligible.

3.1.2 Simulated particle concentrations and sampling efficiency

~~Using the~~ In this section, we use simulated flow fields ~~, we study the interaction of the flow with the particles, as explained in section 2.2.2~~(Sect. 2.2.2) to study how the air flow around a wing-mounted instrument affects the particles. For each class of particles with a different density ~~and diameter~~ρ_p and diameter d_p, we release $2 \cdot 10^5$ particles upstream the ~~wing-mounted~~ instrument at the domain border ~~. For each particle class, we~~ and calculate the sampling efficiency f_{eff} as the ratio between particles passing through the sampling area and particles released ~~in the free stream. These numbers are normalized by the ratio of the releasing area to the sampling area. This is done by using of~~ at the domain border. Counting the particles is done using a Gaussian kernel that reduces the dependency of the estimated particle concentration ~~from~~ on the computational grid (Silverman, 1986). These numbers are normalized by the ratio of the releasing area to the sampling area. Figure 7 shows an example of streamlines around the wing-mounted instrument. Contours are color-coded with ~~pressure~~ density ρ_{air} and streamlines with ~~flow speed . Particles slow down~~ air speed U. Air speed decreases in the vicinity of the probe ~~. Due~~ and streamlines are bent due to the flow distortion caused by the overpressure~~streamlines are bent~~. This effect has been observed already by King (1984). The ability of particles to adapt to flow changes is expressed by the Stokes number Stk. The Stokes number represents the ratio of ~~particles~~ particle's response time to the characteristic fluid time scale. Particles with a small Stokes number react immediately to flow changes and consequently follow the streamlines, as in the case of ~~submicron particles. Here, to~~ submicron-sized particles. To generalize the analysis according to Israel and Rosner (1982) ~~,~~ into the non-laminar flow regime, we use instead of the original Stokes number Stk a modified Stokes number ~~is used, hereafter called Stokes number~~ Stk^*, which is defined as ~~:~~

$$Stk^* = \frac{\rho_p U d_p^2}{L 18 \mu_{air}} \psi(Re_p) \text{ where } Re_p = \frac{pUd_p}{(T \cdot 287.058)\mu_{air}} \frac{p_s U d_p}{(T \cdot 287.058)\mu_{air}}. \quad (4)$$

μ_{air} is the dynamic viscosity of air, and ψ ~~a~~ the additional correction factor as a function of particle Reynolds number (Re_p) varying from 1 in the laminar case to ~~0~~ values smaller than 0.1 in the case of fully turbulent flow ~~(Israel and Rosner, 1982)~~ (see Fig. 3 of Israel and Rosner (1982) for $\psi(Re_p)$). L is a characteristic fluid length, here fixed to 1 m. The TAS is used for U in Eq. 4. Figure 8 shows the sampling efficiency as a function of the Stokes number Stk^*. Different symbol colors represent particle diameters whereas ~~different line colors~~ the differently-colored lines represent fits of sigmoid functions to the Stokes numbers of the selected test cases. The ~~instrument~~ sampling efficiency f_{eff} is well approximated by the sigmoid fits. In the appendix, Tab. A3 presents the sampling efficiencies of the selected test cases ~~as a function of the particle diameter and density~~for different particle diameters and densities. For large Stokes numbers, the simulated droplet concentration at the probe is minimally affected by the flow. For example, $f_{eff} > 95\%$ holds for ~~particles~~ diameters larger than 100 µm. For small particles with less inertia, the effect caused by the flow is more evident, and it leads to a sampling efficiency of ~~75~~ 77 % (test

case u100_p900). This effect appears less marked for test cases at higher TAS and lower pressure, e.g. for u200_p250 where 80 % of the small particles reach the sampling area. It is worth mentioning that simulations considering only the wing itself without the instrument (not shown) result in f_{eff} values around 91-92 % for small Stk^* illustrating that both the wing and the instrument affect the flow at the sampling location.

The change of particle inertia as a function of particle diameters plays a significant role also in the particle velocity. As King (1984) reported, particle speed v_p may significantly differ from the local ~~airspeed~~ air speed depending on their Stokes number. Figure 9 shows the particle speed v_p normalized by PAS (a) and TAS (b) for the selected test cases. Different colors represent different particle diameters and marker thickness is a function of the TAS. For each simulated case, particle speed is calculated as an average of the sampled particles. For diameters smaller than 5 µm, PAS is a reasonable approximation of particle speed. Larger particles ~~, having~~ with a higher Stokes number, are less influenced by the air flow change due to their inertia. For this reason ~~, as visible in Fig. 9b, the~~ the particle velocity v_p ~~of particles larger than 50~~ for diameters $d_p > 50$ µm can be well approximated using the TAS with an error smaller than 10 % ~~. From~~ (see Fig. 9b). Fig. 9b ~~it is visible~~ also shows that at higher TAS (see gray arrow) the normalized particle speed is lower, especially for smaller particles~~. This is due to the air compressibility effect on airspeed, as discussed in~~ , because of the lower normalized air speed (Fig. 5~~, whereas TAS minimally affects the normalized speed of larger particles~~).

3.1.3 Compressibility effect on concentration: a correction strategy

The PAS is lower than TAS (during SALTRACE, PAS/TAS$\simeq$ 70 %, see Fig. 6c). Thus, for a given number of particle counts per time interval, particle number concentrations, calculated using PAS as a reference speed, are larger than values obtained using TAS. Furthermore, the ~~pressure and the temperature~~ temperature and the pressure at the probe are higher than ~~at~~ in the free stream as shown in Fig. 6a and b. Wrong temperature and pressure values will lead to errors of the concentration values after conversion to other conditions, e.g. those ~~at~~ in the free stream. A higher pressure value leads to a lower calculated concentration, whereas it is directly proportional to the temperature value used.

Weigel et al. (2016) provide a method to derive ambient number concentration from data of underwing instruments that is primarily based on the concept that the air compression near the instrument causes a corresponding densification of the number concentration of airborne particles. Subsequently, they take into account a size-dependent correction factor that corrects the effect of the inertia of large particles. Their inertia correction is mainly assessed on the basis of the circularity of droplet images taken by an OAP at a resolution of 15 µm. Weigel et al. (2016) conclude that particles with diameters d_p<70 µm follow the air flow and thus require no inertia correction. On the contrary, our simulations (see e.g. Fig. 9) show a notable impact of the particle inertia already for particle diameters d_p = 10 µm (their speed is about 10% higher than the air speed; particle density 1 gm^{-3}) and a strong impact for 50 µm particles (about 25% faster than air). These particle simulations are consistent with results (not shown) from a simplified numerical particle motion model using the simulated flow fields (Sect. 3.1.1) as input and Eq. 3.5 of Hinds (1999) (which is based on Clift et al. (1978)) to calculate the drag force on the particles. Therefore, we conclude that inertia needs to be taken into consideration for particles larger than about d_p>5-10 µm.

The main idea of our concentration correction strategy is to express the sampling efficiency f_{eff} as a function of the Stokes

number and a parameter α describing the difference between the probe and the free stream conditions ~~:~~

$$\alpha = \frac{p_{free}}{p_{probe}} \frac{T_{probe}}{T_{free}} \frac{TAS}{PAS}. \tag{5}$$

Using α as variable, the sampling efficiency f_{eff} can be approximated with the ~~equation:~~ sigmoid equation

$$f_{eff}(\alpha, Stk^*) = k_1 \frac{100 - k_1}{1 + e^{-k_0(\log(Stk) - x_0)}} + \frac{100 - k_1}{1 + e^{k_0 \cdot x_0} \cdot (Stk^*)^{-k_0}}. \tag{6}$$

The sampling efficiency values used for the fits were calculated from the simulation results for different flight conditions and for different distances from the probe. The coefficients in Eq. 6 are obtained by linear regression on α: x_0 = ~~0.009~~0.857 · α ~~-5.46~~ 5.39, k_0 = ~~0.003~~0.505 · α + ~~2.157~~ 2.00 and k_1 = ~~0.87~~85.0 · α + ~~11.5~~13.5. Equation 6 allows correcting particle concentrations as a function of the Stokes number and flight conditions. For each particle diameter d_p, the first step of the correction is to estimate the corresponding Stokes number (Eq. 4) using free stream conditions (p_s, T, TAS) and a range of particle densities. Secondly, the sampling efficiency f_{eff} is calculated using the Eq. 6. ~~For the calculation of α also the probe conditions are needed. Finally, particle concentrations calculated using free stream conditions are corrected for each diameter by division by the corresponding sampling efficiency value f_{eff}~~Finally, the ambient number concentration N_i in each diameter bin i (covering the diameter interval from $d_{p,i}$ to $d_{p,i+1}$) is calculated as follows

$$N_i = \frac{\text{number of detected particles in bin } i}{\text{size of instrument's sampling area} \cdot \text{TAS} \cdot \text{measurement duration} \cdot f_{eff}(d_p)} \tag{7}$$

Note, that Eq. 6 is an extension of the formula by Belyaev and Levin (1974) where the deviation of the sampling efficiency from unity was found (via a direct method) to be a sigmoid function of the stokes number and to be proportional to (PAS/TAS - 1).

Fig. 10 compares estimated sampling efficiencies with sampling efficiencies obtained directly from the simulations. Two different estimation methods are considered to illustrate the benefit of ~~our~~ the new correction strategy proposed here. In the 'Old Method' (Fig. 10a) concentrations are calculated using PAS as reference speed, which are then corrected with an adiabatic expansion between the probe and free stream conditions. In contrast, the 'New Method' (Fig. 10b) uses TAS as reference speed and the fitted sampling efficiency f_{eff} sigmoid function from Eq. 6. The concentrations calculated with the ~~Old Method~~ 'Old Method' are correct for describing the behavior of small particles (see Fig. 10a). Small particles exhibit enough mobility to ~~be considered acting like the flow. By~~ follow the air flow. In contrast, using probe conditions (PAS) and an adiabatic expansion overestimates the particle number concentration by up to 25 % for coarse mode particles (d_p>2 µm). This difference will grow even larger if ~~airspeed~~ PAS deviates more from ~~free stream conditions. The New Method~~ TAS. The 'New Method' (Fig. 10b) ~~, based on our correction strategy,~~ shows good agreement ~~,~~ with deviations smaller than 2 % for the complete size range. The ~~New Method also~~ 'New Method' not only has the advantage of reducing ~~errors that otherwise will depend on the particle diameter. Weigel et al. (2016) provides a more rough estimation based on the concept that the air compressibility effect will cause particle accumulation near the instrument. However, the concentration at the wing instrument is apparently larger only because particles are slowed down and stay longer in the corresponding region (see Fig. 9). OPCs measure particle flux, by~~

counting single particles passing through the sampling area, hence they are not influenced by the mentioned compressibility effect. This effect is influencing other aerosol instruments measuring directly bulk concentration such as the Hot-wire or depending on it, as the case of the Back-scatter Cloud Probe (BCP). concentration errors but it also reduces the size-dependence of the these errors.

3.1.4 Reducing positional errors for OAP

OAP size range mostly covers particles larger than 10

3.1.4 Reducing OAP errors related to OAP reference speed

The OAP reference speed is usually derived from measurements with a pitot tube being part of the OAP, thus by default represent local conditions. As explained in Sect. 2.1.1 the OAP reference speed is critical for the correct reconstruction of the particle size in the direction of the flow. OAP instruments mainly cover particle diameters larger than 30 µm. As shown in Fig. 9particle speed in this range b shows that particle speed v_p in this size range is close to TAS, i.e. v_p is minimally affected by the flow (see Fig. 9b)around the aircraft. Thus, TAS is a good approximation for the OAP instrument reference speed, for calculating the time frame and therefore reducing images distortion errors. Using using the PAS as a reference speed for the OAP OAP reference speed will result in images flattened along the flow direction, with a relative error proportional to the offset from the free stream. The main idea is to use the pitot tube to measure free stream conditions by calibrating relative offset of PAS from TAS. On the contrary, TAS is a good approximation for the OAP reference speed minimizing image distortion errors. Therefore, the basis of the correction method proposed here is to calibrate the pressure sensors such that positional errors are minimized. Similar to the analysis shown the pitot tube of the OAP reports TAS instead of PAS. This can be achieved by performing a similar analysis as presented in Fig. 2,. In our case, the CAPS pitot tube was calibrated using the free stream conditions collected by re-calibrated using data from the CMET system : a polynomial fitbetween together with simultaneous measurements of CAPS during some test flights. A linear fit[2] between the free stream conditions and instrument ones is used from the CMET system and the probe conditions from CAPS is performed for q_c and $p_s$collected during some test flights[3]. A similar analysis is was conducted using NASA DC-8 data provided by the MMS during the ATom missionsfor ATom-2, ATom-3, and ATom-4.

Figure 11 shows the ratio of airspeed measured with the wing-mounted probe and the free conditions the air speed reported by the CAPS instrument and the TAS during the NASA DC-8 campaigns ATom-1 (a, 2016), ATom-2 (b, 2017), and the Falcon

[2]For DMT's instruments, like the CAPS, the pitot tube calibration can be done modifying in the PADS acquisition software the file "config.ini" with the coefficients obtained with the linear fit. Since in PADS temperature measurements are derived using the Bernoulli equation, reported values depend on the dynamic pressure. Consequently, the temperature values need to be recalculated during the post-processing, using the dynamic pressure at the probe obtained by inverting the fit coefficients.

[3]For DMT's instruments, like the CAPS, the pitot tube calibration can be done modifying in the PADS acquisition software the file "config.ini" with the coefficients obtained with the polynomial fit. Since in PADS temperature measurements are derived using the Bernoulli equation, reported values depend on the dynamic pressure. Consequently, the temperature values need to be recalculated during the post-processing, using the dynamic pressure at the probe obtained by inverting the fit coefficients.

campaign A-LIFE (c~~). During A-LIFE and ATom-2 the pitot tube probe~~ , 2017). Whereas during ATom-1 the CAPS pitot tube calibration was based on the manufacturer settings reporting PAS, the CAPS pitot tube was calibrated to match free stream conditions reporting TAS during ATom-2 and A-LIFE. The obtained ~~airspeed~~air speed during ATom-2 and A-LIFE, named hereafter TAS_{CAPS}, shows on average a 2 % deviation from the TAS_{CMET} and 3 % from TAS_{MMS}. Contrary, during ATom-1, the uncorrected PAS_{CAPS} shows an offset with the TAS_{MMS} larger than 15 % (see Fig. 11a).

~~In the following we evaluate OAP image distortions along the flow to estimate the correctness of the assumed particle speed v_p. Since ice crystals mostly present irregular shapes, we limit our analysis to liquid droplet images.~~

3.2 Droplet deformation

The recorded shape of droplets using an OAP is a combination of the real particle shape influenced by the sampling conditions and~~instrumental errors~~ , as discussed above, instrumental effects such as those resulting from the ~~wrong speed setting. A wrong speed setting will lead to a wrong frequency of image recording, for example using a lower speed results in squeezed images along the air flow direction , as discussed above~~settings to calculate v_p. In the following we evaluate OAP image distortions along the flow direction to estimate the correctness of the assumed particle speed v_p and to investigate aerodynamic effects on the real droplet shape. Since ice crystals mostly present irregular shapes, we limit our analysis to liquid droplet images.

Figure 12 shows ~~a sequence~~ sequences of gray-scale images taken with the CIP in ~~a cloud passage during the A-LIFE campaign. Pressure and temperature conditions (p=840 , T=298)~~cloud passages during the ATom-4 campaign. The vertical dimension (y-axis) of these images is the dimension of the optical array (being perpendicular to air flow direction) and the horizontal dimension (x-axis) initially is the time dimension, which is converted to length using the OAP reference speed. As discussed, using PAS would result in particles flattened in the horizontal dimension since for particles in the OAP size range v_p is higher than PAS (Fig. 9). For the particles shown in Figure 12 pressure and temperature conditions recorded during the ~~passage~~ passages ensure droplets being in a liquid state. Image colors are the three levels of shadow recording on each photo-detector. The vertical scale is 62 pixels and pixels represent areas of 15 µm ~~while the horizontal axis represents the timeline~~. 15 µm. Images were taken using the TAS_{CAPS} as reference speed. TAS_{CAPS} is obtained as explained in section 3.1.4. ~~Most of the droplets show a spherical shape, whereas some larger droplets are deformed~~ The smaller droplet images are nearly circular, whereas larger droplets show deformed shapes, with the deformation ~~being more visible for the larger droplets~~becoming increasingly visible with increasing size. The red ~~contours highlight~~ contour highlights droplet breakup and the blue ones indicate large ~~and~~ deformed droplets that are not fully recorded by the array.

To better understand the droplet deformation and ~~the flow deviation from the free stream conditions we perform~~ v_p deviations from TAS we performed a statistical analysis of ~~the imagesshown in Fig. 12~~droplet images. Figure 13 compares the deformation ratio, defined as the ratio between main droplet axes d_y/d_x for the different droplet images. ~~Images are from a selected flight sequence where we encountered liquid droplets (black markers)~~To extend our analysis, we included datasets collected during different campaigns (as indicated by the marker colors). The image were taken during selected flight sequences where liquid droplets were encountered. Following Korolev (2007), we choose droplet images ~~only showing~~ showing only a small Fresnel effect and entirely contained in the field of view of the CIP, except for the ATom-4 data marked in light blue (Fig. 13b) where

the particles were not fully recorded. Image analyses were conducted using the image processing library OpenCV (Bradski, 2000) (using a contours threshold of 0.8). Error bars in both directions are calculated according to the CIP size resolution of one pixel, corresponding to 15 µm and solid lines indicate the mean value of each campaign. ~~To extend our analysis, we included two datasets collected during the ATom campaign. The first (red) was taken~~ Red markers refer to measurements during ATom-1 with the PAS_{CAPS} set as reference speed for particles. ~~For the second one (gray), recorded during~~ Dark blue markers refer to ATom-2 ~~, the TAS was estimated using the calibrated speed as shown in~~ when the TAS_{CAPS} was used after re-calibration of the pitot tube (Fig. 11b). In the case of ATom-1 (red markers), the use of the PAS ~~as an approximation of particle speed~~ causes a squeezing effect in the images along the flow direction~~(~~, i.e. $d_y/d_x > 1$ for most droplets~~)~~. Contrary, during ATom-2, ATom-4, and A-LIFE the ratio d_y/d_x is more evenly distributed around 1 ~~illustating~~ illustrating the benefit of using TAS_{CAPS} as reference speed. For small droplets (<150 µm) the large scattering is due to the limited instrument resolution (see error bars). For larger droplets error bars expressing the instrumental resolution cannot explain the data scattering~~, especially in case of the A-LIFE dataset~~. The scattering ~~cannot either be explained only by airspeed errors . One possible explanation can be~~ also cannot be explained by air speed errors only. A possible explanation is the instability effect on the surface of the droplets, as presented in Szakall et al. (2009), and discussed below. To better understand these phenomena ~~and estimate errors committed when using OAP images to approximate droplet volume,~~ we extend our ~~results~~ study by using a droplet deformation model.

3.2.1 Quantification of droplet deformation

Before analyzing the results of the droplet deformation model, we ~~want to~~ test the numerical results by comparison with data from the experimental work of Vargas (2012). ~~As a benchmark, we selected one of~~ We selected the experiments of Vargas (2012) where they observed a 1032 µm water droplet approaching an aircraft wing as test for our simulations. The selected experiment consisted ~~on a rotating arm,~~ of a droplet that is vertically falling on a horizontally rotating arm with an attached wing profile~~, rotating at~~ . The wing profile rotated with a speed of 90 ms^{-1}. In Figure 14 selected images at different ~~instants from~~ points of time in the Vargas (2012) experiment (upper ~~panels~~half of the upper panel) are compared with the corresponding simulation results (lower ~~panels~~half of the upper panel). Since the ~~imposed flow velocity~~ flow circulating around the particle is changing with time, the lower panel also shows the corresponding ~~speed values U_{rel}~~ slip velocity values U_{slip} defined as the droplet ~~relative speed with respect to the airflow~~speed relative to the suspending air. To have a more explicit comparison ~~,~~ of the change of droplet shape, the lower panel of Fig. 14 ~~b shows the length~~ shows the lengths of the droplet's axes of the experimental data (dots) and those simulated (lines) as a function of time and relative speed ~~U_{rel}. Principal~~ U_{slip}. The lengths of the axes of individual droplet images are determined using the length ~~of the side~~ and width of a circumscribing rectangle (as sketched in the Fig. 14). As visible in the upper panel, when the droplet approaches the airfoil ~~U_{rel}~~ U_{slip} increases and the droplet starts to be squeezed along the flow direction, until the breakup process occurs at the droplet edges for ~~$U_{rel} \sim$~~ $U_{slip} \sim$ 60 ms^{-1}. The model reproduces ~~qualitatively and quantitatively well, over time,~~ the behavior of the droplet ~~with only small deviations~~ over time qualitatively well with deviations smaller than two times the uncertainties of the experimental data. To extend our result to different droplet diameters and flight conditions, we use the Weber number We which represents the ratio

of the aerodynamic forces to the surface tension forces. We is defined as:

$$We = \frac{d\rho_{air}U_{rel}^2}{\sigma} \frac{d_p\rho_{air}U_{slip}^2}{\sigma}. \quad (8)$$

σ is the surface tension and ~~d~~ d_p the droplet diameter. In our case, ~~U_{rel}~~ U_{slip} is changing with time from zero when the droplet is in still air, to its maximum value when the droplet is recorded (~~U_{rel}~~ U_{slip} = TAS-PAS for large Stokes numbers). ~~The Weber number represents the ratio of the aerodynamic forces to the surface tension forces.~~

To understand the data deviation found in Fig. 13 we simulated different droplet diameters. The results are shown in Fig. 15 where the deformation ratio is plotted for the simulated droplets as a function of the ~~Weber number~~We. Different marker colors represent different test cases where we varied droplet diameters. As a droplet approaches the airfoil, the relative speed ~~U_{rel}~~ U_{slip} increases and therefore the ~~Weber number~~ We also increases. The mechanism of droplet deformation and breakup is governed by an interplay of aerodynamic, tension and viscous forces. The distortion is primarily caused by the aerodynamic forces, whereas the surface tension and viscous forces, respectively, resist and delay deformation of the droplet. Gravitational forces play a minor role since the ratio of aerodynamic forces over gravitational forces ~~$\rho_{air}U_{rel}^2/\rho_d g d$~~ $\rho_{air}U_{slip}^2/\rho_p g d_p$, is much larger than unity. When ~~inertial~~ aerodynamic forces grow larger than the surface tension forces, they deform the droplet causing in the worst case a breakup of the droplet by aerodynamic shattering (Craig et al., 2013). For a droplet approaching an airfoil, the viscous forces are smaller than aerodynamic and surface tension forces and the droplet breakup process is mainly controlled by ~~We~~We. Howarth (1963) and Prandtl (1952) showed that a droplet requires a critical Weber number (~~We_{crit}~~ We_{crit}) for breakup. Wierzba (1990) studied ~~the critical Weber numbers (Weber number at the time of droplet breakup)~~ We_{crit} when droplets interact with an instantaneous ~~airflow~~ air flow in a horizontal wind tunnel. Kennedy and Roberts (1990) studied the breakup of droplets subject to an accelerating flow in a vertical wind tunnel.

The critical ~~We for the breakup~~ Weber number We_{crit} from different experimental studies with uniform ~~airflow~~ air flow varies around 11 ± 2. Craig et al. (2013) also assumed ~~$We_{crit} = 12$~~ $We_{crit} = 12$ for determining the droplet critical diameter d_{crit} for aerodynamic shattering on an inlet. For a droplet approaching an airfoil, since ~~U_{rel} is changing~~ U_{slip} is changing and droplets can adjust their shape to the changing flow, droplet breakup occurs at larger ~~We compared with~~ We compared to the case of a uniform ~~airflow~~air flow (Vargas, 2012). On the other hand, the rapid change in the flow creates ~~instability~~ instabilities and droplets show a deformed shape already at ~~We~~$We \sim 1$ (see Fig. 15). Garcia-Magariño et al. (2018) characterized the ~~We_{crit}~~ We_{crit} providing an analytical equation:

$$We We_{crit} = 17.5 + 17.9\tau \text{ where } \tau = \frac{\sqrt{(\rho d^3\pi/(6\sigma))}}{U_{rel}/\frac{\partial U_{rel}}{\partial t}} \frac{\sqrt{(\rho_p d_p^3\pi/(6\sigma))}}{U_{slip}/\frac{\partial U_{slip}}{\partial t}} \quad (9)$$

Using the simulated ~~field and Eq. 9 with Eq. 8~~ air flow fields and Eqs. 8 and 9, we can express the critical diameter d_{crit} as a function of relative ~~speed U_{rel}. U_{rel}~~ particle speed U_{slip}. U_{slip} is a function of TAS and mounting position (see Fig. 5). Therefore, for a specific configuration, d_{crit} can be expressed as a function of TAS. Figure 16 shows how d_{crit} decreases when TAS increases. The two colors in Fig. 16 refer to the two different mounting configurations for the DLR Falcon and the NASA-DC-8. The ~~differences~~ difference in the mounting ~~system~~ configurations between the Falcon and the DC-8 ~~are responsible~~ is

the main reason for the differences in the relative ~~velocity~~particle speed U_{slip} for a given droplet diameter d_p and TAS, which results in differences in d_{crit} as shown in Fig. 16. Figure 16 also shows that pressure and temperature have only a rather small effect since results for different test cases with same TAS lie on top of each other. Generally, a large difference between the free stream and the probe ~~airspeed~~ air speed will increase the ~~relative velocity~~ slip velocity U_{slip} and consequently the Weber number, reducing the critical diameter for droplet breakup. This explains why critical diameters for the Falcon configuration are smaller than for the DC-8. ~~Small~~

In general, smaller droplets resist deformation more than larger ones because the small ~~radius~~ diameter translates into a larger curvature. However, when comparing equal ~~Weber numbers~~We, small droplets show instability phenomena where the droplet surface starts to oscillate (called Taylor instability). This effect can be responsible for ~~the~~ some scattering of data in Fig. 13. The deforming effect is only partially visible in the statistical analysis presented in Fig. ~~12~~13, since large particles have a higher chance to be only partially recorded inside the field of view, and consequently being excluded from the study. ~~As shown in Fig. 5, the relative velocity U_{rel} at the sampling area location is roughly 30 % of TAS. For example, for an airplane flying at 100 at 900 , recorded particles have a relative velocity of 30 . For a droplet of 200~~ When considering particles not fully recorded inside the field of view, the deformation is visible for particles larger than about 600 µm, ~~this corresponds to We=2.5 and consequently it cannot be considered being spherical~~as shown in Fig. 13b. Most have ratios $d_y/d_x > 1$ going up to 1.4 which is confirmed by the mean values (lines) being larger than unity. Since the y-extension of these particles is not fully covered by the imaging array, the real ratio d_y/d_x is probably even higher.

3.2.2 Impact of droplet deformation on particle volume estimation

As observed in Figs. 12, 14 and 15 large liquid droplets show a large distortion with d_y/d_x values around two and larger, when measured with an OAP onboard a fast aircraft. This raises the question ~~of~~ which diameter should be used to describe the size of deformed droplets. Different diameter definitions exist (Korolev et al., 1998). Here we use as approximation diameters d_{approx}, the maximum diameter $d_{max} = \max(d_x, d_y)$, the mean diameter $d_{mean} = (d_x + d_y)/2$, and the area equivalent diameter $d_{equi} = 2\sqrt{Area/\pi}$ where Area is the droplet cross section area calculated from the image. Two further approximation are used, $d_{spheroid} = (d_x d_y^2)^{1/3}$ derived assuming a spheroid rotated around the x-axis and $d_{asym} = (4/\pi \cdot Area \cdot d_y)^{1/3}$. McFarquhar (2004) noted that inconsistencies in particle size definitions could have significant impacts on mass conversion ratios between different hydrometeor classes used in numerical models. Errors in the droplet volume approximations have a direct effect on the ~~LWC estimation. Here, we~~ liquid water content (LWC) estimation. We use the numerical simulations analyzed in Fig. 15 to better understand possible errors in the estimation of the droplet volume. The simulated droplet shapes are processed to calculate the chosen different approximation diameters and estimate the corresponding approximation volumes ($V_{approx} = d_{approx}^3 \cdot \pi/6$). Results are shown in Fig. 17, where the relative error ($~~err_{rel} = |V_{approx} - V_0|/V_0~~ err_{slip} = |V_{approx} - V_0|/V_0$) is plotted as a function of ~~We~~We. V_0 is the ~~initial~~ actual droplet volume. Using the d_{max} (red diamonds) error increases progressively with ~~We~~We, from 10 % at ~~We~~We=1 until almost a factor 10 when the breakup process starts. A better approximation ~~,~~ ~~reducing this effect, is to use~~ is the mean diameter d_{mean} (cyan symbols). In this case, for ~~We~~We<20, on average the volume is underestimated by 2 % to 20 %. For larger ~~We~~We, the formula overestimates the volume up to a factor of 6. A more stable way

to define droplet diameter is based on the equivalent d_{equi} (green circles). Also in this case, errors are growing as a function of ~~We~~We, passing from 3 % to 40 %. A common assumption is considering droplets as spheroids (purple triangles). In this case using the approximation formula for a spheroid $V_{approx} = \pi/6 d_x \cdot d_y^2$ gives errors smaller than 12 % below ~~We~~We=34. For larger ~~We~~We, droplets appear asymmetric, and errors can grow larger than a factor of 7. The best approximation is obtained by using d_{asym} where the volume result in the more general formula $V_{approx} = 2/3 Area \cdot d_y$. Errors, in this case, are generally $\pm 3\%$ to $\pm 10\%$ and in case of droplet ~~break up~~ breakup still smaller than a factor of 2.

4 Recommendations

The following list summarizes the proposed correction strategy to reduce flow-induced measurement errors and to express measurement uncertainties for OAP and OPC instruments. OPC and OAP measurement errors directly depend on flow conditions like pressure, ~~airspeed~~air speed, and temperature. Since free stream conditions differ from conditions at the position where the instrument is mounted on the aircraft, it is fundamental to adopt a correction scheme.

Recommended steps for ~~OAP:~~ optical array probes (OAP) such as CIP:

1. For imaging probes, covering ~~a size range~~ particle diameters larger than 50 µm, use the TAS as the reference ~~particle speed for calculating the shutter speed~~speed in the OAP data acquisition software. If possible, use the TAS recorded by the ~~plane~~aircraft. Otherwise, an option could be to re-calibrate the pitot tube installed on the probe to measure free stream conditions (~~see Sec~~PAS, $p_{s,probe}$ and T_{probe}, see Sect. 3.1.4 and the appendix). In this last case, the local probe conditions can be obtained during the data evaluation by inverting the calibration coefficients for p_s, q_c and using Eq. 3 to calculate the PAS.

2. ~~For approximating the droplet volume using OAP images, use the formula $V = 2 Area \cdot d_y/3$. Indeed, droplets appear to be~~ Droplets are deformed by the flow distortion around the wing-mounted instrument even at low ~~airspeed.~~

3. ~~Try to find instrument mounting locations where the deviation between the instrument and free stream conditions are small. Substantial velocity differences will lead to deformations of droplets with the risk of aerodynamic shattering, and consequently increasing the number concentrations. See Fig. 16 for a quick-view of critical breakup diameters depending on aircraft speed.~~ TAS which complicates the volume estimation from OAP images. For the volume estimation using the formula $V = 2 \cdot Area \cdot d_y/3$ is recommended.

Recommended steps for ~~OPC:~~ passive inlet optical particle counters (OPC) such as CAS:

1. ~~As a first step calculate~~ Calculate the α parameter (Eq. 5) using the ratio between the free stream and probe ~~flight conditions.~~ conditions. To do so data from the instrument's pitot tube recording local air flow conditions (PAS, $p_{s,probe}$ and T_{probe}) at the probe are necessary in addition to independent meteorological data covering the free stream condition.

2. ~~Second, estimate~~ Estimate the particle Stokes number Stk^* based on flight conditions (~~p,~~ p_s, (U=)TAS), particle diameter and density (Eq. 4). If particle density is not known, use a range of possible values to propagate the uncertainty.

3. Use ~~the~~ Eq. 6 ~~function of α and Stk~~ to calculate the correction factor ~~. This parameter depends on flight conditions and particle diameter~~ f_{eff} as function of α and Stk^*.

4. ~~Use~~ For the derivation of particle number concentration use free stream conditions (TAS) ~~to calculate particle concentrations. This is especially important for coarse mode aerosols.~~

5. ~~Divide the obtained concentrations by the correction factors~~and the correction factor f_{eff} (see Eq. 7).

6. ~~The first steps can be skipped using~~ If steps 1-3 can not be done, the lookup table ~~that can be found~~ in the appendix (Tab. A3) can be used instead. These correction values were calculated for different diameters and two reference densities (water and mineral dust).

When designing new mounting systems, the mounting location should be selected such that the deviation between the instrument and free stream conditions, and thus also the flow-induced measurement errors, are minimized.

5 Conclusions

This study investigated the effect of flow distortion around wing-mounted instruments. The analysis focused on open path and passive inlet OPC and OAP instruments. The data-set collected during SALTRACE (Weinzierl et al., 2017) was used to estimate flow differences between the free stream and the aerosol and cloud probes mounted under an aircraft wing. The ~~airspeed~~ air speed at the probe location (PAS) was on average 30 % smaller than ~~at free stream conditions~~ in the free stream (TAS).
A CFD model was adopted to test different flight conditions. The numerical results matched the recorded ~~difference~~ differences between free stream conditions and the conditions at the probe location (see Fig. 6). The simulated flow ~~field was~~ fields were used to estimate changes in concentration for particles of different ~~density~~ densities and diameters. Concentrations of particles smaller than ~~0.5~~ about 5 µm ~~were correctly estimated when using~~ can be derived with low error using the probe conditions (PAS, $p_{s,probe}$ and T_{probe}). Therefore, it is highly beneficial to equip wing-mounted instruments covering this size range with measurements of the probe conditions (PAS, $p_{s,probe}$ and T_{probe}). However, ~~simulations~~ the simulations also showed that using probe conditions ~~such as PAS, p_{probe} and T_{probe} led~~ leads to incorrect particle ~~concentration~~ concentrations with an overestimation of the coarse mode aerosol amount ~~of up to 20 % especially in the~~ in the diameter range $[5 - 100]$ µm of up to 20 % (see Fig. 10). ~~We proposed a correction factor for the particle concentration based on the particle Stokes number . This correction~~ This inaccuracy can be corrected with the correction scheme proposed in this study which considers the Stokes number depending on particle size and density. The proposed correction scheme was generalized to different aircraft configurations with a simple formula based on the ratio between the probe and free stream conditions (Eq. 6), reducing concentration errors drastically, from 30 % to ~~smaller~~ less than 2 %.
Wrong OAP recording speeds not only impact the derived particle concentrations, but also result in deformed images. ~~The~~

deviation of the airspeed recorded by the under-wing instrument from the free stream airspeed was significantly reduced Since coarse particles and droplets ($d_p > 50$ µm) move with a speed $v_p \approx$ TAS, TAS was used as the reference speed in the OAP data acquisition software during the A-LIFE and ATom-2 missions. In our measurements during these missions, the OAP reference speed was taken from the instrument's pitot tube measurements after a re-calibration of the instrument's pitot tube . The re-calibrated speed was used as a reference for the CIP during the A-LIFE and Atom-2 missionssuch that it provides TAS. Although the use of TAS as a reference particle speed largely reduced images distortions, large droplets still appeared deformed. To understand the deformation of water droplets, a VOF model was used volume of fluid (VOF) method was used which confirmed that aerodynamic forces are the reason for the deformations. The model well reproduced experimental data from Vargas (2012). Already at WeWeber number We=1 droplets appeared were deformed (see Figs. 14 and 15). In particular droplets smaller than 400 µm showed a wiggling behavior. Oscillations of the droplets were caused by Taylor deformed shapes caused by instabilities developing at the their surface.

To reduce errors of the estimated LWC , derived from OAP size distributions, different definitions of droplet diameter were tested. Using the maximum droplet dimension d_{max} to estimate droplet volume resulted in a 40 % error even at low aircraft speed with errors dramatically increasing, up to one order of magnitude, with aircraft speed. The best volume approximation was obtained by using the formula $V = 2d_y \cdot Area/3$, where d_y is the particle diameter perpendicular to the flow and $Area$ is the droplet area calculated from the image. Significant differences between airspeed at air speed in the free stream (TAS) and at the instrument location (PAS) increased the risk, especially for fast flying aircraft, of the breakup of large droplets. Droplet breakup caused measurement artifacts by increasing the number of particles (red contours contour in Fig. 12). This phenomenon, known also as aerodynamic breakup (Craig et al., 2013), caused shattering of droplets without hiting hitting instrument walls. Extending the result from Garcia-Magariño et al. (2018), we provided an estimate for the critical diameter of droplet breakup as a function of aircraft speed.

Numerical simulations explained the physical reason Deviations between values of PAS and TAS have been under discussion for some time. In this study, the physical reasons for the observed deviations between TAS and PAS and provided a correction methodwere explained based on numerical simulations and a new correction method has been proposed. The correction scheme was validated for the DLR Falcon (A-LIFE campaign) and the NASA DC-8 (ATom campaign) and the general conclusions hold for any fast-flying research aircraft. Using this new method for the analysis of past and upcoming data sets therefore may reduce errors in particle and droplet number concentrations up to 30 % and in the derived LWC up to one order of magnitude.

References

Albrecht, B. A.: Aerosols, Cloud Microphysics, and Fractional Cloudiness, Science, 245, 1227–1230, https://doi.org/10.1126/science.245.4923.1227, 1989.

Barlow, J., Rae, W., and Pope, A.: Wind Tunnel Testing 3rd edition, John Wiley & Sons, Inc., 1999.

Barsotti, S., Bignami, C., Buongiorno, M., Corradini, S., Doumaz, F., Guerrieri, L., Merucci, L., Musacchio, M., Nannipieri, L., Neri, A., Piscini, A., Silvestri, M., Spanu, A., Spinetti, C., Stramondo, S., and Wegmuller, U.: SAFER Response to Eyjafjallajökull and Merapi Volcanic Eruptions, In: 'Let's embrace space' Space Research achievements under the 7th Framework Programme, https://doi.org/10.2769/1549, http://hdl.handle.net/2122/7646, 2011.

Baumgardner, D., Jonsson, H., Dawson, W., O'Connor, D., and Newton, R.: The cloud, aerosol and precipitation spectrometer: a new instrument for cloud investigations, Atmospheric Research, 59, 251–264, https://doi.org/10.1016/S0169-8095(01)00119-3, 13th International Conference on Clouds and Precipitation, 2001.

Baumgardner, D., Newton, R., Krämer, M., Meyer, J., Beyer, A., Wendisch, M., and Vochezer, P.: The Cloud Particle Spectrom-eter with Polarization Detection (CPSPD): A next generation open-path cloud probe for distinguishing liquid cloud droplets from ice crystals, Atmos. Res., 142, 2–14, https://doi.org/10.1016/j.atmosres.2013.12.010, 2014.

Belyaev, S. and Levin, L.: Techniques for collection of representative aerosol samples, Journal of Aerosol Science, 5, 325 – 338, https://doi.org/https://doi.org/10.1016/0021-8502(74)90130-X, 1974.

Bogel, W. and Baumann, R.: Test and calibration of the DLR Falcon wind measuring system by maneuvers, J. Atmos.Oceanic Technol., 8, 5–18, https://doi.org/10.1175/1520-0426(1991)008<0005:TACOTD>2.0.CO;2, 1991.

Bradski, G.: The OpenCV Library, Dr. Dobb's Journal of Software Tools, 2000.

Chan, K. R., Dean-Day, J., Bowen, S. W., and Bui, T. P.: Turbulence measurements by the DC-8 meteorological measurement system, Geophys. Res. Lett., 25, 1355–1358, https://doi.org/10.1029/97GL03590, 1998.

Clark, M. M.: Drop breakup in a turbulent flow—I. Conceptual and modeling considerations, Chemical Engineering Science, 43, 671–679, https://doi.org/110.1016/0009-2509(88)87025-8, 1988.

Clift, R., Grace, J. R., and Weber, M. E.: Bubbles, Drops, and Particles, Academic Press, 1978.

Craig, L., Moharreri, A., Schanot, A., Rogers, D. C., Anderson, B., and Dhaniyala, S.: Characterizations of Cloud Droplet Shatter Artifacts in Two Airborne Aerosol Inlets, Aerosol Science and Technology, 47, 662–671, https://doi.org/10.1080/02786826.2013.780648, 2013.

Craig, L., Moharreri, A., Rogers, D. C., Anderson, B., and Dhaniyala, S.: Aircraft-Based Aerosol Sampling in Clouds: Performance Characterization of Flow-Restriction Aerosol Inlets, Journal of Atmospheric and Oceanic Technology, 31, 2512–2521, https://doi.org/10.1175/JTECH-D-14-00022.1, 2014.

Cruette, D., Marillier, A., Dufresne, J. L., Grandpeix, J. Y., Nacass, P., and Bellec, H.: Fast Temperature and True Airspeed Measurements with the Airborne Ultrasonic Anemometer–Thermometer (AUSAT), Journal of Atmospheric and Oceanic Technology, 17, 1020–1039, https://doi.org/10.1175/1520-0426(2000)017<1020:FTATAM>2.0.CO;2, 2000.

DeMott, P. J., Prenni, A. J., Liu, X., Kreidenweis, S. M., Petters, M. D., Twohy, C. H., Richardson, M. S., Eidhammer, T., and Rogers, D. C.: Predicting global atmospheric ice nuclei distributions and their impacts on climate, Proc. Natl. Acad. Sci. U.S.A., 107, 11 217–11 222, https://doi.org/10.1073/pnas.0910818107, 2010.

Drummond, A. M. and MacPherson, J. I.: Aircraft Flow Effects on Cloud Drop Images and Concentrations Measured by the NAE Twin Otter, J. Atmos. Ocean. Tech., 2, 633–643, https://doi.org/10.1175/1520-0426(1985)002<0633:AFEOCD>2.0.CO;2, 1985.

Elgobashi: Particle-Laden Turbulent Flows: Direct Numerical Simulation and Closure Models, Appl. Sci. Res., pp. 3–4, https://doi.org/10.1007/BF02008202., 1991.

Garcia-Magariño, A., SorSuthyvann, S., and Velazquez, S.: Droplet Breakup Criterion in Airfoils Leading Edge Vicinity, Journal of Aircraft, https://doi.org/10.2514/1.C034631, 2018.

Garcy, W.: Measurement of aircraft speed and altitude, NASA, Reference Publication 1046, https://ntrs.nasa.gov/search.jsp?R=19800015804, 1980.

Hayman, M., McMenamin, K. J., and Jensen, J. B.: Response Time Characteristics of the Fast-2D Optical Array Probe Detector Board, Journal of Atmospheric and Oceanic Technology, 33, 2569–2583, https://doi.org/10.1175/JTECH-D-16-0062.1, 2016.

Hinds, W. C.: Aerosol technology: properties, behavior, and measurement of airborne particles, John Wiley & Sons, 1999.

Howarth, L.: The Scientific Papers of G. I. Taylor. Vol. III. Aerodynamics and the Mechanics of Projectiles and Explosions, Journal of Fluid Mechanics, 17, 633–636, https://doi.org/10.1017/S0022112063241554, 1963.

Hsiang, L.-P. and Faeth, G.: Near-limit drop deformation and secondary breakup, International Journal of Multiphase Flow, 18, 635–652, https://doi.org/10.1016/0301-9322(92)90036-G, 1992.

Ibrahim, E. A., Yang, H. Q., and Przekwas, A. J.: Modeling of spray droplets deformation and breakup, Journal of Propulsion and Power, 9, 651–654, https://doi.org/10.2514/3.23672, 1993.

Israel, R. and Rosner, D. E.: Use of a Generalized Stokes Number to Determine the Aerodynamic Capture Efficiency of Non-Stokesian Particles from a Compressible Gas Flow, Aerosol Science and Technology, 2 (1), 45–51, https://doi.org/10.1080/02786828308958612, 1982.

Johnson, C.: Streamline diffusion finite-element method for compressible and incompressible fluid flow, in: Finite Elements in Fluids. Vol. 8, edited by Chung, T. J., vol. 8, pp. 75–96, 1992.

Jung, S., Tiwari, M. K., Doan, N. V., and Poulikakos, D.: Mechanism of supercooled droplet freezing on surfaces, Nature Communications, 3, 615 EP –, https://doi.org/10.1038/ncomms1630, article, 2012.

Kalogiros, J. A. and Wang, Q.: Aerodynamic Effects on Wind Turbulence Measurements with Research Aircraft, Journal of Atmospheric and Oceanic Technology, 19, 1567–1576, https://doi.org/10.1175/1520-0426(2002)019<1567:AEOWTM>2.0.CO;2, 2002.

Kandler, K., Schütz, L., Deutscher, C., Ebert, M., Hofmann, H., Jäckel, S., Jaenicke, R., Knippertz, P., Lieke, K., Massling, A., Petzold, A., Schladitz, A., Weinzierl, B., Wiedensohler, A., Zorn, S., and Weinbruch, S.: Size distribution, mass concentration, chemical and mineralogical composition and derived optical parameters of the boundary layer aerosol at Tinfou, Morocco, during SAMUM 2006, Tellus B, 61, 32–50, https://doi.org/10.1111/j.1600-0889.2008.00385.x, 2009.

Kennedy, J. and Roberts, J.: Rain Ingestion in a Gas Turbine Engine, in: ILASS-Americas, Inst. of Liquid Atomization and Spray Systems, 4th Annual Conference, pp. 154–186, 1990.

King, W. D.: Air Flow and Particle Trajectories around Aircraft Fuselages. I: Theory, J. Atmos. Ocean. Tech., 1, 5–13, https://doi.org/10.1175/1520-0426(1984)001<0005:AFAPTA>2.0.CO;2, 1984.

King, W. D., Turvey, D., Williams, D., and Llewellyn, D.: Air flow and particle trajectories around aircraft fuselages. II: Measurements., J. Atmos. Oceanic Tech., 1, 14–21, https://doi.org/10.1175/1520-0426(1984)001<0014:AFAPTA>2.0.CO;2, 1984.

Knollenberg, R.: Techniques for probing cloud microstructure, in: Clouds their Formation, Optical Properties, and Effects, pp. 15–91, Elsevier, https://doi.org/10.1016/b978-0-12-350720-4.50007-7, 1981.

Knollenberg, R. G.: The Optical Array: An Alternative to Scattering or Extinction for Airborne Particle Size Determination, Journal of Applied Meteorology, 9(1), 86–103, https://doi.org/10.1175/1520-0450(1970)009<0086:TOAAAT>2.0.CO;2, 1970.

Knollenberg, R. G.: Three new instruments for cloud physics measurements: the 2-D spectrometer probe, the forward scattering spectrometer probe and the active scattering aerosol spectrometer, Amer. Met. Society, pp. 554–561, int'l Conf. on Cloud Physics, 1976.

Kok, J. F., Ridley, D. A., Zhou, Q., Miller, R. L., Zhao, C., Heald, C. L., Ward, D. S., Albani, S., and Haustein, K.: Smaller desert dust cooling effect estimated from analysis of dust size and abundance, Nature Geoscience, 10, 274, https://doi.org/10.1038/ngeo2912, 2017.

Korolev, A.: Reconstruction of the Sizes of Spherical Particles from Their Shadow Images. Part I: Theoretical Considerations, J. Atmos. Ocean. Tech., 24, 376–389, https://doi.org/10.1175/JTECH1980.1, 2007.

Korolev, A. and Isaac, G.: Shattering During Sampling by OAPs and HVPS. Part I: Snow Particles, J. Atmos. Oceanic Technol., 22, 528–542, https://doi.org/10.1175/JTECH1720.1, 2005.

Korolev, A., Emery, E., and Creelman, K.: Modification and Tests of Particle Probe Tips to Mitigate Effects of Ice Shattering, Journal of Atmospheric and Oceanic Technology, 30, 690–708, https://doi.org/10.1175/JTECH-D-12-00142.1, 2013.

Korolev, A. V., Strapp, J. W., and Isaac, G. A.: Evaluation of the Accuracy of PMS Optical Array Probes, Journal of Atmospheric and Oceanic Technology, 15, 708–720, https://doi.org/10.1175/1520-0426(1998)015<0708:EOTAOP>2.0.CO;2, 1998.

Lance, S., Brock, C. A., Rogers, D., and Gordon, J. A.: Water droplet calibration of the Cloud Droplet Probe (CDP) and in-flight performance in liquid, ice and mixed-phase clouds during ARCPAC, Atmospheric Measurement Techniques, 3, 1683–1706, https://doi.org/10.5194/amt-3-1683-2010, 2010.

Laucks, M. and Twohy, C. H.: Size-Dependent Collection Efficiency of an Airborne Counter floow Virtual Impactor, Aerosol Sci. Thechnol, 28, 40–60, https://doi.org/10.1080/02786829808965511, 1998.

Launder, B. and Spalding, D.: The numerical computation of turbulent flows, Computer Methods in Applied Mechanics and Engineering, 3, 269–289, https://doi.org/10.1016/0045-7825(74)90029-2, 1974.

Lawson, R. P., O'Connor, D., Zmarzly, P., Weaver, K., Baker, B., Mo, Q., and Jonsson, H.: The 2D-S (Stereo) Probe: Design and Preliminary Tests of a New Airborne, High-Speed, High-Resolution Particle Imaging Probe, Journal of Atmospheric and Oceanic Technology, 23, 1462–1477, https://doi.org/10.1175/JTECH1927.1, 2006.

Letko, W.: Investigation of the fuselage interference on a pitot-static tube extending forward from the nose of the fuselage, NACA Technical Note NACA-TN-1496, https://ntrs.nasa.gov/search.jsp?R=19930082152, 1947.

Marks, C. R.: Drop Breakup and Deformation in Sudden Onset Strong Flow, American Institute of Chemical Engineers, http://adsabs.harvard.edu/abs/1998PhDT.....204M, 1998.

Masud, J.: Performance Characteristics of Flush Angle-of-Attack Measurement System Integrated on a Pitot Tube, Engineering Applications of Computational Fluid Mechanics, 4:4, 549–557, https://doi.org/10.1080/19942060.2010.11015340, 2010.

McFarquhar, G. M.: A New Representation of Collision-Induced Breakup of Raindrops and Its Implications for the Shapes of Raindrop Size Distributions, Journal of the Atmospheric Sciences, 61, 777–794, https://doi.org/10.1175/1520-0469, 2004.

Moharreri, A., Craig, L., Rogers, D. C., and Dhaniyala, S.: A New Aircraft Inlet for Sampling Interstitial Aerosol: Design Methodology, Modeling, and Wind Tunnel Tests, Aerosol Science and Technology, 47, 885–894, https://doi.org/10.1080/02786826.2013.800186, 2013.

Moharreri, A., Craig, L., Dubey, P., Rogers, D. C., and Dhaniyala, S.: Aircraft testing of the new Blunt-body Aerosol Sampler (BASE), Atmospheric Measurement Techniques Discussions, 7, 2663–2688, https://doi.org/10.5194/amtd-7-2663-2014, 2014.

Montorfano, A.: Mesh generation for HPC problems: the potential of SnappyHexMesh, https://doi.org/10.13140/RG.2.2.25007.53923, 2017.

Nacass, P.: Theoretical Errors on Airborne Measurements Of Static Pressure, Impact Temperature, air Flow Angle, Air Flow Speed, NCAR Technical Note, NCAR/TN-385+STR, https://doi.org/10.5065/D6M61H79, 1992.

Nakao, S., Kashitani, M., Miyaguni, T., and Yamaguchi, Y.: A study on high subsonic airfoil flows in relatively high Reynolds number by using OpenFOAM, Journal of Thermal Science, 23, 133–137, https://doi.org/10.1007/s11630-014-0687-5, 2014.

Nayar, K. G., Panchanathan, D., McKinley, G. H., and Lienhard, J. H.: Surface Tension of Seawater, Journal of Physical and Chemical Reference Data, 43, 043 103, https://doi.org/10.1063/1.4899037, 2014.

Noh, W. F. and Woodward, P.: SLIC (Simple Line Interface Calculation), in: Proceedings of the Fifth International Conference on Numerical Methods in Fluid Dynamics June 28 – July 2, 1976 Twente University, Enschede, edited by van de Vooren, A. I. and Zandbergen, P. J., pp. 330–340, Springer Berlin Heidelberg, Berlin, Heidelberg, 1976.

Norment, H. G.: Three-Dimensional Trajectory Analysis of Two Drop Sizing instruments: PMS* OAP and PMS* FSSP, Journal of Atmospheric and Oceanic Technology, 5, 743–756, https://doi.org/10.1175/1520-0426(1988)005<0743:TDTAOT>2.0.CO;2, 1988.

O'Rourke, P. J. and Amsden, A. A.: The Tab Method for Numerical Calculation of Spray Droplet Breakup, in: SAE Technical Paper, SAE International, https://doi.org/10.4271/872089, 1987.

Pilch, M. and Erdman, C. A.: Use of Breakup Time Data and Velocity History Data to Predict the Maximum Size of Stable Fragments for Acceleration-Induced Breakup of a Liquid Drop, Int. J. Multiphase Flow, 13, 41–757, https://doi.org/10.1016/0301-9322(87)90063-2, 1987.

Poret, M., Corradini, S., Merucci, L., Costa, A., Andronico, D., Montopoli, M., Vulpiani, G., and Freret-Lorgeril, V.: Reconstructing volcanic plume evolution integrating satellite and ground-based data: application to the 23 November 2013 Etna eruption, Atmospheric Chemistry and Physics, 18, 4695–4714, 2018.

Prandtl, L.: Prandtl's Essentials of Fluid Mechanics, vol. 158 of *Applied Mathematical Sciences*, Springer-Verlag New York, https://doi.org/10.1007/b97538, 1952.

Pruppacher, H. and Klett, J.: Microphysics of Clouds and Precipitation, vol. 18 of *Atmospheric and Oceanographic Sciences Library*, Springer Netherlands, https://doi.org/10.1007/978-0-306-48100-0, 2010.

Rallison, J.: The deformation of small viscous drops and bubbles in shear flows., Ann. Rev. Fluid Mech., 16, 45–66, https://doi.org/10.1146/annurev.fl.16.010184.000401, 1984.

Rhie, C. and Chow, W.: A numerical study of the turbulent flow past an isolated airfoil with trailing edge separation, in: AIAA/ASME 3rd Joint Thermophysics, Fluids, Plasma and Heat Transfer Conference, AIAA-82-0998, 1982.

Rosenfeld, D. and Lensky, I. M.: Satellite–Based Insights into Precipitation Formation Processes in Continental and Maritime Convective Clouds, Bulletin of the American Meteorological Society, 79, 2457–2476, https://doi.org/10.1175/1520-0477(1998)079<2457:SBIIPF>2.0.CO;2, 1998.

Rumscheidt, F. D. and Mason., S. G.: Particle motions in sheared suspensions XII. Deformation and burst of fluid drops in shear and hyperbolic flow., J. Colloid Sci., 16, 238–261, https://doi.org/10.1016/0095-8522(61)90003-4, 1961.

Scott, S., Bui, T. P., Chan, R., and Bowen, S. W.: The Meteorological Measurement System on the NASA ER-2 Aircraft, J. Atmos. Oceanic Technol., 7, 525–540, https://doi.org/10.1175/1520-0426(1990)007<0525:TMMSOT>2.0.CO;2, 1990.

Silverman, B.: Density Estimation for Statistics and Data Analysis, vol. 26 of *Monographs on Statistics and Applied Probability*, Chapman and Hall,London, 1986.

Solomos, S., Ansmann, A., Mamouri, R.-E., Binietoglou, I., Patlakas, P., Marinou, E., and Amiridis, V.: Remote sensing and modelling analysis of the extreme dust storm hitting the Middle East and eastern Mediterranean in September 2015, Atmospheric Chemistry and Physics, 17, 4063–4079, https://doi.org/10.5194/acp-17-4063-2017, 2017.

Spanu, A., Dollner, M., Gasteiger, J., Bui, T., and Weinzierl, B.: Probe comparison, https://doi.org/10.3334/ornldaac/??, https://daac.ornl.gov/cgi-bin/dsviewer.pl?ds_id=??, 2018.

Stocker, T., Qin, D., Plattner, G. K., Tignor, M., Allen, S., Boschung, J., Nauels, A., Xia, Y., Bex, V., and Midgley, P.: Climate Change 2013 – The Physical Science Basis: Working Group I Contribution to the Fifth Assessment Report of the Intergovernmental Panel on Climate Change, Cambridge University Press, https://doi.org/10.1017/CBO9781107415324, 2014.

Sun, Z., Zhou, J., Zhang, H., and J.A., H.: On the influencing factors in a Pitot tube measurement II. Influence of total and static ports, Chinese Journal of Sensors and Actuators, 20, 941–944, 2007.

Szakall, M., Diehl, K., Mitra, S. K., and Borrmann, S.: A Wind Tunnel Study on the Shape, Oscillation, and Internal Circulation of Large Raindrops with Sizes between 2.5 and 7.5 mm, Journal of the Atmospheric Sciences, 66, 755–765, https://doi.org/10.1175/2008JAS2777.1, 2009.

Tan, S. and Papadakis, M.: General Effects of Large Droplet Dynamics on Ice Accretion Modeling, Aerospace Sciences Meetings, American Institute of Aeronautics and Astronautics, https://doi.org/10.2514/6.2003-392, 0, 2003.

Vargaftik, N., Volko, B., and Voljak, L.: International Tables of the Surface Tension of Water, Journal of Physical and Chemical, 12, 817, https://doi.org/10.1063/1.555688, 1983.

Vargas, M.: Droplet Deformation Prediction With the Droplet Deformation and Breakup Model (DDB), https://doi.org/10.2514/6.2012-3131, atmospheric Space Environments Conference, 2012.

Vargas, M. and Feo, A.: Experimental Observations on the Deformation and Breakup of Water Droplets Near the Leading Edge of an Airfoil, https://doi.org/10.2514/6.2010-7670, 2010.

Walser, A., Sauer, D., Spanu, A., Gasteiger, J., and Weinzierl, B.: On the parametrization of optical particle counter response including instrument-induced broadening of size spectra and a self-consistent evaluation of calibration measurements, Atmospheric Measurement Techniques Discussions, 2017, 1–30, https://doi.org/10.5194/amt-10-4341-2017, 2017.

Weber, R. J., Clarke, A. D., Litchy, M., Li, J., Kok, G., Schillawski, R. D., and McMurry, P. H.: Spurious Aerosol Measurements when Sampling from Aircraft in the Vicinity of Clouds., J. Geophys. Res., 103, 28 337–28 346, https://doi.org/10.1029/98JD02086, 1998.

Weigel, R., Spichtinger, P., Mahnke, C., Klingebiel, M., Afchine, A., Petzold, A., Krämer, M., Costa, A., Molleker, S., Reutter, P., Szakáll, M., Port, M., Grulich, L., Jurkat, T., Minikin, A., and Borrmann, S.: Thermodynamic correction of particle concentrations measured by underwing probes on fast-flying aircraft, Atmospheric Measurement Techniques, 9, 5135–5162, https://doi.org/10.5194/amt-9-5135-2016, 2016.

Weinzierl, B. and ALIFE_Team: Absorbing aerosol layers in a changing climate: aging, lifetime and dynamics (A-LIFE), www.a-life.at, 2018.

Weinzierl, B., Petzold, A., Esselborn, M., Wirth, M., Rasp, K., Kandler, K., SchüTZ, L., Koepke, P., and Fiebig, M.: Airborne measurements of dust layer properties, particle size distribution and mixing state of Saharan dust during SAMUM 2006, Tellus B: Chemical and Physical Meteorology, 61, 96–117, https://doi.org/10.1111/j1600-0889.2008.00392.x, 2009.

Weinzierl, B., Sauer, D., Esselborn, M., Petzold, A., Veira, A., Rose, M., Mund, S., Wirth, M., Ansmann, A., Tesche, M., Gross, S., and Freudenthaler, V.: Microphysical and optical properties of dust and tropical biomass burning aerosol layers in the Cape Verde region—an overview of the airborne in situ and lidar measurements during SAMUM-2, Tellus B, 63, 589–618, https://doi.org/10.1111/j.1600-0889.2011.00566.x, 2011.

Weinzierl, B., Ansmann, A., Prospero, J. M., Althausen, D., Benker, N., Chouza, F., Dollner, M., Farrell, D., Fomba, W. K., Freudenthaler, V., Gasteiger, J., Groß, S., Haarig, M., Heinold, B., Kandler, K., Kristensen, T. B., Mayol-Bracero, O. L., Müller, T., Reitebuch, O.,

Sauer, D., Schäfler, A., Schepanski, K., Spanu, A., Tegen, I., Toledano, C., and Walser, A.: The Saharan Aerosol Long-range Transport and Aerosol-Cloud-Interaction Experiment (SALTRACE): overview and selected highlights, Bulletin of the American Meteorological Society, 98, 1427–1451, https://doi.org/10.1175/BAMS-D-15-00142.1, 2017.

Weller, H., Tabor, G., Jasak, H., and Fureby, C.: A tensorial approach to computational continuum mechanics using object-oriented techniques, Computers in Physics, 12, https://doi.org/10.1063/1.168744, 1998.

Wierzba, A.: Deformation and breakup of liquid drops in a gas stream at nearly critical Weber numbers, Experiments in Fluids, 9, 59–64, https://doi.org/10.1007/BF00575336, 1990.

Wofsy, S., Afshar, S., Allen, H., Apel, E., Asher, E., Barletta, B., Bent, J., Bian, H., Biggs, B., Blake, D., Blake, N., Bourgeois, I., Brock, C., Brune, W., Budney, J., Bui, T., Butler, A., Campuzano-Jost, P., Chang, C., Chin, M., Commane, R., Correa, G., Crounse, J., Cullis, P., Daube, B., Day, D., Dean-Day, J., Dibb, J., Digangi, J., Diskin, G., Dollner, M., Elkins, J., Erdesz, F., Fiore, A., Flynn, C., Froyd, K., Gesler, D., Hall, S., Hanisco, T., Hannun, R., Hills, A., Hintsa, E., Hoffman, A., Hornbrook, R., Huey, L., Hughes, S., Jimenez, J., Johnson, B., Katich, J., Keeling, R., Kim, M., Kupc, A., Lait, L., Lamarque, J.-F., Liu, J., Mckain, K., Mclaughlin, R., Meinardi, S., Miller, D., Montzka, S., Moore, F., Morgan, E., Murphy, D., Murray, L., Nault, B., Neuman, J., Newman, P., Nicely, J., Pan, X., Paplawsky, W., Peischl, J., Prather, M., Price, D., Ray, E., Reeves, J., Richardson, M., Rollins, A., Rosenlof, K., Ryerson, T., Scheuer, E., Schill, G., Schroder, J., Schwarz, J., St.Clair, J., Steenrod, S., Stephens, B., Strode, S., Sweeney, C., Tanner, D., Teng, A., Thames, A., Thompson, C., Ullmann, K., Veres, P., Vizenor, N., Wagner, N., Watt, A., Weber, R., Weinzierl, B., Wennberg, P., Williamson, C., Wilson, J., Wolfe, G., Woods, C., and Zeng, L.: ATom: Merged Atmospheric Chemistry, Trace Gases, and Aerosols, https://doi.org/10.3334/ornldaac/1581, https://daac.ornl.gov/cgi-bin/dsviewer.pl?ds_id=1581, 2018.

Yang, W., Jia, M., Che, Z., Sun, K., and Wang, T.: Transitions of deformation to bag breakup and bag to bag-stamen breakup for droplets subjected to a continuous gas flow, International Journal of Heat and Mass Transfer, 111, 884–894, https://doi.org/10.1016/j.ijheatmasstransfer.2017.04.012, 2017.

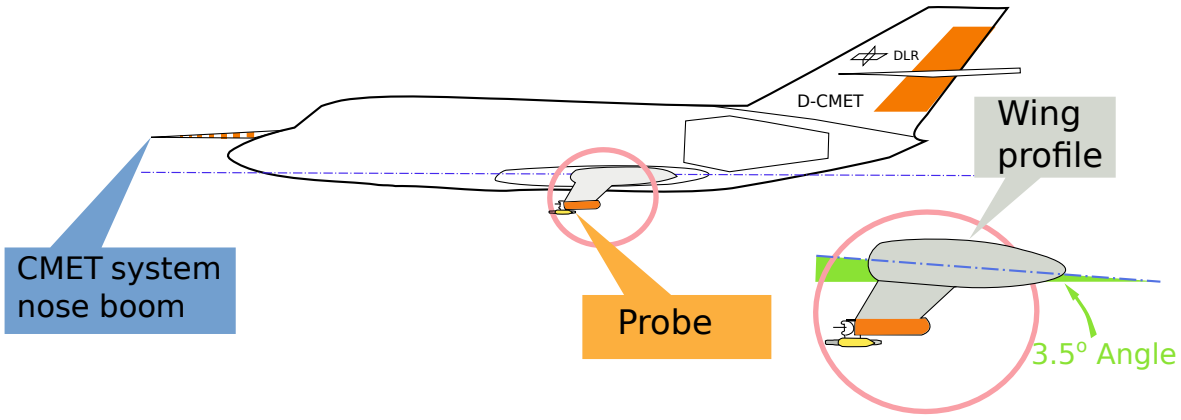

Figure 1. The DLR research aircraft Falcon equipped with the meteorological sensors in the nose boom (also referred to the "CMET system" in this study) and a probe mounted under the wing for the detection of coarse mode aerosols and cloud droplets/ice crystals.

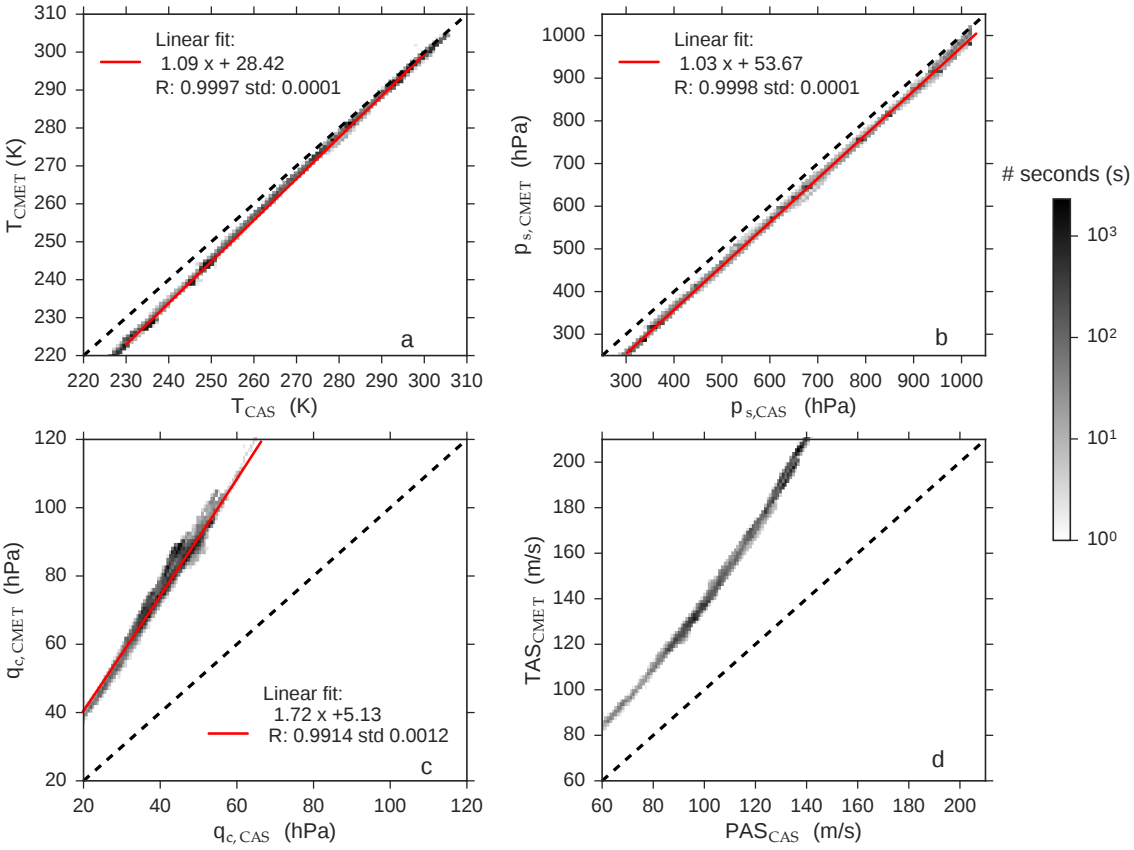

Figure 2. Statistical comparison between values recorded by the CMET ~~systyem~~ system and the CAS pitot tube during SALTRACE: temperature (a), static pressure (b), dynamic pressure (c) and ~~airspeed~~ air speed (d). ~~Histogram~~ The histogram color-map refers to the number of seconds of data at 1 Hz. Dashed lines represent the 1:1 line and the red lines linear fits.

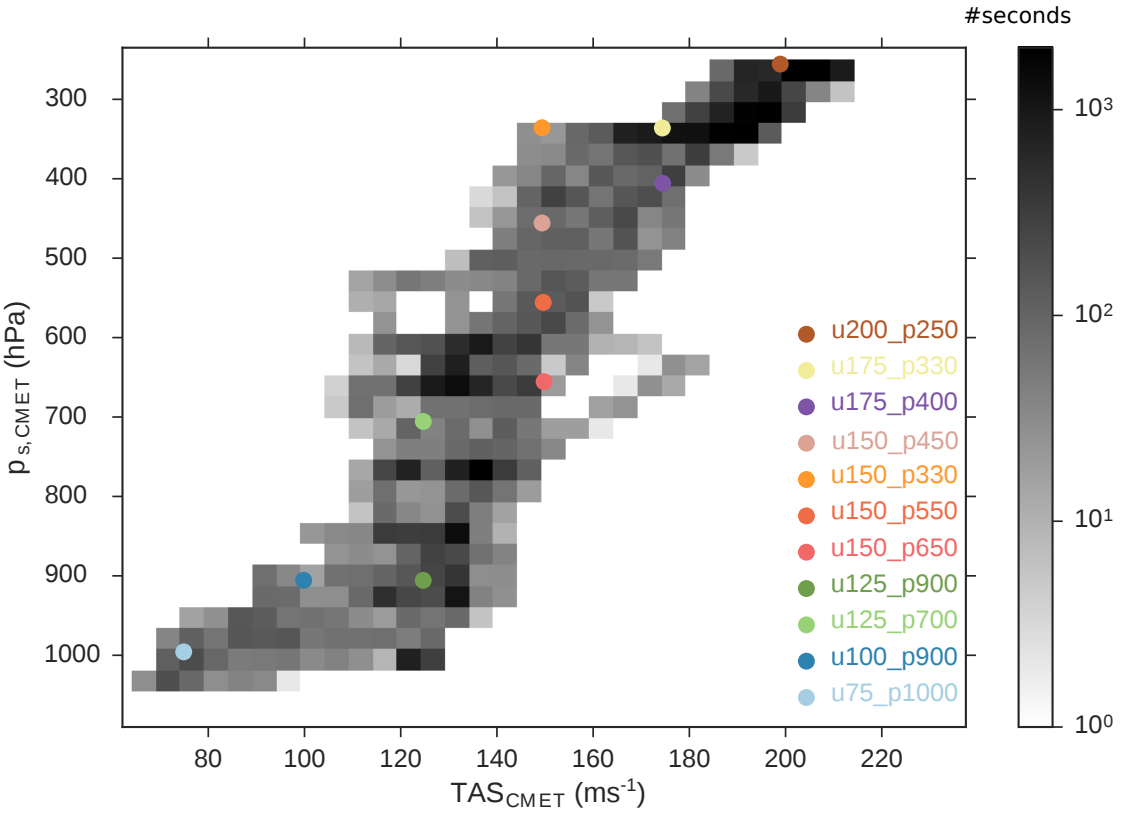

Figure 3. 2D histogram of flight conditions (pressure and TAS) recorded at 1 Hz by the CMET system at the nose boom during SALTRACE. Pixels are color coded with the number of seconds spent in the corresponding condition. Colored dots represent the selected test cases for the CFD investigations described in Tab. 2.

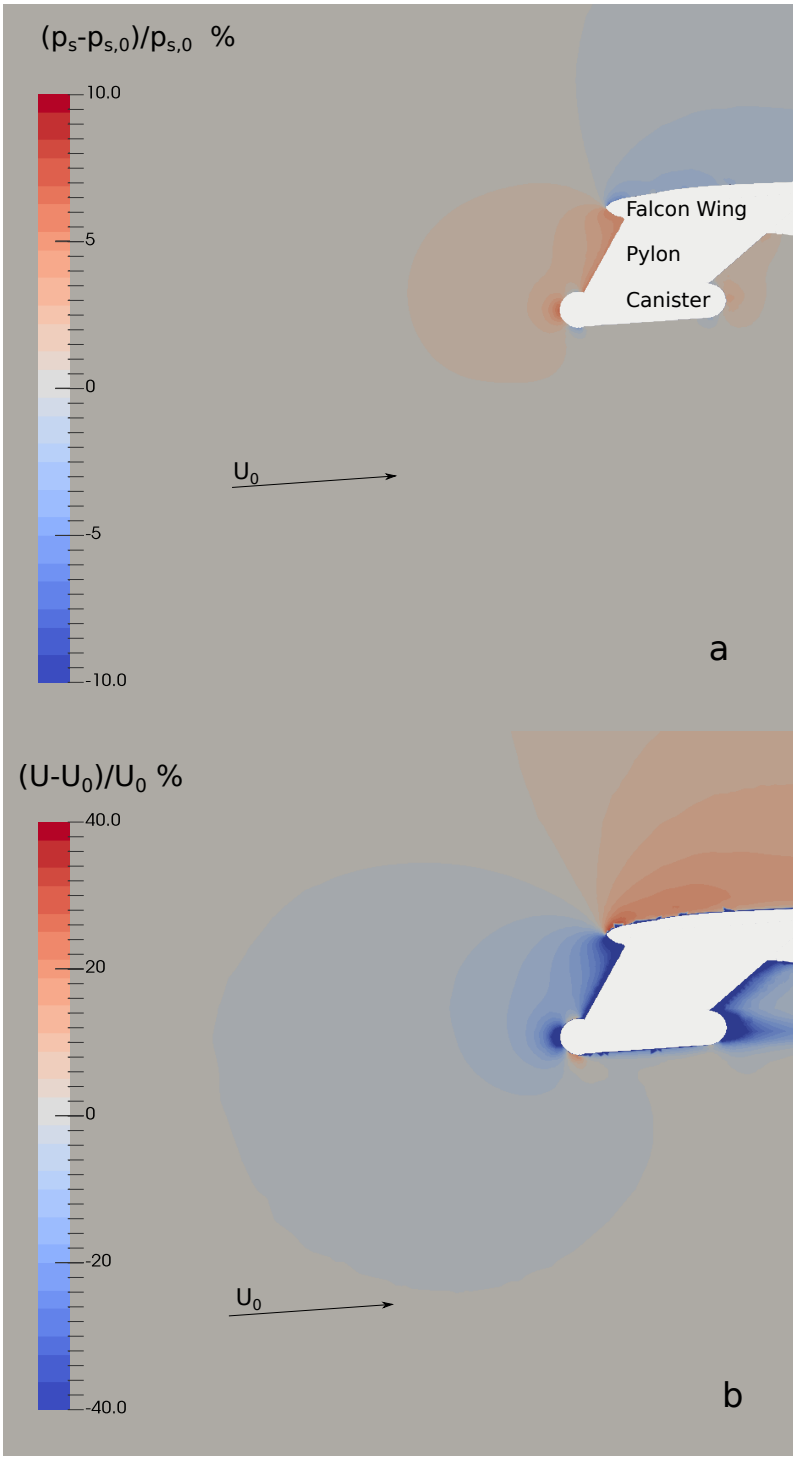

Figure 4. Vertical slice through the probe center and along the flow direction for the simulated test case u100_p900. The gray area represents the aircraft wing with the pylon and the probe installed. Colored contours illustrate the static pressure p_s (a) and the velocity field (b) expressed as the ratio ~~of~~ compared to the free stream values. The overpressure in front of the probe is slowing down the flow field.

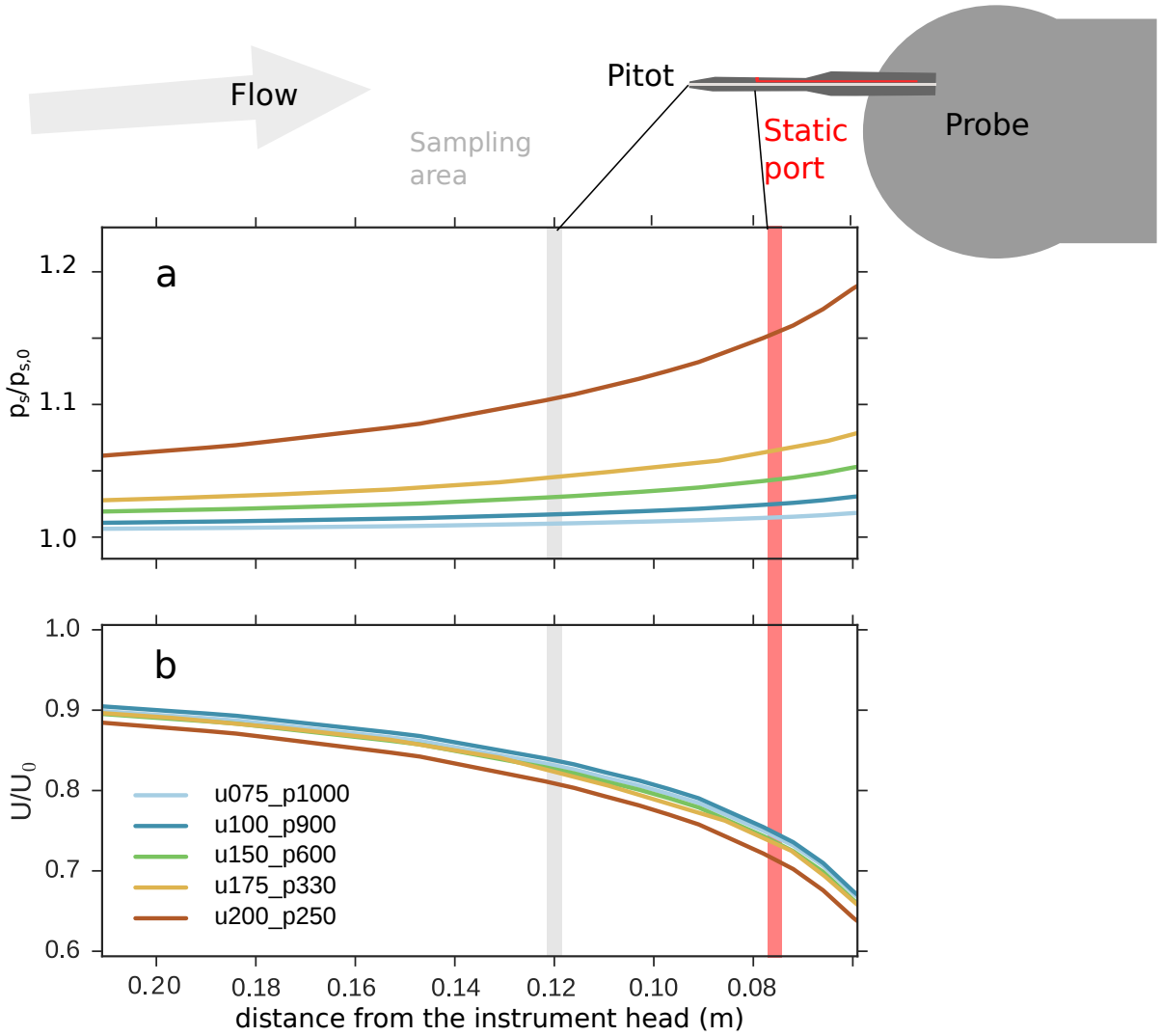

Figure 5. Static pressure and velocity normalized by the free stream values calculated along a streamline as a function of the distance from the instrument head. Different colors represent different tests described in Tab. 2. The gray area marks the pitot tube location, while the red area marks the static port location. The pitot tube was designed to measure the pressure conditions representative for the sampling area of the instrument.

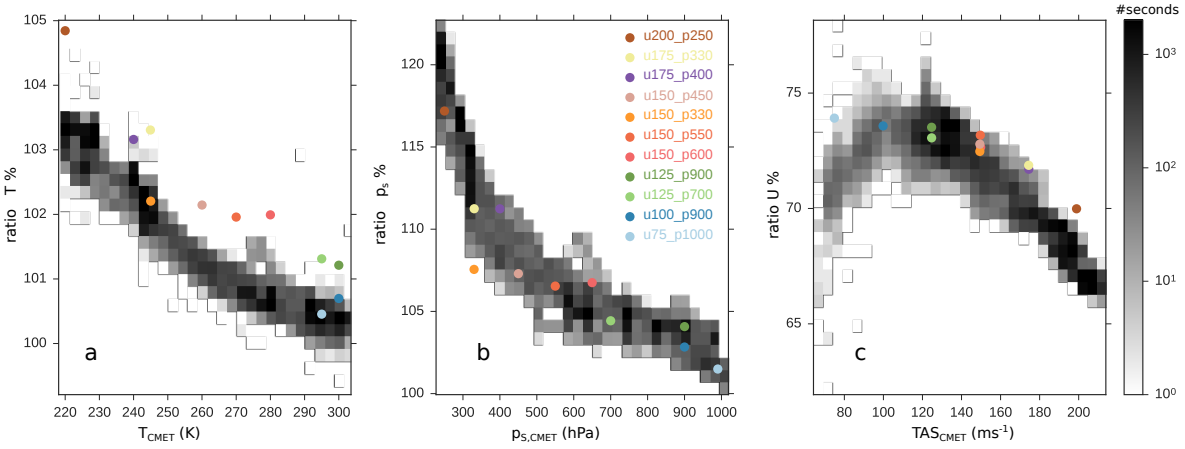

Figure 6. Statistical analysis of ~~differences~~ ratios between values read by the CMET system and the CAS pitot tube during SALTRACE. Histogram color-map refers to the number of seconds of data at 1 Hz. Colored dots represent the selected test cases for the CFD simulations described in Tab. 2.

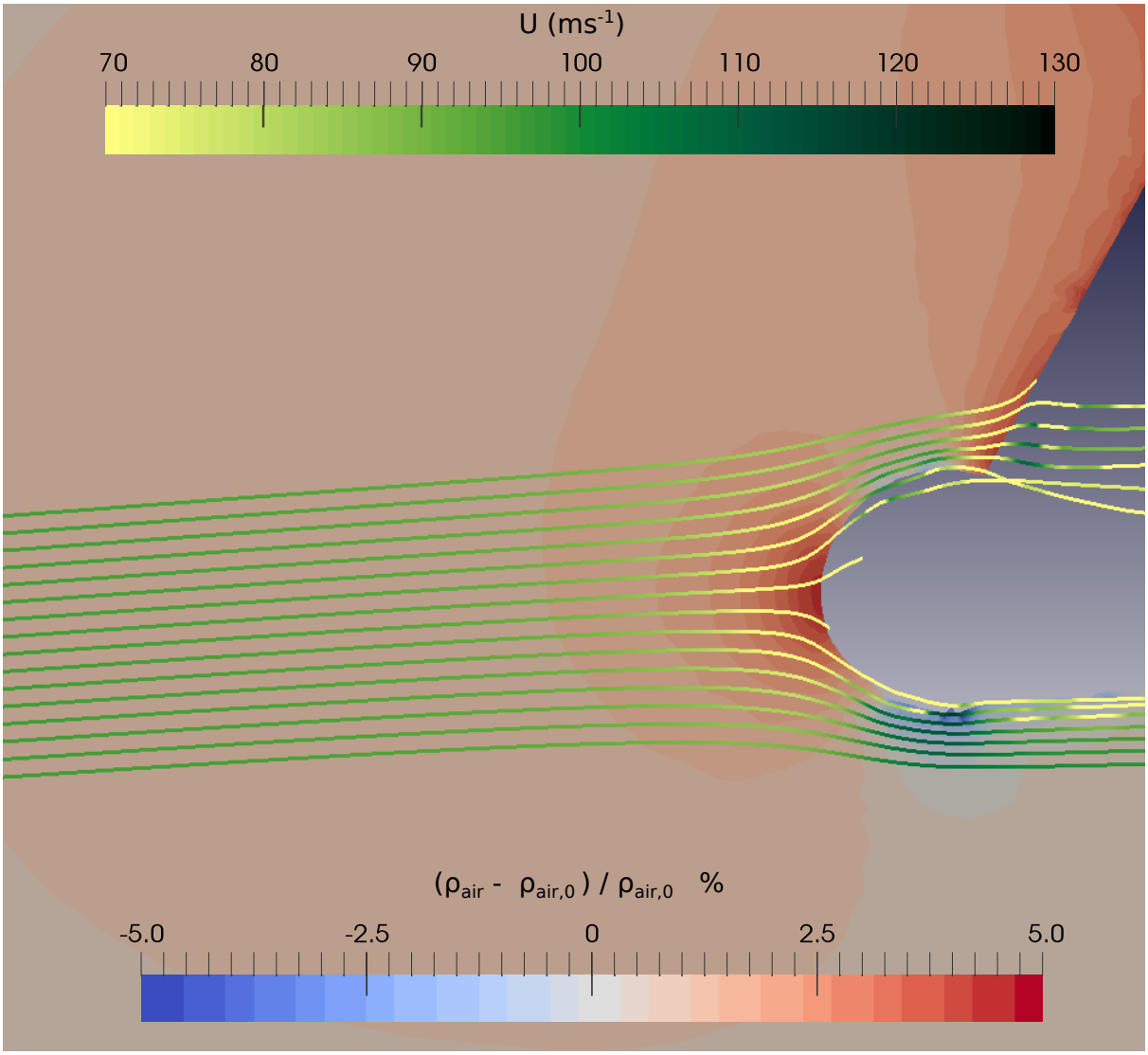

Figure 7. ~~Pressure profile~~ Relative deviation of air density ρ_{air} around the probe from the air density $\rho_{air,0}$ in the free stream for the test case u100_p900 as contours in the background (color code at the bottom). Lines in the foreground represent streamlines colored with the local air flow velocity ~~. The wing influences the streamlines that appear bent around~~ U (color code at the ~~probe~~top).

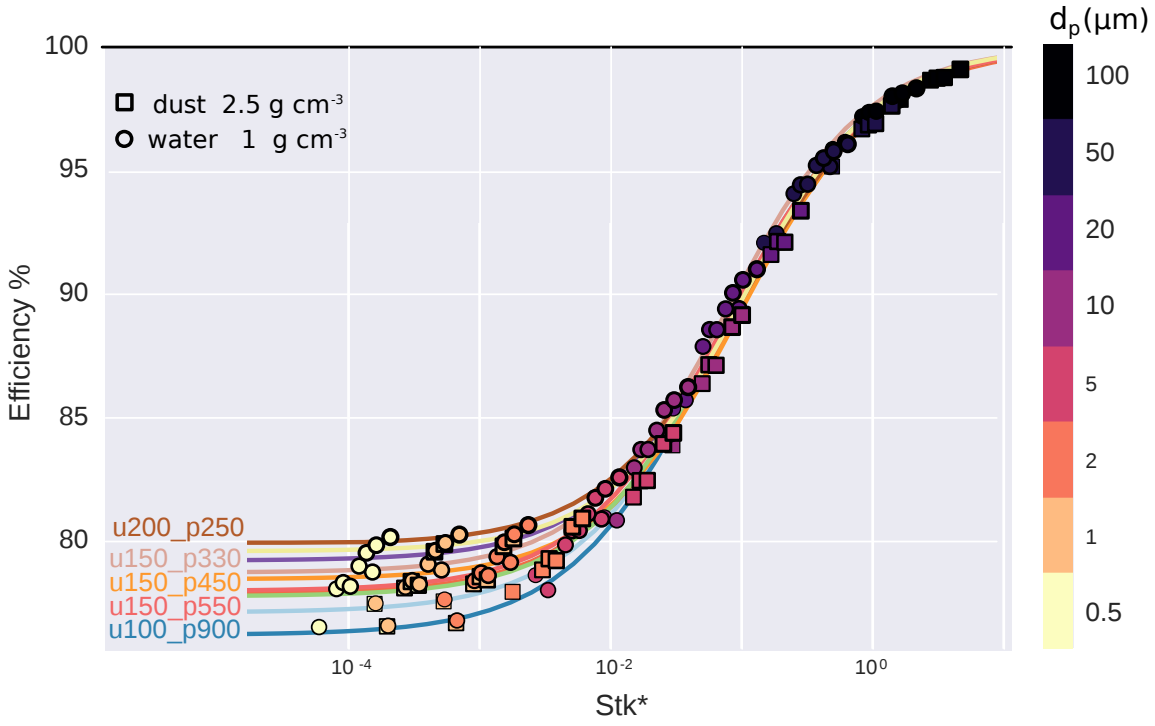

Figure 8. Sampling efficiency calculated as a function of modified Stokes number (see Eq. 4) for selected numerical test cases of Tab. 2. Each marker represents a run where we released $2 \cdot 10^5$ particles of a specific diameter (colors) and density (markers) in front of the probe in the computed flow field. Sampling efficiency is defined as the ratio between particles released and particles passing through the sampling area, renormalized by the corresponding areas. The black line marks 100 % efficiency. Curves are obtained by fitting the data with a sigmoid function (see text).

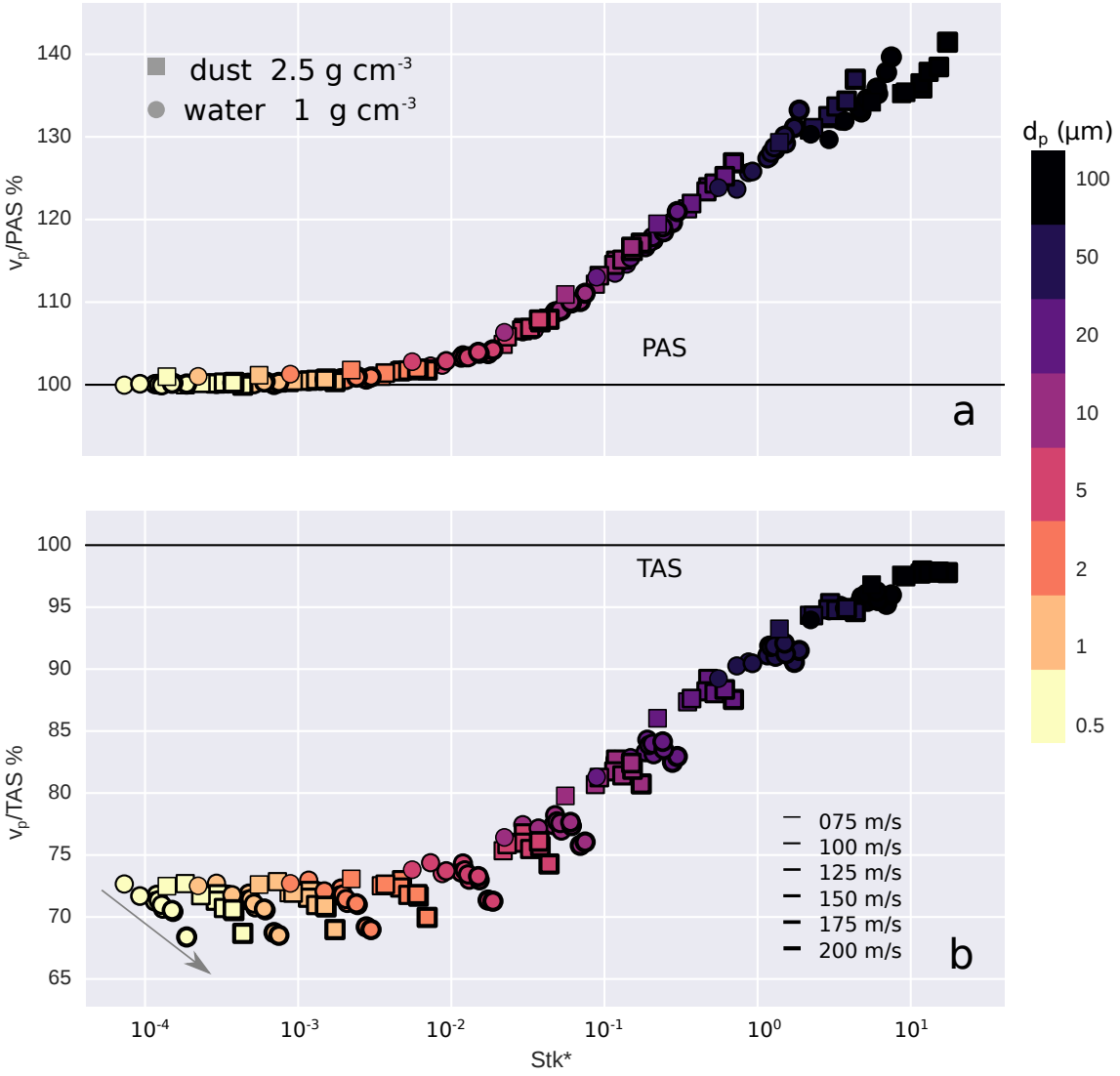

Figure 9. Particle velocity v_p normalized by PAS$_{CAS}$ (a) and TAS$_{CMET}$ (b) as a function of modified Stokes number Stk^*. Marker thickness increases with TAS. Colors denote particle diameters.

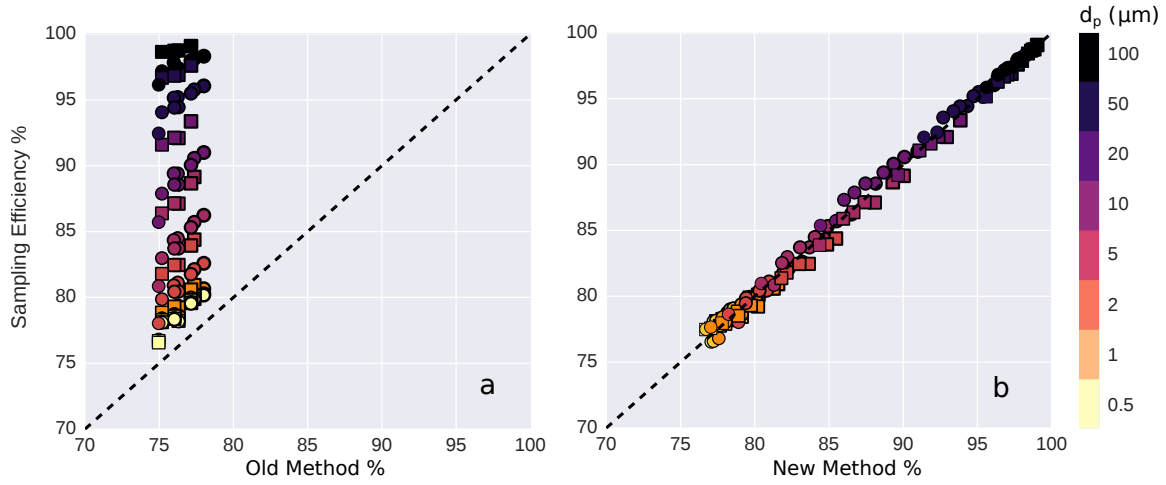

Figure 10. Simulated sampling efficiency f_{eff} versus sampling efficiencies estimated from the simulations using the "'Old Method"' (a) and the "'New Method"' (b). Different markers indicate different numerical test cases while the colors refer to the particle diameter. For the 'Old Method', the concentration is calculated using the probe conditions and using an adiabatic expansion to free stream conditions. For the 'New Method', the concentration is calculated using free stream conditions and corrected for the flow distortion by applying Eq. 6. To obtain the sampling efficiency, both concentrations are divided by concentration assumed ~~at~~ in the free stream.

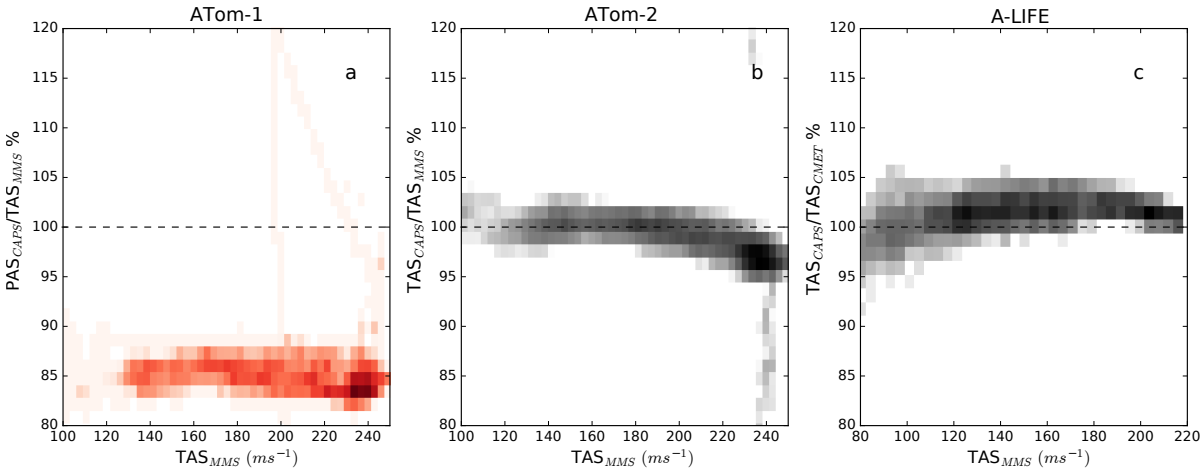

Figure 11. Air velocity recorded by CAPS normalized by air velocity recorded by the default aircraft systems. Data from ATom-1 (a), ATom-2 (b) and A-LIFE (c) is shown. While the CAPS pitot tube was calibrated to match PAS during ATom-1, it was calibrated to match the TAS during ATom-2 and A-LIFE. The pixels are color coded with the number of seconds of data at 1 Hz.

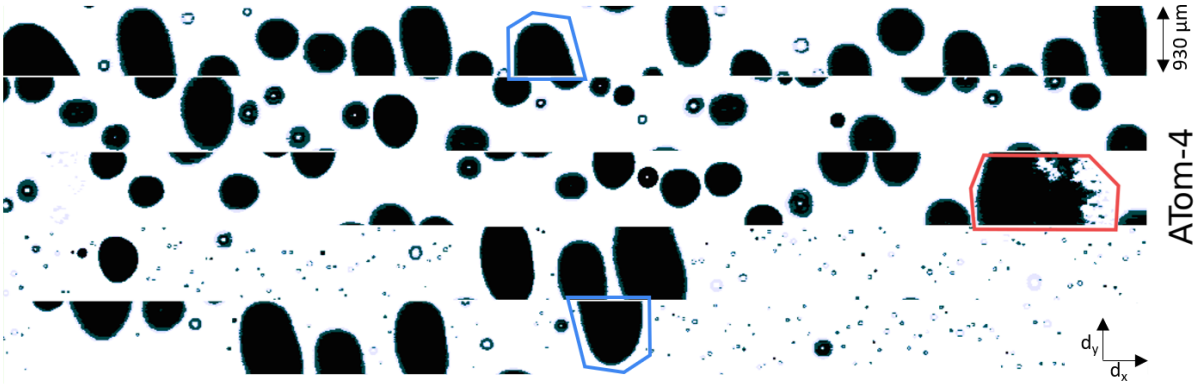

Figure 12. CIP gray-scale images collected in a cloud during the ~~A-LIFE~~ ATom-4 campaign. Colors are the three levels of shadow recorded on each photo-detector. The vertical scale is 62 pixels of 15 µm while the horizontal axis represents the time line. ~~Flight conditions are TAS=124 , p_s=840 , and T=298 . Red contours indicate~~ The red contour indicates splashes due to a droplet breakup. Blue contours highlight examples of large particles that are not ~~complitely~~ fully recorded.

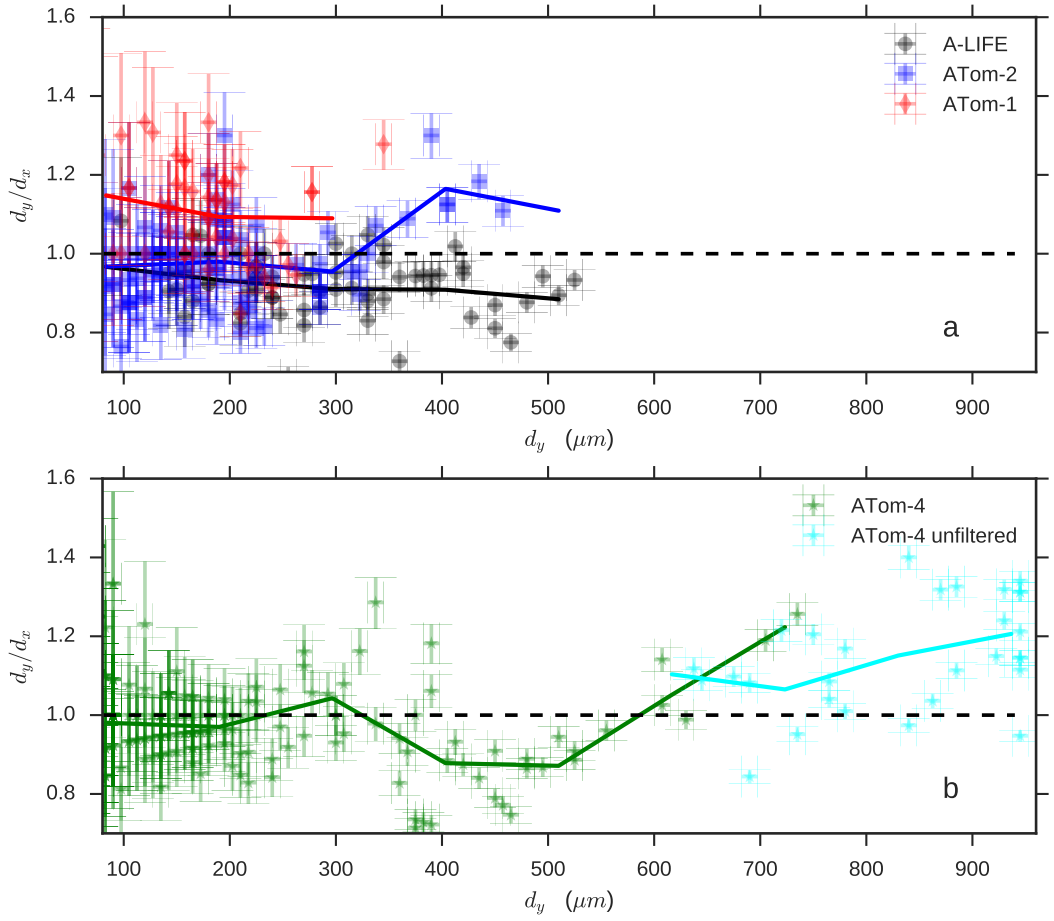

Figure 13. Ratio between the main axis lengths (d_y/d_x) of droplets recorded by the CIP during different campaigns (indicated by color). Error bars represent the CIP pixel resolution (15 µm). Considered are only particles recorded during cloud passages where the temperature ensures a liquid droplet state. ~~Black markers represent 200 particles selected from Fig. 12.~~ Red markers in the upper panel show data from the ATom-1 mission where the CAPS pitot tube, and thus the OAP reference velocity, was calibrated to match PAS whereas the data of the other campaigns (shown in ~~gray and~~ dark blue, black, green, light blue) was collected when the CAPS pitot tube was calibrated to match TAS (see also Fig. 11). Lines indicate the mean values of each campaign within several wider size intervals. Data from ATom-4 (green), including particles not fully covered by CIP (light blue), are shown in the lower panel.

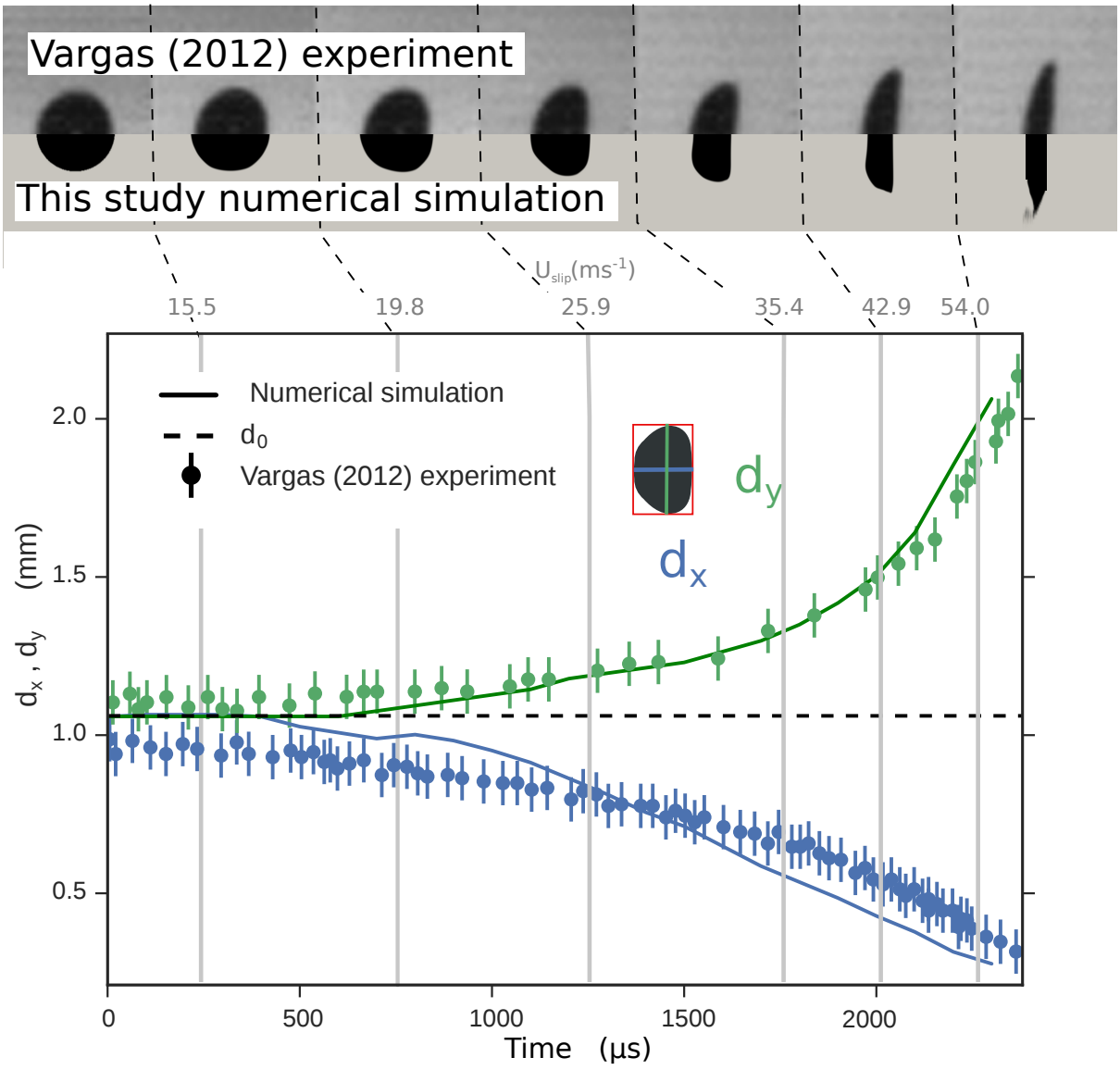

Figure 14. Simulations for a test case with a 1032 μm diameter droplet reproducing an experiment by Vargas (2012). In the upper panel the upper halves display images recorded by Vargas (2012) while the lower halves show corresponding simulated droplets. The air flow comes from the left. Time and relative ~~airspeed~~ air speed increase from the left to the right. The lower panel shows changes of both droplet axes lengths (d_x and d_y, see inlay image) as a function of time and relative velocity (labeled at the top) for the experiment from Vargas (2012) (dots) and for the simulations (continuous line).

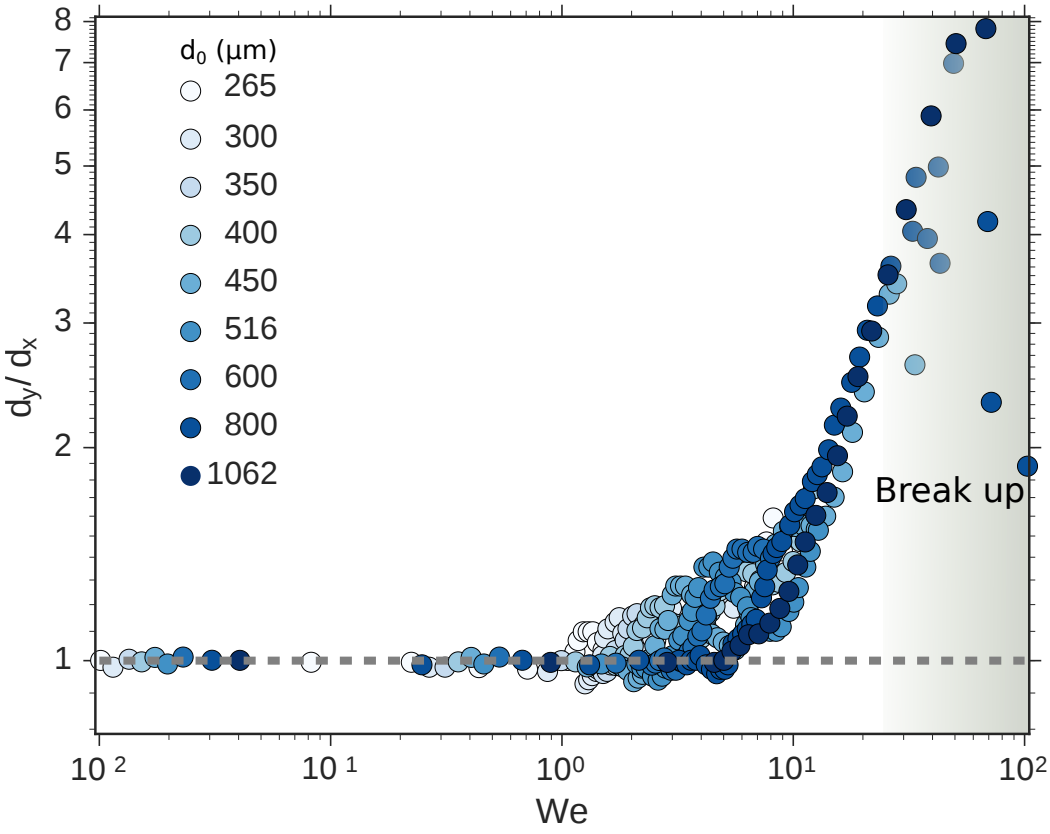

Figure 15. Droplet axis ratio (d_y/d_x) as a function of Weber number (~~We~~We). Different dots represent different simulations where we increased the initial droplet diameter d_0 from 265 µm (white) to 1062 µm (dark blue). The gray area represents the region where droplet ~~break up~~ breakup can occur.

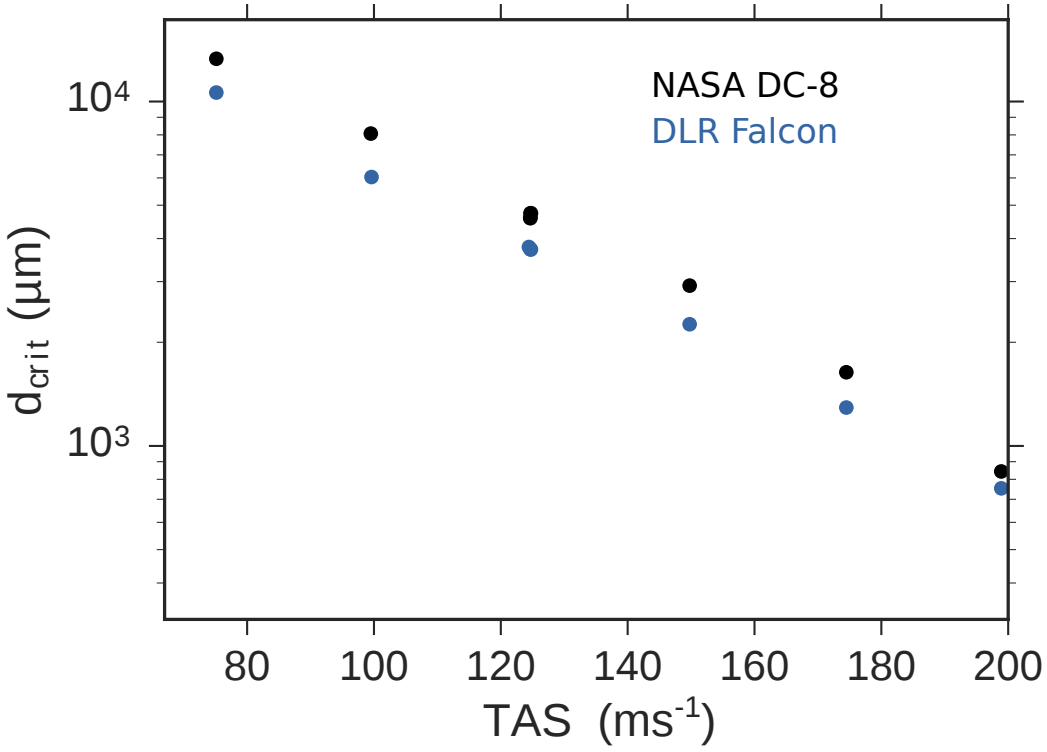

Figure 16. Critical diameter for droplet breakup as a function of TAS for the DLR Falcon and the NASA DC-8 configuration.

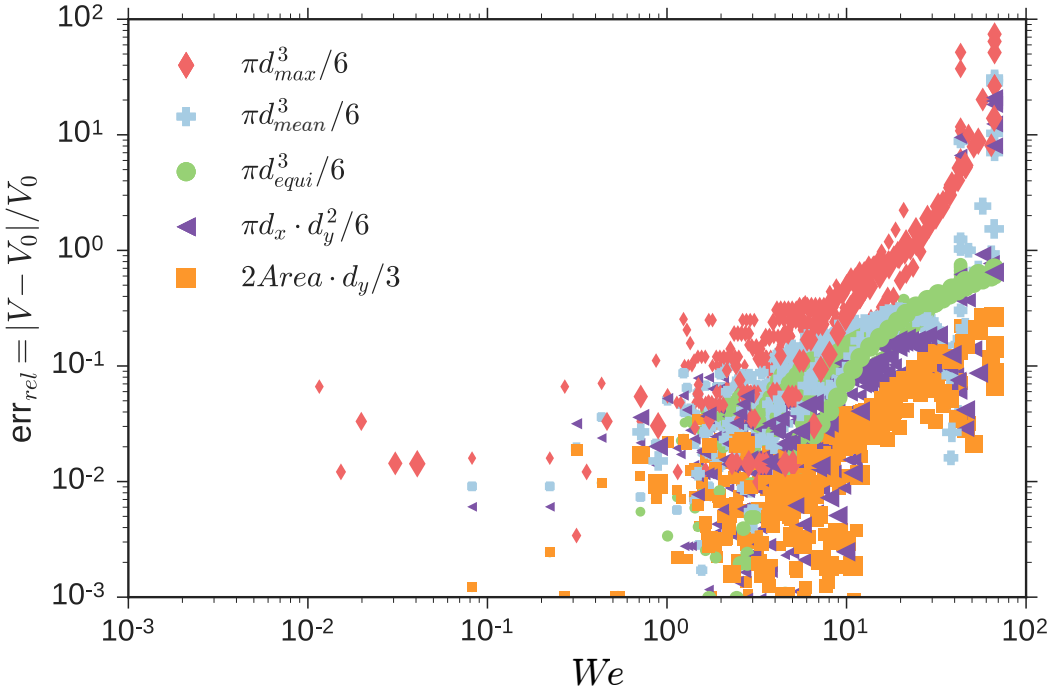

Figure 17. Relative error of the droplet volume as a function of Weber number (~~We~~We) for different volume approximations (colors). V_0 is the original droplet volume. Different marker sizes represent different simulations where we varied the droplet diameter.

Table 1. ~~Airplane~~ Aircraft configuration details and instruments used in this study. The DLR CAS (UNIVIE CAPS) is equipped with a 17 cm (24 cm) long pitot tube.

Campaign	~~Airplane~~ Aircraft	Max. altitude	Typ. cruise speed	Default flow sensors	Wing instrument	Reference
SALTRACE	DLR Falcon	12800 m	80-220 ms^{-1}	CMET system	DLR CAS	Weinzierl et al. (2017)
A-LIFE	DLR Falcon	12800 m	80-220 ms^{-1}	CMET system	UNIVIE CAPS	Weinzierl and ALIFE_Team (201
ATom	NASA DC-8	13800 m	90-250 ms^{-1}	MMS	UNIVIE CAPS	Wofsy et al. (2018)

Table 2. Flight conditions (p, T, TAS) used to initialize the numerical flow simulation test cases.

Test name	TAS (ms^{-1})	p (hPa)	T (K)
u75_p1000	75	1000	300
u100_p900	100	900	300
u125_p700	125	700	295
u125_p900	125	900	300
u150_p650	150	650	280
u150_p550	150	550	270
u150_p450	150	450	260
u150_p330	150	330	245
u175_p400	175	400	240
u175_p330	175	330	245
u200_p250	200	250	220

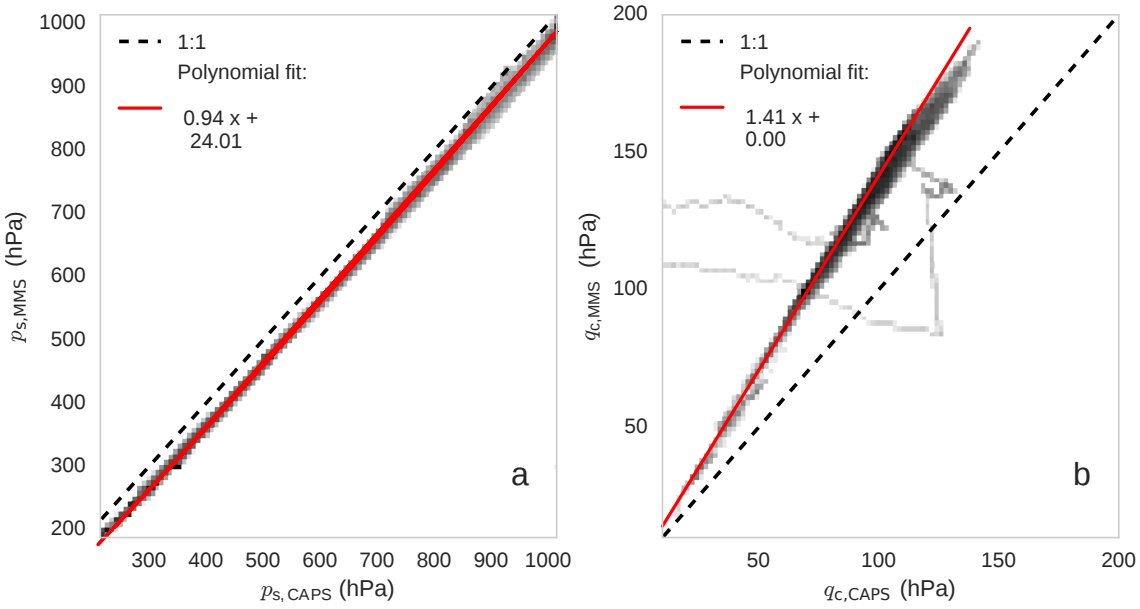

Figure A1. Statistical comparison between values recorded by the MMS and the CAPS pitot tube installed under the aircraft wing during ATom-1: static pressure (a) and dynamic pressure (b). The histogram color-map refers to number of seconds of data at 1 Hz. Dashed lines represent the 1:1 line and red lines ~~polynomial~~ linear fits.

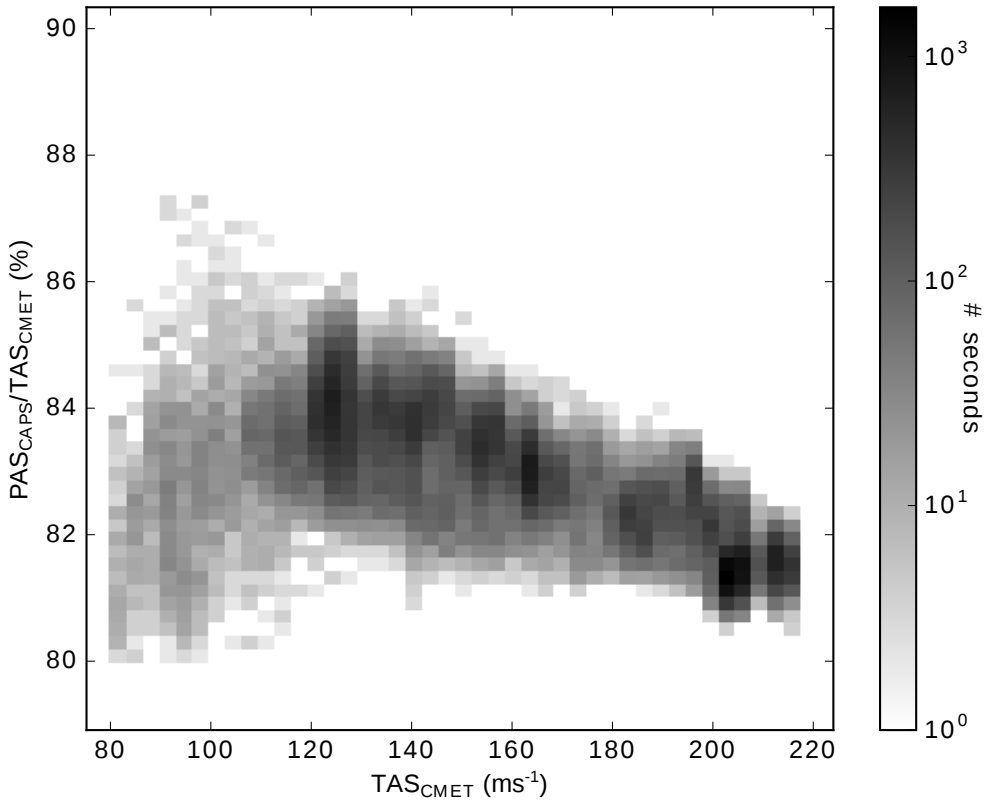

Figure A2. Statistical analysis of differences between ~~airspeed at~~ air speed in the free stream and at the probe during A-LIFE when CAPS was calibrated to match free stream conditions. TAS_{CMET} values were obtained by the CMET system and the PAS_{CAPS} was post-calculated using Eq. 1 and the dynamic and static pressure as well the temperature value at the probe obtained inverting the relation described in section 3.1.4. The histogram color-map refers to the number of seconds of data at 1 Hz.

Table A1. Different speeds used.

TAS	True air speed; Speed of airmass flown through (relative to aircraft)
TAS_{CMET}	True air speed obtained from CMET system
TAS_{MMS}	True air speed obtained from MMS system
TAS_{CAPS}	True air speed obtained from CAPS instrument after re-calibration to match TAS
PAS	Probe air speed; Speed of air at the probe (relative to aircraft, i.e. also relative to probe)
PAS_{CAS}	Probe air speed obtained from CAS instrument
PAS_{CAPS}	Probe air speed obtained from CAPS instrument
U	(Local) air speed; Speed of air at a given location (relative to aircraft)
U_0	Free stream velocity; Equivalent to TAS
v_p	Particle speed; Speed of a particle (relative to aircraft)
U_{slip}	Slip velocity; Speed of a particle relative to the suspending air around the particle
U_{sound}	Speed of sound
M	Mach Number; Equal to U/U_{sound}

Table A2. Acronyms and symbols used.

CFD	Computational Fluid Dynamic
LWC	Liquid Water Content
OAP	Optical Array Probe
OPC	Optical Particle Counter
~~PAS Probe Air Speed TAS True Air Speed~~ VOF	Volume Of Fluid
~~d~~ d_p	Particle diameter
~~v_p~~ ϱ_p	Particle ~~speed~~density
V	Droplet Volume
~~U Flow speed ρ Density~~ σ	Surface tension
γ	Heat capacity ratio
p_s	Static pressure
p_{tot}	Total pressure
q_c	Dynamic pressure
~~M Mach Number Stk~~ Stk^*	Modified Stokes number (Eq. 4)
~~We~~ We	Weber Number

Author contributions. BW and AS designed the study. AS carried out the simulations and the numerical analysis. BW and MD performed the airborne CAPS measurements. MD preprocessed the CAPS data. TPB provided the MMS data. AS analyzed the data with the help of BW and wrote the manuscript with the support of BW and JG. JG, BW, and AS revised the manuscript. All authors commented on the manuscript.

Table A3. Sampling efficiency ~~values~~ f_{eff} (%) for different test cases ~~as a function of~~ for different particle ~~diameter~~ diameters d_p and ~~density~~ densities ρ_p as shown in Fig. 8.

~~diam~~ d_p (µm)	0.5	1	2	5	10	20	50	100
test case								
	$\rho_p = 1$ gcm^{-3} (water)							
u75_~~p990~~ p1000	76.89	76.93	77.09	78.09	80.50	84.99	91.86	95.75
u100_p900	76.60	76.68	76.82	78.06	80.89	85.85	92.35	96.12
u125_p900	77.77	77.81	78.11	79.46	82.55	87.42	93.50	96.25
u150_p650	78.27	78.42	78.76	80.43	83.70	88.50	94.42	97.08
u150_p550	78.18	78.29	78.64	80.32	83.76	88.52	94.44	96.71
u175_p400	79.42	79.52	79.87	81.66	85.20	90.03	95.57	98.62
u175_p330	79.75	79.80	80.14	82.14	85.81	90.66	95.64	98.70
u200_p250	80.16	80.30	80.66	82.60	86.22	91.12	96.18	97.04
	$\rho_p = 2.5$ gcm^{-3} (mineral dust)							
u75_~~p990~~ p1000	76.91	77.01	77.40	79.49	83.48	88.93	95.01	97.77
u100_p900	76.62	76.71	78.11	80.48	84.88	90.13	95.77	97.71
u125_p900	77.76	77.93	78.64	81.39	85.89	91.06	96.61	98.70
u150_p650	78.34	78.61	79.28	82.51	87.13	92.25	96.23	99.25
u150_p550	78.24	78.47	79.12	82.51	87.18	92.10	97.49	98.99
u175_p400	79.47	79.74	80.58	84.02	88.62	93.61	98.07	98.94
u175_p330	79.77	80.06	80.88	84.32	89.18	94.40	98.50	99.20
u200_p250	80.26	80.79	81.66	85.20	89.85	94.22	97.97	99.26

Competing interests. The authors declare that they have no competing interests.

Data availability. The data are archived in the World Data Center ORNL DAAC and can be accessed under DOI 10.3334/ornldaac/?? (Spanu et al., 2018)

Acknowledgements. This work was supported by the VERTIGO Marie Curie Initial Training Network, funded through the European Seventh Framework Programme (FP7 2007-2013) under Grant Agreement number 607905, and by the European Research Council under the European Community's Horizon 2020 research and innovation framework program/ERC grant agreement number 640458 (A-LIFE). The SALTRACE aircraft field experiment was funded by the Helmholtz Association (Helmholtz-Hochschul-Nachwuchsgruppe AerCARE, Grant Agreement VH-NG-606) and by DLR. We also would like to acknowledge partial funding through LMU Munich's Institutional Strategy LMUexcellent within the framework of the German Excellence Initiative. The A-LIFE field experiment was funded under ERC grant agree-

ment number 640458 (A-LIFE). In addition, DLR and two EUFAR projects provided funding for a significant amount of additional flight hours and aircraft allocation days for the A-LIFE aircraft field experiment. The ATom mission and the MMS measurements were funded under National Aeronautics and Space Administration's Earth Venture program (grant NNX15AJ23G). CAPS measurements during ATom were additionally supported by the University of Vienna. We are thankful to Andreas Giez, Volker Dreiling, Christian Mallaun, and Martin Zoeger for providing the meteorological data for SALTRACE and A-LIFE. We would like to thank DMT for the fruitful discussions related to the CAPS instrument. Thanks to the SALTRACE, A-LIFE, and ATom science teams, the pilots, administrative and technical support teams for their great support before and during the field missions and for the accomplishment of the unique research flights.